Models for flows with melting heat and convection

By

Khursheed Muhammad

Department of Mathematics
Quaid-i-Azam University
Islamabad, Pakistan
2021

Models for flows with melting heat and convection

By

Khursheed Muhammad

Supervised By

Prof. Dr. Tasawar Hayat

Department of Mathematics
Quaid-i-Azam University
Islamabad, Pakistan
2021

Models for flows with melting heat and convection

By

Khursheed Muhammad

A THESIS SUBMITTED IN THE PARTIAL FULFILLMENT OF THE REQUIREMENT FOR THE DEGREE OF

DOCTOR OF PHILOSOPHY

IN

MATHEMATICS

Supervised By

Prof. Dr. Tasawar Hayat

Department of Mathematics
Quaid-i-Azam University
Islamabad, Pakistan

2021

Author's Declaration

I **Khursheed Muhammad** hereby state that my PhD thesis titled **Models for flows with melting heat and convection** is my own work and has not been submitted previously by me for taking any degree from the Quaid-I-Azam University Islamabad, Pakistan or anywhere else in the country/world.

At any time if my statement is found to be incorrect even after my graduate the university has the right to withdraw my PhD degree.

Name of Student: **Khursheed Muhammad**

Date: **12-08-2021**

Plagiarism Undertaking

I solemnly declare that research work presented in the thesis titled **Models for flows with melting heat and convection** is solely my research work with no significant contribution from any other person. Small contribution/help wherever taken has been duly acknowledged and that complete thesis has been written by me.

I understand the zero tolerance policy of the HEC and **Quaid-I-Azam University** towards plagiarism. Therefore, I as an Author of the above titled thesis declare that no portion of my thesis has been plagiarized and any material used as reference is properly referred/cited.

I undertake that if I am found guilty of any formal plagiarism in the above titled thesis even afterward of PhD degree, the University reserves the rights to withdraw/revoke my PhD degree and that HEC and the University has the right to publish my name on the HEC/University Website on which names of students are placed who submitted plagiarized thesis.

Student/Author Signature: ____________________

Name: **Khursheed Muhammad**

Models for flows with melting heat and convection

By

Khursheed Muhammad

CERTIFICATE

A THESIS SUBMITTED IN THE PARTIAL FULFILLMENT OF THE REQUIREMENTS FOR THE DEGREE OF THE

DOCTOR OF PHILOSOPHY IN MATHEMATICS

We accept this dissertation as conforming to the required standard

1. **Prof. Dr. Sohail Nadeem**
(Chairman)

2. **Prof. Dr. Tasawar Hayat**
(Supervisor)

3. **Dr. Rahmat Ellahi**
Associate Professor
Department of Mathematics & Statistic
International Islamic University,
Sector, H-10 Islamabad
(External Examiner)

4. **Dr. Maryiam Javed**
Associate Professor
Department of Applied Mathematics
and Statistics, Institute of Space
Technology (IST), Islamabad
(External Examiner)

Department of Mathematics
Quaid-I-Azam University
Islamabad, Pakistan
2021

Certificate of Approval

This is to certify that the research work presented in this thesis entitled **Models for flows with melting heat and convection** was conducted by Mr.**Khursheed Muhammad** under the kind supervision of **Prof. Dr. Tasawar Hayat**. No part of this thesis has been submitted anywhere else for any other degree. This thesis is submitted to the Department of Mathematics, Quaid-i-Azam University, Islamabad in partial fulfillment of the requirements for the degree of Doctor of Philosophy in field of Mathematics from Department of Mathematics, Quaid-i-Azam University Islamabad, Pakistan.

Student Name: **Khursheed Muhammad** Signature: Isheed

External committee:

a) **External Examiner 1**: Signature:
Name: **Dr. Rahmat Ellahi**
Designation: Associate Professor
Office Address: Department of Mathematics & Statistics, International Islamic University, Sector H-10 Islamabad.

b) **External Examiner 2**: Signature:
Name: **Dr. Maryiam Javed**
Designation: Associate Professor
Office Address: Department of Applied Mathematics and Statistics, Institute of Space Technology (IST), Islamabad.

c) **Internal Examiner** Signature:
Name: **Dr. Tasawar Hayat**
Designation: Professor
Office Address: Department of Mathematics, QAU Islamabad.

Supervisor Name: Signature:
Prof. Dr. Tasawar Hayat

Name of Dean/HOD: Signature: Nadeem
Prof. Dr. Sohail Nadeem

Dedicated to

my loving parents (Baba Jaan and Moor Jaana)

and supervisor

Acknowledgement

In the name of Allah the most beneficient the most merciful. I praise and thank **Allah Almighty**, who grant me with courage, guidance and opportunity to complete this dissertation. I offer my humblest gratitude to the most respectable personality, **Prophet Muhammad (P. B. U. H).**

I would like to express my deep and sincere gratitude to my supervisor, **Prof. Dr. Tasawar Hayat** for his great support, excellent guidance, patience and care throughout my thesis. His extraordinary knowledge and incredible skills have provide a good basis for the present thesis.

I am grateful to Chairman of Mathematics Department, **Prof. Dr. Tasawar Hayat** and all faculty members for providing me facilities and proper atmosphere to complete the research work.

My deepest and heartiest thanks to my seniors and friends (labfellows) specially **Dr Fahad Mlunir Abbassi, Dr Bilal Ashraf, Dr Muhammad Farooq, Dr Taseer Muahammad, Dr Muhammad Waqas, Dr Shahid Farooq, Dr Zakir Ahmad, Dr Khalilurehman, Dr Muhammad Ijaz Khan, Dr Waleed Ahmed Khan, Dr Mubashir Umar, Dr Yasir Satti, Dr Asif, Dr Imad Khan, Dr Faisal Shah and Mr Zahid Ahmed, Mr Sohail Ahmed Khan, Mr Waqar Ahmed**

Khan, Mr Habibullah, Mr Inayatullah, Dr Sadaf Nawaz, Dr Sumaira Jabeen, Dr Sumaira Qayyum, Ms Farwah Haider, Ms Saima Rani, Ms Aqeela Qaiser for their great help and constant presence that they have given me during my research work. I am really thankful to my friends **Dr Bilal Ahmad, Dr Arsalan Aziz** and **Dr Sajjad Hussain** and some other special friends for their valuable discussions that helped me to understand my research in a better way.

Furthermore I can not put aside the financial support of **HEC (Higher Education Commission of Pakistan)** during my PhD study. I am really thankful to HEC for such supporst under **HEC Indegeneous Scholarship, Phase-II Batch V** and providing me the title of **HEC Scholar** and finally Doctor.

At the end I would like to thanks to my family, my father whose presence is always a source of strength and inspiration for me, my mother whose prayers are source of my every achievement and my brothers, uncles, cousins (Dr Muhammad Israr, Muhammad Nisar, Muhammad Ishaq, Muhammad Imran, Muhammad Aizaz, Irshad Ali, Mumtaz Ali, Muhammad Ayaz, Jamsheed Khan, Sajjad Ali, Tahir, Muhammad Sareer, Ihtisham Ali) whose always support me for my academic career throughout the years.

Dr. Khursheed Muhammad

Preface

Due to extensive applications in engineering and industries, the thermal properties of fluids (materials) have gained a great interest in recent days. Conventional fluids such as water, engine oil, kerosine oil, ethylene oil, gasoline oil etc., possesses very small heat transport capabilities due to its lower thermal conductance. Thermal conductance of mentioned conventional fluids can be improved via suspension of nano-sized (1-100nm) particles, known as nanoparticles. Nanoparticles exist in various varieties such as metal, carbides, nanometals or nitrides (CNTs, graphite). In these nanoparticles, CNTs have promising capability of heat conduction. At room temperature, thermal conductance of carbon substances is five times of ordinary substances. Not only thermal conductance is the unique quality of CNTs but it also possesses exceptional electrical, mechanical properties and applications in atomic transportation and nano-sensors. CNTs are cylindrical shaped substances of carbon fenced by graphene sheet. On the basis of graphene sheet, CNTs are classified into MWCNTs (cylindrical carbon substance fenced by more than one graphene sheet) and SWCNTs (cylindrical carbon substance fenced by one graphene sheet). CNTs are utilized in medicine, batteries, electronic instruments, tissue engineering, solar storages, biosensors, purification process etc.

Having such in mind, the presented thesis consists of ten chapters. In chapter one, we have reviewed literature regarding nanomaterials, stretching surface, squeezed flow, melting heat and stagnation flow. Mathematical modeling for concerned equations (continuity, momentum, energy and concentration) in case of viscous and Jeffrey fluids is presented. Xue expressions for CNTs while Hamilton-Crosser expressions for hybrid nanofluid and ordinary nanofluids are established. Moreover fundamental concepts of OHAM and Bvp4c methods for series and numerical solutions are incorporated.

Chapter two concentrates on melting effect in three dimensional flow of CNTs (SWCNTs, MWCNTs) over a stretching sheet. Chemical reactions and porous medium are also considered. Nanomaterial is constructed through dispersion of CNTs in water-basefluid. Shooting method (bvp4c) is implemented for solutions development. Moreover comparison between MWCNTs and SWCNTs is also given. Contents of this chapter are published in **Results in Physics 8 (2018) 415-421.**

Chapter three addresses; melting heat and thermal radiation effects in stagnation flow of CNTs (carbon nanotubes). Flow is generated via stretching sheet. Chemical reactions are accounted. Gasoline oil and water are taken as baseliquids. Further conversion of involved PDEs (mass, momentum, energy and concentration) into ODEs is performed through suitable transformations. The obtained ODEs are solved through OHAM. Velocity, temperature, skin friction coefficient, concentration and Nusselt number under involved variables are analyzed graphically. Material of this chapter is published in **Communications in Theoretical Physics 69 (2018) 441-448.**

Chapter four addresses entropy production in squeezing flow of CNTs (carbon nanotubes). Nanomaterial is constructed by adding CNTs in water basefluid. Heat transport in presence of melting heat is explored. Adequate transformations are implemented for conversion of PDEs into ODEs. Shooting technique (bvp4c) is used for the numerical solutions. Contents of this chapter are published in **Journal of Thermal Analysis and Calorimetery 140 (2020) 321–329.**

Unsteady squeezed flow of Jeffrey nanomaterial is discussed in chapter five. Brownian motion and thermophoresis describes nanofluid characteristics. Convection conditions for heat and mass transfer are taken into account. The differential systems are computed for the convergent solutions. The acceptable values for convergence analysis are recognized. Detail analysis is performed for velocity, concentration, temperature, skin friction and Nusselt and Sherwood numbers. Material of of this chapter is published in **Physica Scripta 94 (2019) 105703.**

Chapter six explores melting phenomenon in MHD flow of Jeffrey nanomaterial by a stretched sheet. Heat transfer characteristics are elaborated through Joule heating and viscous dissipation. Thermophoresis and Brownian motion characteristics are analyzed via Boungiorno model for nanofluid. Chemical reaction with activation energy is studied. Flow is addressed in stagnation point region. Field equations (PDEs) are transmitted into ODEs by employing adequate transformations. These non-linear systems (ODEs) are solved by OHAM. Research of this chapter is also published in **Physica Scripta 94 (2019) 115702.**

Jeffrey nanofluid in existence of stagnation point by a permeable stretched cylinder is addressed in chapter seven. Viscous dissipation, Brownian motion, thermal radiation and thermophoresis impacts are considered. Surface is subject to convective heat and mass conditions. Activation energy is taken into account. By adequate transformations, the PDEs are converted into ODEs and then solved employing OHAM. This research is submitted for publication in **International Communications in Heat and Mass Transfer.**

In chapter eight we have arranged comparative study of hybrid nanofluid (MWCNTs+Cu+Water), nanofuid (MWCNTs+Water) and basefuid (water). Flow is due to curved stretching sheet. Flow is explored through slip boundary condition. Heat transport analysis is performed in existence of viscous dissipation, mixed convection and convective boundary condition. Transformation technique is applied in obtaining ODEs. These coupled ODEs are solved via RK-4 algorithms (bvp4c). Material of this chapter is published in **Journal of Thermal Analysis and Calorimetery (2020) doi.org/10.1007/s10973-020-09577-z.**

Chapter nine examines stagnation point flow of hybrid nanofluid (SWCNTs+Ag+Gasoline oil) by a variable thicked stretched sheet. Viscous dissipation and melting effects are taken into consideration for heat transport characteristics. PDEs (expressions) are transmitted into ODEs via transformation technique. Governing ODEs are then converted into system of first order differential system in order to solve by bvp4c. Observations of this chapter are published in **International Communications in Heat and Mass Transfer.121 (2021) 104805.**

Chapter ten deals with hybrid nanomaterial (SWCNTs+CuO+Ethylene glycol) flow by a curved non-linear stretching sheet. Heat transfer features are emphasized via Newtonian heating. Viscous dissipation is also reported. Coupled non-linear ODEs are constructed from the field equations (PDEs) through adequate transformations. These non-linear ODEs are then reduced into system of first order. Impacts of flow parameters on temperature, skin friction, velocity and Nusselt number are presented graphically. Comparison amongst hybrid nanofluid (SWCNTs+CuO+Ethylene glycol), nanofluid (SWCNTs+Ethylene glycol) and basefluid (Ethyleneglycol) is arranged. Observations of this chapter are published in **Journal of Thermal Analysis and Calorimetery (2020) doi.org/10.1007/s10973-020-10196-x.**

Contents

Chapter 1

Literature, basic laws, boundary layer equations and solution methodologies

1.1 Nomenclature

Nomenclature for physical parameters involved in all chapters are listed below.

CNTs	carbon nanotubes
SWCNTs	single-walled CNTs
MWCNTs	multi-walled CNTs
Au	aluminum
Cu	copper
Ag	silver
CuO	copper oxide
HNF	hybrid nanofluid
Ns	dimensionless entropy generation
Be	Bejan number
V	velocity

$u_1,\ u_2,\ u_3$	velocity components (for Cartesian coordinates)
$x,\ y,\ z$	Cartesian coordinates
$u_r,\ u_{\overline{\theta}},\ u_z$	velocity components (for cylindrical coordinates)
$r,\ \overline{\theta},\ z$	cylindrical coordinates
$s,\ r$	curvilinear coordinates
$\boldsymbol{\tau}$	Cauchy stress tensor
$\mathbf{b}$	body forces
$\boldsymbol{\nabla}$	differential operator (Del.)
$\mathbf{I}$	identity tensor
$\mathbf{S}$	extra stress tensor
$\mathbf{A}_1$	first Rivilin Ericksen tensor
$\mathbf{B}$	magnetic field
$\mathbf{J}$	current density
p	pressure
τ_0	ratio of heat capacities
$\tau_{xx},\ \tau_{yy},\ \tau_{zz}$	normal stresses (for Cartesian coordinates)
$\tau_{xy},\ \tau_{xz},\ \tau_{yx},\ \tau_{zx},\ \tau_{yz},\ \tau_{zy}$	tangential stresses (for Cartesian coordinates)
$\tau_{rr},\ \tau_{\overline{\theta}\overline{\theta}},\ \tau_{zz}$	normal stresses (for cylindrical coordinates)
$\tau_{r\overline{\theta}},\ \tau_{rz},\ \tau_{\overline{\theta}r},\ \tau_{z\overline{\theta}},\ \tau_{\overline{\theta}z},\ \tau_{zr}$	tangential stresses (for cylindrical coordinates)
ρ_f	density for basefluid
ρ_{nf}	density for nanofluid
ρ_{hnf}	density for HNF
ρ_{CNTs}	density for CNTs
ρ_{m_1}	density for first nanoparticle in HNF
ρ_{m_2}	density for second nanoparticle in HNF
κ_f	thermal conductance for basefluid
κ_{nf}	thermal conductance for nanofluid
κ_{hnf}	thermal conductance for HNF
κ_{CNTs}	thermal conductance for CNTs

κ_{m_1}	thermal conductance for first nanoparticle in HNF
κ_{m_2}	thermal conductance for second nanoparticle in HNF
$(c_p)_f$	specific heat for basefluid
$(c_p)_{nf}$	specific heat for nanofluid
$(c_p)_{hnf}$	specific heat for HNF
$(c_p)_{CNTs}$	specific heat for CNTs
$(c_p)_{m_1}$	specific heat for first nanoparticles in HNF
$(c_p)_{m_2}$	specific heat for second nanoparticles in HNF
$(c_p)_{np}$	specific heat of nanoparticle
α_f	thermal diffusivity for basefluid
α_{nf}	thermal diffusivity for nanofluid
α_{hnf}	thermal diffusivity for HNF
α_{CNTs}	thermal diffusivity for CNTs
α_{m_1}	thermal diffusivity for first nanoparticle in HNF
α_{m_2}	thermal diffusivity for second nanoparticle in HNF
β_f	coefficient of thermal expansion for basefluid
β_{nf}	coefficient of thermal expansion for nanofluid
β_{hnf}	coefficient of thermal expansion for HNF
β_{CNTs}	coefficient of thermal expansion for CNTs
β_{m_1}	coefficient of thermal expansion for first nanoparticle in HNF
β_{m_2}	coefficient of thermal expansion for second nanoparticle in HNF
υ_f	kinematic viscosity for basefluid
υ_{nf}	kinematic viscosity for nanofluid
υ_{hnf}	kinematic viscosity for HNF
υ_{CNTs}	kinematic viscosity for CNTs
υ_{m_1}	kinematic viscosity for first nanoparticle in HNF
υ_{m_2}	kinematic viscosity for second nanoparticle in HNF
μ_f	absolute viscosity for basefluid
μ_{nf}	absolute viscosity for nanofluid
μ_{hnf}	absolute viscosity for HNF

μ_{CNTs}	absolute viscosity for CNTs
μ_{m_1}	absolute viscosity for first nanoparticle in HNF
μ_{m_2}	absolute viscosity for second nanoparticle in HNF
C	concentration of specie
D_B	mass diffusivity
λ	porosity parameter
λ^*	slip coefficient
λ_1	latent heat of fluid
λ_2	relaxation to retardation times ratio
λ_3	retardation time
λ_4	mixed convection parameter
λ_5	slip parameter
$A,\ B$	chemical species
$a,\ b$	concentration of species A and B
$D_A,\ D_B$	mass diffusion of species $A,\ B$
$k_1,\ k_s$	rate constants
k_2	Boltzman constant
k_p	permeability of porous media
k^*	mean absorption coefficient
K^*	strength of homogeneous reaction parameter
K^{**}	strength of heterogeneous reaction parameter
$\mathcal{L}_f,\ \mathcal{L}_\theta,\ \mathcal{L}_\phi$	auxiliary linear operators
$\hbar_f,\ \hbar_\theta,\ \hbar_\phi$	convergence parameters
$f_0,\ \theta_0,\ \phi_0$	initial approximations (guesses)
$U_w(x)$	stretching or wall velocity in x-direction
$U_w(y)$	stretching or wall velocity in y-direction
$U_e(x)$	Free stream velocity
U_0	reference velocity
U_∞	reference free stream velocity
V_0	suction or injection coefficient

v_h	squeezing velocity
T	dimensional temperature
T_f	Temperature of the fluid
T_h	upper plate temperature
T_0	solid surface temperature
T_m	melting surface temperature
T_∞	ambient temperature
R^*	radiation parameter
γ_0	heat transfer coefficient (convective boundary condition)
γ_1	mass transfer coefficient
h^*	heat transfer coefficient (Newtonian heating condition)
β	Deborah number
β_1	thermal Biot number
β_2	mass Biot number
α^*	conjugate parameter
α	wall thickness parameter
Sq	squeezing parameter
Ec	Eckert number
E_G	local entropy generation
Ω	non-dimensional temperature difference
S_{G_0}	characteristic entropy
c	arbitrary constant
k	number of iterations
σ^*	Stefan Boltzman constant
σ_1	dimensionless reaction rate
σ	electrical conductivity
δ	temperature difference parameter
R	radius of the cylinder
γ	curvature parameter
Ha	Hartman number

E_1	activation energy
E	dimensionless activation energy
n	fitted rate constant
a^*	positive dimensional constant
S	suction or injection parameter
D_T	thermophoretic diffusion
D_{B^*}	Brownian diffusion
$N_t,\ N_b$	thermophoretic and Brownian motion parameters
Le	Lewis number
Sc	Schmidt number
M	melting parameter
$\Pr$	Prandtl number
m	power index or shape parameter
$f'(\eta),\ \theta(\eta),\ \phi(\eta)$	dimensionless velocity, temperature and concentration
q_w	heat flux
$Nu_x,\ Nu_s$	local Nusselt number
$\tau_{wx},\ \tau_{wy}$	wall shear stress in x and y-directions respectively
$C_{fx},\ C_{fy}$	skin friction coefficient in x and y-directions respectively
a_0	positive dimensional constant
$C_w,\ C_h$	concentration at lower and upper plates
C_f	concentration of fluid

1.2 Introduction

Here we organize some literature regarding nanomaterials (nanofluids), stretchable surface, squeezed flow, melting heat effect and stagnation flow. Mathematical modeling for fluid flow expressions (continuity, momentum, energy and concentration equations) in case of viscous and Jeffrey fluids. Moreover fundamental concepts of OHAM and Bvp4c methods for series and numerical solutions are incorporated respectively.

1.3 Background

Nanomaterial is the suspension nano-sized (0-100nm) particles in to baseliquid. This suspension is known as nanofluid (nanomaterial) while the suspended particles are referred as nanoparticles. These particles are made from metal nitrides (SiN, AIN), carbon ceramics (Tic, Sic), metals (Au, Ag, Cu) and oxide ceramics (CNTs, graphite, diamonds) etc. Water engine oil, ethylene glycol, gasoline oil, kerosene oil and diesel oil etc., are used as basefluids. In most of the industrial and technological processes, these baseliquids are utilized as cooling agents. Such baseliquids possess very small thermophysical characteristics like specific heat, density, and thermal conductance. Also it is a known fact aforementioned characteristics of solid substances are more when compared with liquids. Thus addition of solid nano-sized (0-100nm) particles in baseliquid highly intensifies the thermophysical characteristics of resulting material (nanofluid). Initial work in this region is done by Choi and Eastman [1]. Moreover thermophysical characteristics of resulting material (nanofluid) highly depends upon shape and size of the dispersed particles (nanoparticles). Elias et al. [2] noted that such characteristics of nanomaterials can be highly effected by nanotubes (cylindrical shaped) followed by spherical shaped, brick shaped and blade shaped nanoparticles respectively. Potentials of CNTs cannot be denied possessing stiffness and elasticity properties. CNTs are cylindrical shaped seamless substances which are surrounded by multiple (MWCNTs) or single (SWCNTs) graphene layers. CNTs are used in health care process, medical instruments and biosensors. A USA company SELDON TECHNOLOGIES has constructed a plant (filtering system) for the purification of drinking water. Such plant removes microbes like pathogens, bacteria and viruses from water without addition of any chemical and giving heat. Electronic usage of CNTs include lithium-ion batteries, data storages, transistors, solar storages and semiconductors etc. [3]. Recently a new class of nanomaterial's have been developed via addition of multiple (more than one) nanoparticles in the same basefluid. Such new class of nanomaterial is referred as hybrid nanofluid [4,5]. Hybrid nanofluids are acknowledged most suitable than ordinary nanofluids. Hybrid nanofluids possess advanced properties in comparison to nanofluids. Different models of nanofluids such as single phased, two phased, Tiwari and Das, CNTs, Boungiorno model etc., are used to analyze nanotechnology [6-13]. Heat transport through radiation with slip boundary condition in flow of nanomaterial is elaborated by Souayeh et al. [14]. Soltani et al. [15] performed an experimental work on applications of hybrid nanomaterial. Analysis of MHD nanofluid via two-phase model is incorporated by Sheikholeslami and Rokni [16]. Khan et al. [17] examined reduction of entropy in chemically reactive MHD flow of Sisko nanofluid in region with stagnation point. Heat transfer via natural convection in MHD flow of nanomaterial is numerically elaborated by Mohebbi et al. [18]. Hassanan et al. [19] analyzed heat transfer in flow of nanomaterial (CNTs+Water) over a stretched surface. Entropy production rate reduction in Bödewadt flow of water-based nanomaterial is examined by Muhammad et al. [20].

Flow over a stretched surface has gained much attention in various technological and industrial purposes. Such flow occurs in fiber spinning, glass blowing, cooling of metallic plates via bath, moving of plastic films continuously, plastic sheet extrusion, heating of material moving between wind-up roll and feed roll etc. In this domain initial analysis was presented by Crane [21]. Entropy generation and chemical reactions in non-Newtonian (Sisko) fluid flow is presented by Khan et al. [22]. MHD flow of hybrid nanomaterial with Joule heating is explored by Khashi'ie et al. [23]. Hayat et al. [24] examined flow of Jeffrey material over a stretching surface of variable thickness in presence of heat generation. Second-grade fluid flow and heat transport via Cattaneo-Christov heat flux is investigated by Alamari et al. [25]. Khan et al. [26] inquired entropy generation in flow of CNTs bounded by two stretchable disks. MHD unsteady flow of viscous fluid by a curved stretching surface is due to Naveed et al. [27]. Numerical study regarding flow of hybrid nanofluid (CNTs+$C_2H_6O_2$+Water) by a stretched cylinder is performed by Gholinia et al. [28]. MHD flow of Williamson fluid with variable thermal conductance and thermal radiation by a stretched cylinder is elaborated by Bilal et al. [29]. Heat transport in squeezed flow of non-Newtonian fluid (third-grade fluid) via Cattaneo-Christov heat flux and melting heat is expressed by Muhammad et al. [30].

Squeezed flow between two plates is an interesting topic for the researchers. The compactness or deformation of a material occurs when both plates moves away or towards each other. For technological and industrial point of view squeezed flow is very important. Applications of squeezed flow in engineering processes are the construction of dampers via electrorheological fluids, lubrication process, polymers and metal moulding etc. During formation of foams, the bubble boundaries are explored biaxially while shrinked in thickness [31]. Squeezed flow was initially examined by Stefan [32]. Heat transport via mixed convection in squeezed flow is explored by Hayat et al. [33]. Qayyum et al. [34] considered time-dependent squeezing flow of Jeffrey material. Heat transport in nanomaterial squeezed flow is examined by Hayat et al. [35]. MHD effect in squeezing flow of Jeffrey fluid is presented by Muhammad et al. [36]. Squeezing flow subject to rotation and Cattaneo-Christov heat flux is studied by Hayat et al. [37]. Gupta and Ray [38] explored squeezed flow of nanomaterial numerically. Chemical reactions in squeezing flow between Riga plates with convective condition is elaborated by Hayat et al. [39]. Squeezed flow of nanomaterial using ADM (Adomian decomposition method) for solution development is presented by Sheikholeslami et al. [40].

Recently researchers have shown a considerable concern in order to improve energy storages and cooling/heating rate in different modern technologies. Regarding these requirements various flow problems are modeled assuming various fluid models. Main goal for researcher is that to construct outstanding energy storages via minimal price. Generally for energy storage process three approaches are utilized which are latent heat, sensible heat and chemical/thermal energy. Amongst these approaches, latent heat is considered more appropriate. In this process thermal energy is added or stored in a material via latent heat while it is recovered again by melting. Melting and solidification play a vital role in mechanical process. Applications of melting phenomenon include welding process, crystal development, treatment of sewage via freezing, magma solidification and production of semiconductors. In this area initial work is done by Robert [41]. Melting effect in flow of Maxwell fluid is explored by Hayat et al. [42]. Das [43] examined melting heat and radiation effects during MHD flow by a movable surface. Melting effect in stagnation point flow of micropolar fluid is analyzed by Yacob et al. [44] while same analysis for viscous fluid is due to Bashok et al. [45]. Ho and Gao [46] studied heat transport via melting in flow of nanomaterial (Al_2O_3+Paraffin). Melting phenomenon in flow of Oldroyd-B fluid by a variable thicked sheet is due to Hayat et al. [47]. Gireesha et al. [48] examined melting effect in MHD flow past a stretching surface in region of stagnation point. Heat generation and melting heat effects in Jeffrey material flow by a non-linear stretched sheet is explored by Hayat et al. [49]. Heat transfer through melting effect in Burgers material flow is analyzed by Awais et al. [50].

A point on the surface of an object placed in flow field at which the local velocity of fluid becomes zero is referred as stagnation point. At this region the value of static pressure is maximum which causes fluid flow. Stagnation points are either orthogonal or oblique. When fluid particles strike surface of the object placed in flow field orthogonally (normally) and as a consequence its local velocity becomes zero is called orthogonal stagnation point while when fluid particles strike such surface the object with a certain angle other than 90 degree and as a result its local velocity becomes zero is called oblique stagnation point. In both natural and industrial point of view the flow behavior in stagnation region is too much important. Such flow can be analyzed for viscous/inviscid, symmetric/asymmetric, steady/unsteady, normal/oblique, two-dimensional/three-dimensional, forward/reverse, homogeneous/two immiscible fluids [51]. Examples of stagnation flow are flow over submarines, rockets, oil ships, air craps etc. Flow of blood at a junction through an artery is an example of stagnation flow in human body. Heat transport in flow by a stretched sheet regarding stagnation point is elaborated by Mahapatra and Gupta [52]. Pop et al. [53] analyzed radiation in stagnation flow over a stretching surface. MHD stagnation flow with heat source/sink and variable thermal conductance is examined by Sharma and Singh [54]. Few analyses regarding stagnation point flows can be seen in Refs. [55-60].

1.4 Basic laws and its corresponding flow equations

1.4.1 Mass conservation law

Equation based on this law is called continuity equation. This law states that mass can neither be created nor destroyed. Mathematically we have

$$\frac{\partial \rho_f}{\partial t} + \mathrm{div}(\rho_f \mathbf{V}) = 0. \tag{1.1}$$

For an incompressible fluid we have

$$\mathrm{div}(\mathbf{V}) = 0. \tag{1.2}$$

Using velocity distribution

$$\mathbf{V} = (u_1(x,\ y,\ z),\ u_2(x,\ y,\ z),\ u_3(x,\ y,\ z)) \tag{1.3}$$

Eq. 1.2 takes the form

$$\frac{\partial u_1}{\partial x} + \frac{\partial u_2}{\partial y} + \frac{\partial u_3}{\partial z} = 0, \quad \text{(Cartesian coordinates}(x,\ y,\ z)), \tag{1.4}$$

while using velocity distribution

$$\mathbf{V} = (u_r(r,\ \overline{\theta},\ z),\ u_{\overline{\theta}}(r,\ \overline{\theta},\ z),\ u_z(r,\ \overline{\theta},\ z)) \tag{1.5}$$

we have

$$\frac{\partial u_r}{\partial r} + \frac{u_r}{r} + \frac{1}{r}\frac{\partial u_{\overline{\theta}}}{\partial \overline{\theta}} + \frac{\partial u_z}{\partial z} = 0 \quad \text{(cylindrical coordinates}(r,\ \overline{\theta},\ z)). \tag{1.6}$$

1.4.2 Momentum conservation law

Momentum conservation law states that momentum of a system remains conserved. Further derivation of momentum equation is based on Newton's second law of motion. Mathematically

$$\rho_f \frac{d\mathbf{V}}{dt} = \mathrm{div}(\boldsymbol{\tau}) + \rho_f \overline{\mathbf{b}}. \tag{1.7}$$

L.H.S of this expression represents inertial forces while on R.H.S first term denotes surface forces and second term on R.H.S depicts body forces. Here $\frac{d}{dt}$ is material derivative defined by

$$\frac{d}{dt} = \frac{\partial}{\partial t} + \mathbf{V}.\boldsymbol{\nabla}. \tag{1.8}$$

In Cartesian coordinates $(x,\ y,\ z)$ one has

$$\frac{d}{dt} = \frac{\partial}{\partial t} + u_1\frac{\partial}{\partial x} + u_2\frac{\partial}{\partial y} + u_3\frac{\partial}{\partial z}, \tag{1.9}$$

and in cylindrical coordinates $(r,\ \overline{\theta},\ z)$

$$\frac{d}{dt} = \frac{\partial}{\partial t} + u_r\frac{\partial}{\partial r} + \frac{u_{\overline{\theta}}}{r}\frac{\partial}{\partial \overline{\theta}} - \frac{u_{\overline{\theta}}^2}{r} + u_z\frac{\partial}{\partial z}. \tag{1.10}$$

For an incompressible fluid

$$\boldsymbol{\tau} = -p\mathbf{I} + \mathbf{S}, \tag{1.11}$$

$$\boldsymbol{\tau} = \begin{pmatrix} \tau_{xx} & \tau_{xy} & \tau_{xz} \\ \tau_{yx} & \tau_{yy} & \tau_{yz} \\ \tau_{zx} & \tau_{zy} & \tau_{zz} \end{pmatrix} \quad \text{(Cartesian coordinates}(x,\ y,\ z)), \tag{1.12}$$

and

$$\boldsymbol{\tau} = \begin{pmatrix} \tau_{rr} & \tau_{r\overline{\theta}} & \tau_{rz} \\ \tau_{\overline{\theta}r} & \tau_{\overline{\theta\theta}} & \tau_{\overline{\theta}z} \\ \tau_{zr} & \tau_{z\overline{\theta}} & \tau_{zz} \end{pmatrix} \quad \text{(cylindrical coordinates}(r,\ \overline{\theta},\ z)). \tag{1.13}$$

Using Cartesian coordinates $(x,\ y,\ z)$ with velocity distribution

$$\mathbf{V} = (u_1(x,\ y,\ z,\ t),\ u_2(x,\ y,\ z,\ t),\ u_3(x,\ y,\ z,\ t)) \tag{1.14}$$

momentum equation in components form can be expressed as

$$\rho_f(\frac{\partial}{\partial t} + \mathbf{V}.\boldsymbol{\nabla})u_1 = \frac{\partial}{\partial x}(\tau_{xx}) + \frac{\partial}{\partial y}(\tau_{xy}) + \frac{\partial}{\partial z}(\tau_{xz}) + \rho_f b_x, \tag{1.15}$$

$$\rho_f(\frac{\partial}{\partial t} + \mathbf{V}.\boldsymbol{\nabla})u_2 = \frac{\partial}{\partial x}(\tau_{yx}) + \frac{\partial}{\partial y}(\tau_{yy}) + \frac{\partial}{\partial z}(\tau_{yz}) + \rho_f b_y, \tag{1.16}$$

$$\rho_f(\frac{\partial}{\partial t} + \mathbf{V}.\boldsymbol{\nabla})u_3 = \frac{\partial}{\partial x}(\tau_{zx}) + \frac{\partial}{\partial y}(\tau_{zy}) + \frac{\partial}{\partial z}(\tau_{zz}) + \rho_f b_z. \tag{1.17}$$

Using cylindrical coordinates $(r,\ \overline{\theta},\ z)$ and velocity distribution

$$\mathbf{V} = (u_r(r,\ \overline{\theta},\ z,\ t),\ u_{\overline{\theta}}(r,\ \overline{\theta},\ z,\ t),\ u_z(r,\ \overline{\theta},\ z,\ t)), \tag{1.18}$$

we have

$$\rho_f(\frac{\partial}{\partial t} + \mathbf{V}.\boldsymbol{\nabla})u_r = \frac{\partial}{\partial r}(\tau_{rr}) + \frac{\tau_{rr}}{r} - \frac{\tau_{\overline{\theta\theta}}}{r} + \frac{1}{r}\frac{\partial}{\partial\overline{\theta}}(\tau_{r\overline{\theta}}) + \frac{\partial}{\partial z}(\tau_{rz}) + \rho_f b_r, \tag{1.19}$$

$$\rho_f(\frac{\partial}{\partial t} + \mathbf{V}.\boldsymbol{\nabla})u_{\overline{\theta}} = \frac{\partial}{\partial r}(\tau_{\overline{\theta}r}) + \frac{\tau_{r\overline{\theta}}}{r} + \frac{\tau_{\overline{\theta}r}}{r} + \frac{1}{r}\frac{\partial}{\partial\overline{\theta}}(\tau_{\overline{\theta\theta}}) + \frac{\partial}{\partial z}(\tau_{\overline{\theta}z}) + \rho_f b_{\overline{\theta}}, \tag{1.20}$$

$$\rho_f(\frac{\partial}{\partial t} + \mathbf{V}.\boldsymbol{\nabla})u_z = \frac{\partial}{\partial r}(\tau_{zr}) + \frac{\tau_{zr}}{r} + \frac{1}{r}\frac{\partial}{\partial\overline{\theta}}(\tau_{z\overline{\theta}}) + \frac{\partial}{\partial z}(\tau_{zz}) + \rho_f b_z. \tag{1.21}$$

1.4.3 Energy conservation law

Mathematically

$$\rho_f(c_p)_f \frac{dT}{dt} = \mathrm{Trace}(\boldsymbol{\tau}.\,\mathrm{grad}(\mathbf{V})) - \mathbf{q}_r - \mathrm{div}(\mathbf{q}). \tag{1.22}$$

L.H.S of this equation represent total internal energy while on R.H.S first term is due to viscous dissipation, second term for thermal and third for radiative heat flux. Here $\mathbf{q}_r$ and $\mathbf{q}$ are described by Stefan Boltzman law and Fourier's law of heat conduction respectively.

1.4.4 Mass transport equation

This equation basically represents that total concentration of a system under consideration remain conserved. Derivation of mass transfer equation is based on Fick's second law. Mathematically in absence of chemical reaction one can write

$$\frac{dC}{dt} = -\,\mathrm{div}(\mathbf{j}), \tag{1.23}$$

$$\mathbf{j} = -D_B\,\mathrm{grad}(C) \quad \text{(Fick's first law)}. \tag{1.24}$$

Thus we get

$$\frac{dC}{dt} = D_B\,\mathrm{div}(\mathrm{grad}(C))$$

or

$$\frac{dC}{dt} = \boldsymbol{\nabla}^2 D_B C. \tag{1.25}$$

1.5 Boundary layer expressions under consideration

This thesis is based on boundary layer flow of viscous and Jeffrey fluids.

1.5.1 Viscous fluid

These are the fluids in which shear stress and rate of deformation are directly proportional to each other in a linear way. Further Newton's law of viscosity holds for these fluids. Cauchy stress tensor satisfies

$$\boldsymbol{\tau} = -p\mathbf{I} + \mathbf{S}. \tag{1.26}$$

For viscous fluids

$$\mathbf{S} = \mu \mathbf{A}_1, \tag{1.27}$$

with

$$\mathbf{A}_1 = \mathrm{grad}(\mathbf{V}) + (\mathrm{grad}(\mathbf{V}))^{Transpose}. \tag{1.28}$$

Velocity distribution is

$$\mathbf{V} = (u_x(x,\ y,\ z) = u(x,\ y,\ z),\ u_y(x,\ y,\ z) = v(x,\ y,\ z),\ u_z(x,\ y,\ z) = w(x,\ y,\ z)). \tag{1.29}$$

For three-dimensional flow we have

$$\mathrm{grad}(\mathbf{V}) = \begin{pmatrix} \frac{\partial u}{\partial x} & \frac{\partial u}{\partial y} & \frac{\partial u}{\partial z} \\ \frac{\partial v}{\partial x} & \frac{\partial v}{\partial y} & \frac{\partial v}{\partial z} \\ \frac{\partial w}{\partial x} & \frac{\partial w}{\partial y} & \frac{\partial w}{\partial z} \end{pmatrix}, \tag{1.30}$$

$$(\mathrm{grad}(\mathbf{V}))^{Transpose} = \begin{pmatrix} \frac{\partial u}{\partial x} & \frac{\partial v}{\partial x} & \frac{\partial w}{\partial x} \\ \frac{\partial u}{\partial y} & \frac{\partial v}{\partial y} & \frac{\partial w}{\partial y} \\ \frac{\partial u}{\partial z} & \frac{\partial v}{\partial x} & \frac{\partial w}{\partial z} \end{pmatrix}, \tag{1.31}$$

$$\mathbf{A}_1 = \begin{pmatrix} 2\frac{\partial u}{\partial x} & \frac{\partial u}{\partial y} + \frac{\partial v}{\partial x} & \frac{\partial u}{\partial z} + \frac{\partial w}{\partial x} \\ \frac{\partial v}{\partial x} + \frac{\partial u}{\partial y} & 2\frac{\partial v}{\partial y} & \frac{\partial v}{\partial z} + \frac{\partial w}{\partial y} \\ \frac{\partial w}{\partial x} + \frac{\partial u}{\partial z} & \frac{\partial w}{\partial y} + \frac{\partial v}{\partial x} & 2\frac{\partial w}{\partial z} \end{pmatrix}, \tag{1.32}$$

and

$$\mathbf{I} = \begin{pmatrix} 1 & 0 & 0 \\ 0 & 1 & 0 \\ 0 & 0 & 1 \end{pmatrix}. \tag{1.33}$$

Thus

$$\boldsymbol{\tau} = \begin{pmatrix} -p + 2\mu\frac{\partial u}{\partial x} & \mu(\frac{\partial u}{\partial y} + \frac{\partial v}{\partial x}) & \mu(\frac{\partial u}{\partial z} + \frac{\partial w}{\partial x}) \\ \mu(\frac{\partial v}{\partial x} + \frac{\partial u}{\partial y}) & -p + 2\mu\frac{\partial v}{\partial y} & \mu(\frac{\partial v}{\partial z} + \frac{\partial w}{\partial y}) \\ \mu(\frac{\partial w}{\partial x} + \frac{\partial u}{\partial z}) & \mu(\frac{\partial w}{\partial y} + \frac{\partial v}{\partial x}) & -p + 2\mu\frac{\partial w}{\partial z} \end{pmatrix}. \tag{1.34}$$

Component form of expressions for steady flow are

$$\rho_f(\mathbf{V}.\boldsymbol{\nabla})u = \frac{\partial}{\partial x}(-p+2\mu\frac{\partial u}{\partial x}) + \frac{\partial}{\partial y}(\mu(\frac{\partial u}{\partial y}+\frac{\partial v}{\partial x})) + \frac{\partial}{\partial z}(\mu(\frac{\partial u}{\partial z}+\frac{\partial w}{\partial x})), \tag{1.35}$$

$$\rho_f(\mathbf{V}.\boldsymbol{\nabla})v = \frac{\partial}{\partial x}(\mu(\frac{\partial v}{\partial x}+\frac{\partial u}{\partial y})) + \frac{\partial}{\partial y}(-p+2\mu\frac{\partial v}{\partial y}) + \frac{\partial}{\partial z}(\mu(\frac{\partial v}{\partial z}+\frac{\partial w}{\partial y})), \tag{1.36}$$

$$\rho_f(\mathbf{V}.\boldsymbol{\nabla})w = \frac{\partial}{\partial x}(\mu(\frac{\partial w}{\partial x}+\frac{\partial u}{\partial z})) + \frac{\partial}{\partial y}(\mu(\frac{\partial w}{\partial y}+\frac{\partial v}{\partial x})) + \frac{\partial}{\partial z}(-p+2\mu\frac{\partial w}{\partial z}). \tag{1.37}$$

Implementing boundary layer assumptions for 2D flow $u = v = x = y = O(1)$, $w = z = O(\delta)$ while $u = x = O(1)$, $v = w = O(\delta)$, we get the finalized form as follows

$$\rho_f(u\frac{\partial u}{\partial x} + v\frac{\partial u}{\partial y}) = -\frac{\partial p}{\partial x} + \mu\frac{\partial^2 u}{\partial y^2}.$$

In cylindrical coordinates $(r,\ \overline{\theta},\ z)$ with velocity distribution

$$\mathbf{V} = (u_r(r,\ 0,\ z) = v,\ 0,\ u_z(r,\ 0,\ z) = u), \tag{1.38}$$

one can write

$$\text{grad}(\mathbf{V}) = \begin{pmatrix} \frac{\partial u_r}{\partial r} & 0 & \frac{\partial u_r}{\partial z} \\ 0 & \frac{u_r}{r} & 0 \\ \frac{\partial u_z}{\partial r} & 0 & \frac{\partial u_z}{\partial z} \end{pmatrix}, \tag{1.39}$$

$$(\text{grad}(\mathbf{V}))^{Transpose} = \begin{pmatrix} \frac{\partial u_r}{\partial r} & 0 & \frac{\partial u_z}{\partial r} \\ 0 & \frac{u_r}{r} & 0 \\ \frac{\partial u_r}{\partial z} & 0 & \frac{\partial u_z}{\partial z} \end{pmatrix}, \tag{1.40}$$

$$\mathbf{A}_1 = \begin{pmatrix} 2\frac{\partial u_r}{\partial r} & 0 & \frac{\partial u_r}{\partial z} + \frac{\partial u_z}{\partial r} \\ 0 & 2\frac{u_r}{r} & 0 \\ \frac{\partial u_z}{\partial r} + \frac{\partial u_r}{\partial z} & 0 & 2\frac{\partial u_z}{\partial z} \end{pmatrix}. \tag{1.41}$$

$$\boldsymbol{\tau} = \begin{pmatrix} -p+2\mu\frac{\partial u_r}{\partial r} & 0 & \mu(\frac{\partial u_r}{\partial z} + \frac{\partial u_z}{\partial r}) \\ 0 & -p+2\mu\frac{u_r}{r} & 0 \\ \mu(\frac{\partial u_z}{\partial r} + \frac{\partial u_r}{\partial z}) & 0 & -p+2\mu\frac{\partial u_z}{\partial z} \end{pmatrix}. \tag{1.42}$$

After implementing boundary layer approximations $u_z = z = O(1)$, $u_r = r = O(\delta)$, we get

$$\rho_f(u_z\frac{\partial u_z}{\partial x} + u_r\frac{\partial u_z}{\partial r}) = -\frac{\partial p}{\partial z} + \mu\frac{\partial^2 u_z}{\partial r^2} + \frac{\mu}{r}\frac{\partial u_z}{\partial r}. \tag{1.43}$$

1.5.2 Jeffrey fluid

Jeffrey fluid is the non-Newtonian fluid which describes rheological feature of linear viscoelastic fluids. This fluid lies in rate type category which describes relaxation and retardation time features. Examples of Jeffrey fluid are fiber orientation and dilute polymer solution etc. For Jeffrey fluid the extra stress tensor satisfies

$$\mathbf{S} = \frac{\mu}{1+\lambda_2} + (\mathbf{A}_1 + \lambda_3\frac{d\mathbf{A}_1}{dt}). \tag{1.44}$$

In cylindrical coordinates $(r,\ \overline{\theta},\ z)$ with velocity distribution

$$\mathbf{V} = (u_r(r,\ 0,\ z) = v,\ 0,\ u_z(r,\ 0,\ z) = u), \tag{1.45}$$

For two-dimensional flow, we have

$$\tau_{rr} = -p + \frac{\mu}{1+\lambda_2}(2\frac{\partial u_r}{\partial r} + \lambda_3(2u_r\frac{\partial^2 u_r}{\partial r^2} + 2u_z\frac{\partial^2 u_r}{\partial r\partial z})), \tag{1.46}$$

$$\tau_{\overline{\theta\theta}} = -p + \frac{\mu}{1+\lambda_2}(2\frac{u_r}{r} + \lambda_3(2\frac{u_r}{r}\frac{\partial u_r}{\partial r} - 2\frac{u_r^2}{r^2} + 2\frac{u_z}{r}\frac{\partial u_r}{\partial z})), \tag{1.47}$$

$$\tau_{zz} = -p + \frac{\mu}{1+\lambda_2}(2\frac{\partial u_z}{\partial z} + \lambda_3(2u_r\frac{\partial^2 u_z}{\partial z\partial r} + 2u_z\frac{\partial^2 u_z}{\partial z^2})), \tag{1.48}$$

$$\tau_{rz} = \tau_{zr} = \frac{\mu}{1+\lambda_2}((\frac{\partial u_r}{\partial z} + \frac{\partial u_z}{\partial r}) + \lambda_3(u_r\frac{\partial^2 u_r}{\partial r\partial z} + u_r\frac{\partial^2 u_z}{\partial r^2} + u_z\frac{\partial^2 u_r}{\partial z^2} + u_z\frac{\partial^2 u_z}{\partial r\partial z})). \tag{1.49}$$

After implementing boundary layer approximations $u_z = z = O(1)$, $u_r = r = O(\delta)$, we get

$$\rho_f(u_z\frac{\partial u_z}{\partial z} + u_r\frac{\partial u_z}{\partial r}) = -\frac{\partial p}{\partial z} + \frac{\mu}{1+\lambda_2}(\frac{1}{r}\frac{\partial u_r}{\partial r} + \frac{\partial^3 u_z}{\partial r^3} + \lambda_3\left(\begin{array}{c} \frac{u_r}{r}\frac{\partial^2 u_z}{\partial r^2} + \frac{\partial^2 u_z}{\partial r^2}\frac{\partial u_r}{\partial r} + \\ u_r\frac{\partial^3 u_z}{\partial r^3} + \frac{u_z}{r}\frac{\partial^2 u_z}{\partial r\partial z} + \\ \frac{\partial^2 u_z}{\partial r\partial z} + \frac{\partial u_z}{\partial r}\frac{\partial^2 u_z}{\partial r\partial z} + u_r\frac{\partial^3 u_z}{\partial z\partial r^2} \end{array}\right)). \tag{1.50}$$

1.6 Solutions methodologies

Non-linear system of ODEs (ordinary differential equations) are solved via OHAM (analytically) in chapters 5, 6 and 7 while via bvp4c (numerically) in chapters 2, 3, 4, 8, 9 and 10.

1.6.1 Optimal homotopy analysis method (OHAM)

This method is based on HAM (Homotopy analysis method) using BVPh 2.0 mathematica package [61-65]. This method only require to define governed equations along with boundary conditions. Further we select proper auxiliary operators ($\mathcal{L}_f$, $\mathcal{L}_\theta$, $\mathcal{L}_\phi$) and initial guesses (f_0, θ_0, ϕ_0) corresponding to each unknown function. Bvph 2.0 generate analytical approximations to the solutions automatically after the aforementioned inputs.

1.6.2 Bvp4c Method

This method (bvp4c) is based on shooting method with Runge-Kutta algorithm. This methodology works for first order ODEs. Thus first we convert the governed expressions into systems of first order ODEs [66-70].

Chapter 2

Melting effect in chemically reactive flow of CNTs

2.1 Introduction

This chapter concentrates on melting effect in three-dimensional flow of CNTs (SWCNTs, MW-CNTs) over a stretching surface. Flow analysis is performed in presence of chemical reactions and porous medium. Carbon nanotubes (CNTs) are dispersed in water-basedliquid for development of nanomaterial. Non-linear differential system is obtained through adequate transformations from flow, heat and mass expressions. Shooting method (bvp4c) is implemented for solutions development. Velocity distribution and temperature under influential variable are elaborated graphically while skin friction and Nusselt number are evaluated numerically. Moreover comparison between MWCNTs and SWCNTs is performed.

2.2 Mathematical Modeling

Consider three-dimensional flow of nanofluid over an impermeable stretchable boundary. Fluid saturates the porous medium. Present flow is subject to melting heat and homogeneous-heterogeneous reactions. CNTs are utilized in water. Moreover viscous dissipation and thermal radiation are neglected. Cartesian coordinates are chosen. Heat released during the reaction is also

Homogeneous reaction for cubic autocatalysis is in the form:

$$A + 2B \rightarrow 3B, \qquad rate = k_1 ab^2, \tag{2.1}$$

while isothermal reaction of order first on the catalyst surface is

$$A \rightarrow B, \qquad rate = k_s a. \tag{2.2}$$

These equations of reactions guarantee that the rate of reaction is zero in the external flow as well on the outer edge of boundary layer. After utilizing boundary layer approximations $(o(x) = o(y) = o(u) = o(v) = o(1), o(w) = o(z) = o(\delta))$ one has

$$\frac{\partial u}{\partial x} + \frac{\partial v}{\partial y} + \frac{\partial w}{\partial z} = 0, \tag{2.3}$$

$$u\frac{\partial u}{\partial x} + v\frac{\partial u}{\partial y} + w\frac{\partial u}{\partial z} = v_{nf}(\frac{\partial^2 u}{\partial z^2} - \frac{u}{k_p}), \tag{2.4}$$

$$u\frac{\partial v}{\partial x} + v\frac{\partial v}{\partial y} + w\frac{\partial v}{\partial z} = v_{nf}(\frac{\partial^2 v}{\partial z^2} - \frac{v}{k_p}), \tag{2.5}$$

$$u\frac{\partial T}{\partial x} + v\frac{\partial T}{\partial y} + w\frac{\partial T}{\partial z} = \alpha_{nf}\frac{\partial^2 T}{\partial z^2}, \tag{2.6}$$

$$u\frac{\partial a}{\partial x} + v\frac{\partial a}{\partial y} + w\frac{\partial a}{\partial z} = D_A\frac{\partial^2 a}{\partial z^2} - k_1 ab^2, \tag{2.7}$$

$$u\frac{\partial b}{\partial x} + v\frac{\partial b}{\partial y} + w\frac{\partial b}{\partial z} = D_B\frac{\partial^2 b}{\partial z^2} + k_1 ab^2. \tag{2.8}$$

The boundary conditions are

$$u = U_w(x) = U_0 x, \quad v = U_w(y) = U_0 y, \quad T = T_m,$$

$$D_A\left(\frac{\partial a}{\partial z}\right) = k_s a, \quad D_B\left(\frac{\partial b}{\partial z}\right) = -k_s a \quad \text{at} \quad z = 0,$$

$$u \rightarrow 0, \quad v \rightarrow 0, \quad T \rightarrow T_\infty, \quad a \rightarrow a_0, \quad b \rightarrow 0 \quad \text{when} \quad z \rightarrow \infty. \tag{2.9}$$

Melting heat condition is

$$k_{nf}\left(\frac{\partial T}{\partial z}\right)_{z=0}=\rho_{nf}\left[\lambda_1+c_s(T_m-T_0)\right]w_{z=0}. \tag{2.10}$$

Xue expressions regarding CNTs flow are [20]

$$\mu_{nf}=\frac{\mu_f}{(1-\phi)^{2.5}},\qquad \nu_{nf}=\frac{\mu_{nf}}{\rho_{nf}},\qquad \rho_{nf}=(1-\phi)\,\rho_f+\phi\rho_{_{CNTs}},$$

$$\alpha_{nf}=\frac{k_{nf}}{\rho_{nf}\,(c_p)_{nf}},\qquad \frac{k_{nf}}{k_f}=\frac{(1-\phi)+2\phi\frac{k_{CNTs}}{k_{CNT}-k_f}\ln\frac{k_{CNTs}+k_f}{2k_f}}{(1-\phi)+2\phi\frac{kf}{k_{CNTs}-k_f}\ln\frac{k_{CNTs}+k_f}{2k_f}}. \tag{2.11}$$

Table. 2.1: Thermal characteristics of CNTs (SWCNTs, MWCNTs) and baseliquid (water) [20]:

Physical properties	CNTs		Baseliquid
	SWCNTs	MWCNTs	Water
$c_p(\frac{J}{kgK})$	425	796	4179
$k(\frac{W}{mK})$	6600	3000	0.613
$\rho(\frac{kg}{m^3})$	2600	1600	997

Consider transformations

$$\eta=z\sqrt{\frac{U_0}{v_f}},\qquad u=U_0xf'(\eta)\,,\qquad v=U_0yg'(\eta)\,,$$

$$w=-\sqrt{U_0v_f}(f'(\eta)+g'(\eta)),\qquad \theta(\eta)=\frac{T-T_f}{T_\infty-T_f},$$

$$h(\eta)=\frac{a}{a_0},\qquad j(\eta)=\frac{b}{a_0}. \tag{2.12}$$

Implementing these transformations Eq. 2.1 is satisfied while other equations become

$$A^*(f'''-\lambda f')-f'^2+(f+g)\,f''=0, \tag{2.13}$$

$$A^*(g'''-\lambda g')-g'^2+(f+g)\,g''=0, \tag{2.14}$$

$$A^{**}\theta'' + \Pr\left(f+g\right)\theta' = 0, \tag{2.15}$$

$$\frac{1}{Sc}h'' - K^{*}hj^{2} + \left(f+g\right)h' = 0, \tag{2.16}$$

$$\frac{\delta}{Sc}j'' - K^{*}hj^{2} + \left(f+g\right)j' = 0, \tag{2.17}$$

with

$$f'(0) = 1, \quad g'(0) = 1, \quad \frac{k_{nf}}{k_f}M\ \theta'\left(0\right) + \frac{\Pr}{A^{*}\left(1-\phi\right)^{2.5}}\left(f\left(0\right)+g\left(0\right)\right) = 0,$$

$$h'\left(0\right) = K^{**}h\left(0\right), \quad j'\left(0\right) = -\frac{K^{**}}{\delta}j\left(0\right),$$

$$f' \to 0, \quad g' \to 0, \quad \theta \to 1, \quad \text{as } \eta \to \infty. \tag{2.18}$$

In above expressions

$$A^{*} = \frac{1}{\left(1-\phi\right)^{2.5}\left(1-\phi+\phi\frac{\rho_{CNTs}}{\rho_f}\right)},$$

$$A^{**} = \frac{\frac{k_{nf}}{k_f}}{1-\phi+\phi\frac{\left(\rho c_p\right)_{CNTs}}{\left(\rho c_p\right)_f}}.$$

Involved all parameters are

$$\lambda = \frac{v_f}{ak_p}, \quad Sc = \frac{v_f}{D_A}, \quad \Pr = \frac{\mu c_p}{k_f},$$

$$K^{*} = \frac{a_0^2 k_1 x}{U_{w(x)}} = \frac{a_0^2 k_1}{a}, \quad K^{**} = \frac{k_s}{D_A}\sqrt{\frac{v_f}{a}}, \tag{2.19}$$

$$M = \frac{\left(c_p\right)_{nf}\left(T_\infty - T_m\right)}{\lambda_1 + c_s\left(T_m - T_0\right)}, \quad \delta = \frac{D_B}{D_A}.$$

Further we assumed that D_A and D_B are of comparable size. This assumption enable us that both $D_A = D_B$ for $\delta = 1$. Hence

$$h\left(\eta\right) + j\left(\eta\right) = 1. \tag{2.20}$$

Thus Eqs. 2.16 and 2.17 yield

$$\frac{1}{Sc}h'' - K^{*}h\left(1-2h\right)^{2} + \left(f+g\right)h' = 0, \tag{2.21}$$

with

$$h'(0) = K^{**} h\left(0\right), \quad h\left(\eta\right) \to 1 \quad \text{as} \quad \eta \to \infty. \tag{2.22}$$

Expressions for C_{fx}, C_{fy} and Nu_x are

$$C_{fx} = \frac{(\tau_{wx})_{z=0}}{\rho_f U_w^2}, \quad C_{fy} = \frac{(\tau_{wy})_{z=0}}{\rho_f U_w^2}, \quad Nu_x = \frac{x q_w}{k_f (T_\infty - T_f)}, \tag{2.23}$$

with

$$\tau_{wx} = \mu_{nf}(\frac{\partial u}{\partial z} + \frac{\partial w}{\partial x}), \quad \tau_{wy} = \mu_{nf}(\frac{\partial w}{\partial y} + \frac{\partial v}{\partial z}), \quad q_w = -k_{nf}(\frac{\partial u}{\partial y})_{z=0} \tag{2.24}$$

Dimensionless coefficient of skin friction and Nusselt number satisfy

$$C_{fx}\sqrt{\mathrm{Re}} = \frac{1}{(1-\phi)^{2.5}} f''(0), \quad C_{fy}\sqrt{\mathrm{Re}} = \frac{1}{(1-\phi)^{2.5}} g''(0), \quad \frac{Nu_x}{\sqrt{\mathrm{Re}^{-}}} = -\frac{k_{nf}}{k_f}\theta'(0). \tag{2.25}$$

In aforementioned equations $\mathrm{Re} = \frac{U_0}{\nu_f}(x+y)$ is the Reynolds number.

Table. 2.2**:** Evaluation of coefficient of skin friction and Nusselt number under influential variables in both single and multi-wall CNTs cases when $K^* = 0.2$, $K^{**} = 1.2$ and $Sc = 0.8$.

Parameters			SWCNTs	MWCNTs	SWCNTs	MWCNTs	SWCNTs	MWCNTs
ϕ	M	λ	$C_{fx}\sqrt{\mathrm{Re}}$	$C_{fx}\sqrt{\mathrm{Re}}$	$C_{fy}\sqrt{\mathrm{Re}}$	$C_{fy}\sqrt{\mathrm{Re}_y}$	$\frac{Nu_x}{\sqrt{\mathrm{Re}}}$	$\frac{Nu_x}{\sqrt{\mathrm{Re}}}$
0.1	0.5	0.5	-1.68714	-1.63180	-1.68720	-1.63187	-3.63323	-3.55854
0.2			-2.15488	-2.03959	-2.15500	-2.03976	-4.44146	-4.41693
0.3			-2.80679	-2.87050	-2.87050	-2.62161	-5.03448	-5.06319
0.1	0.2	0.5	-2.15488	-1.64363	-1.67920	-1.64371	-3.69830	-3.63775
	0.6		-1.69066	-1.62798	-1.68372	-1.63806	-3.61215	-3.53305
	1.0		-1.67020	-1.61331	-1.69432	-1.61339	-3.53067	-.43530
0.1	0.5	0.0	-1.42409	-1.35847	-1.42411	-1.35849	-3.75571	-3.67827
		0.5	-1.68714	-1.63180	-1.68720	-1.63187	-3.63323	-3.55854
0.1	0.5	1.0	-1.91740	-1.86883	-1.91742	-1.86885	-3.52595	-3.45443

2.3 Analysis

Aim here is to interpret impacts of influential variables on the velocity, temperature, skin friction coefficient and Nusselt number. Figs. 2.1 and 2.2 are sketched for the impacts of nanomaterial volume fraction on both axial and transverse components of velocity. Clearly both velocity and corresponding boundary layer are enhanced against higher nanomaterial volume fraction ϕ. Furthermore the impact of multi-wall CNTs dominants over single-wall CNTs. Effect of porosity parameter λ on axial and transverse components of velocity is displayed via Figs. 2.3 and 2.4. Velocity decreases against higher porosity parameter λ. In fact the permeability of porous medium decreases for larger porosity parameter which leads to reduction of fluid velocity. Effect of single-wall CNTs is more than multi-wall CNTs. Figs. 2.5 and 2.6 show outcome of melting parameter M on axial and transverse components of velocity. Here velocity profiles increases for larger melting parameter M in cases of both single and multi-wall CNTs. Influence of nanomaterial volume fraction ϕ on temperature is presented in Fig. 2.7. Clearly fluid temperature reduces while corresponding thermal layer increases for higher nanomaterial volume fraction ϕ. Fig. 2.8 shows influence of porosity parameter λ on temperature. It is examined that for higher permeability parameter the fluid temperature decreases. In Fig. 2.9 analysis of melting parameter M on temperature is sketched. Temperature reduces for higher M. In fact enlargement in M corresponds to convective flow of heated fluid to the melting surface. Influence of porosity parameter λ on concentration is depicted in Fig. 2.10. Concentration decreases for λ. Fig. 2.11 shows the effect of strength of homogenous reaction parameter K^{*} on concentration. There is decrease in concentration for larger K^{*} while opposite behavior is inspected for boundary layer. Also the impact of single-wall CNTs dominants over multi-wall CNTs. Effect of strength of heterogenous reaction parameter K^{**} on concentration is shown in Fig. 2.12. The result for K^{**} on concentration and associated boundary layer are similar to of K^{*}. Fig. 13. is depicted for the impact of Sc on concentration. It is inspected that concentration enhances while the corresponding solutal boundary layer decreases for larger Sc. The ratio of momentum diffusivity to mass diffusivity is called Schmidt number. Thus by increasing Schmidt number, mass diffusion decreases which is responsible for an enhancement of concentration. Table. 2.1 illustrates specific heat, density and thermal conductivity of carbon nanotubes and water. Table. 2.2 is constructed for numerical data of skin friction coefficient and Nusselt number. The skin friction coefficient is more for larger nanomaterial volume friction ϕ. However it decreases for melting parameter M and porosity parameter λ in both cases of SWCNTs and MWCNTs. Effects of SWCNTs dominant over MWCNTs. Nusselt number shows increasing behavior for larger nanomaterial volume fraction while it has opposite behavior for melting M and porosity λ parameters. Effect of SWCNTs on Nusselt number is more when compared with MWCNTs.

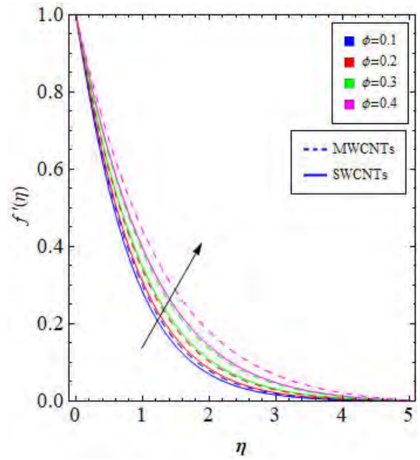

Fig. 2.1: $f'(\eta)$ for higher ϕ.

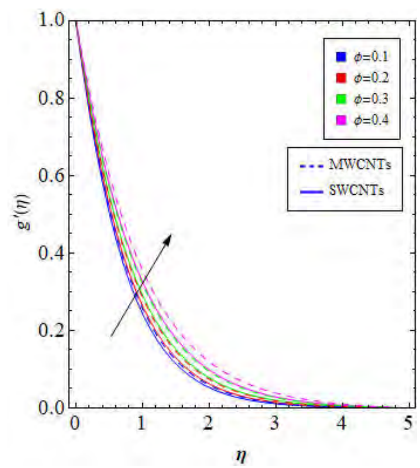

Fig. 2.2: $g'(\eta)$ for higher ϕ.

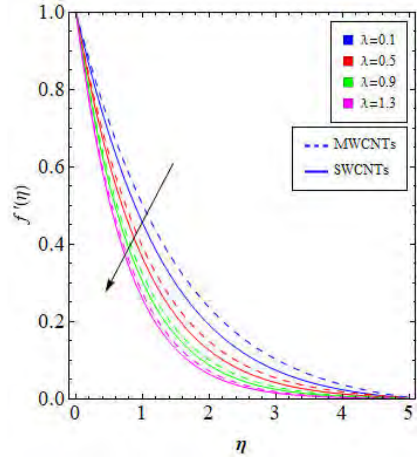

Fig. 2.3: $f'(\eta)$ for higher λ.

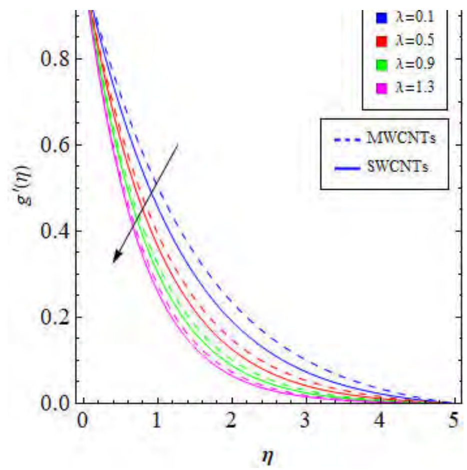

Fig. 2.4: $g'(\eta)$ for higher λ.

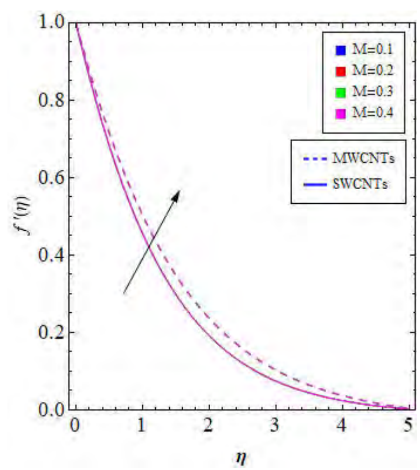

Fig. 2.5: $f'(\eta)$ for higher M.

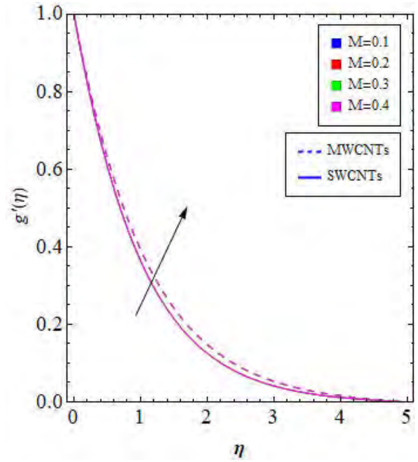

Fig. 2.6: $g'(\eta)$ for higher M.

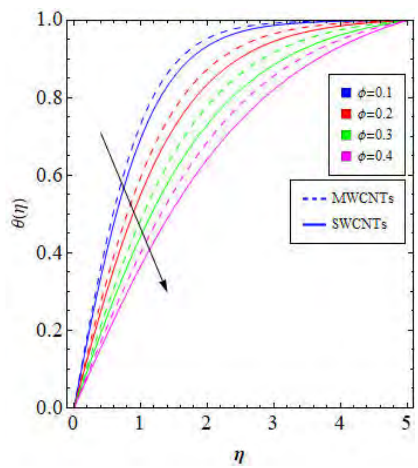

Fig. 2.7: $\theta(\eta)$ for higher ϕ.

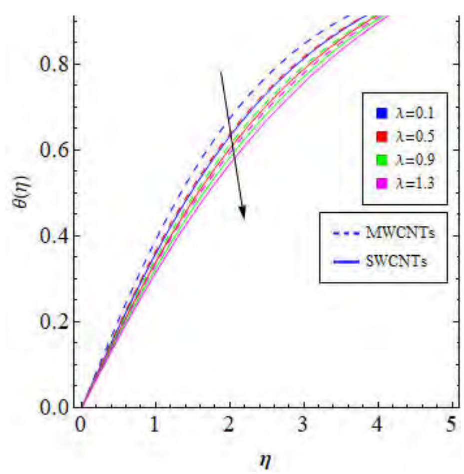

Fig. 2.8: $\theta(\eta)$ for higher λ.

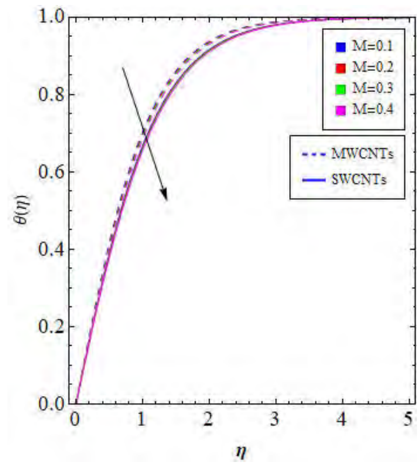

Fig. 2.9: $\theta(\eta)$ for higher M.

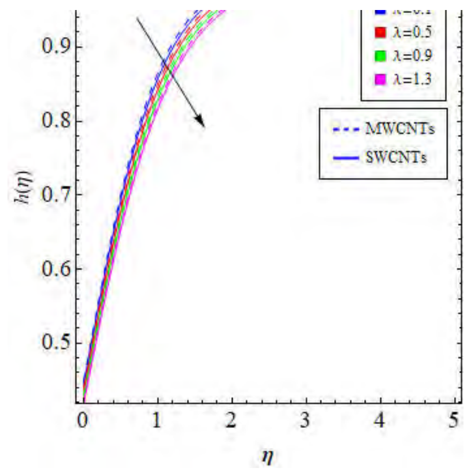

Fig. 2.10: $h(\eta)$ for higher λ.

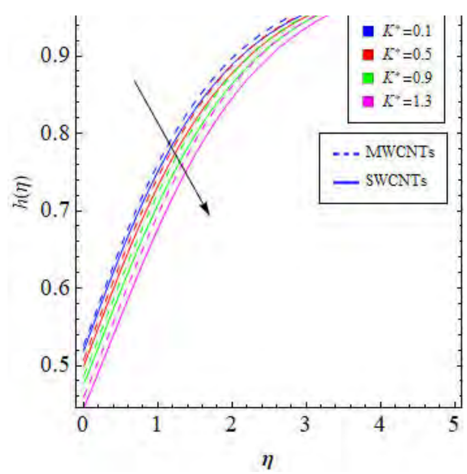

Fig. 2.11: $h(\eta)$ for higher K^*.

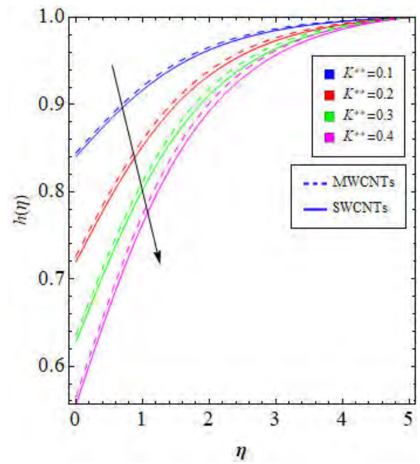

Fig. 2.12: $h(\eta)$ for higher K^{**}.

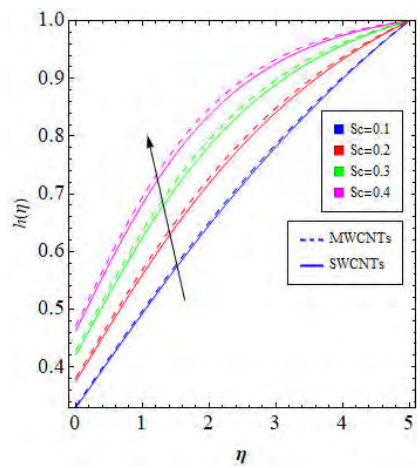

Fig. 2.13: $h(\eta)$ for higher Sc.

2.4 Finalized remarks

The outcomes here are listed as follows.

- Velocity distributions (axial and transverse components of velocity) show increasing behavior for larger nanomaterial volume fraction ϕ. However such velocities have opposite behavior for porosity parameter λ and melting parameter M. Impact of multi-wall CNTs dominants over single-wall CNTs.

- Temperature is smaller for larger nanomaterial volume fraction ϕ, melting parameter M and porosity parameter λ. Furthermore single-wall CNTs are more efficient than multi-wall CNTs.

- Larger strength of homogenous reaction parameter K^* and strength of heterogenous reaction parameter K^{**} cause reduction of concentration. However it enhances for higher Schmidt number Sc.

- Larger nanomaterial volume fraction ϕ cause enlargement in the coefficient of skin friction for both single and multi-wall CNTs cases. Skin friction coefficient reduces for higher melting M and porosity λ parameters.

- Heat transfer rate or cooling process can be increased by utilizing smaller porosity parameter λ and melting parameter M. However it reduces for larger nanomaterial volume fraction ϕ. It is seen that SWCNTs case is more effective than MWCNTs.

Chapter 3

Melting and radiative effects in chemically reactive flow of CNTs

3.1 Introduction

In this chapter we have examined melting heat and thermal radiation in stagnation flow of CNTs (SWCNTs, MWCNTs). Flow is initialized by stretching sheet. Chemical reactions (homogeneous and heterogeneous) are taken into account. Gasoline oil and water are taken as baseliquids. Further conversion of involved PDEs (mass, momentum, energy and concentration) into ODEs is performed through suitable transformations. The obtained ODEs are solved through OHAM. Velocity, temperature, skin friction coefficient, concentration and Nusselt number under involved variables are analyzed.

3.2 Mathematical modeling

We inspect the steady 2D stagnation-point flow towards nonlinear stretchable surface with chemical reactions. Heat transfer in studied via melting heat and thermal radiation. Concept of carbon nanotubes is employed. Sheet thickness is considered by $y = B^* \left(x + b^*\right)^{\frac{1-m}{2}}$, which varies with the distance from the slot due to acceleration/deceleration. CNTs (single-wall CNTs and multi-wall CNTs) are utilized in water and gasoline oil. Cartesian coordinates are chosen in the problem formulation. The homogeneous reaction for cubic autocatalysis is gives by

$$A + 2B \rightarrow 3B, \quad \text{rate} = k_1 a b^2, \tag{3.1}$$

while isothermal reaction of order first on the catalyst surface is

$$A \rightarrow B, \quad \text{rate} = k_s a. \tag{3.2}$$

These expressions of reactions guarantee that the rate of reaction is zero in external flow as well on the outer edge of boundary layer. After utilizing boundary layer approximations, we have the following systems:

$$\frac{\partial u}{\partial x} + \frac{\partial v}{\partial y} = 0, \tag{3.3}$$

$$u\frac{\partial u}{\partial x} + v\frac{\partial u}{\partial y} = U_e \frac{dU_e}{dx} + \nu_{nf} \frac{\partial^2 u}{\partial y^2}, \tag{3.4}$$

$$u\frac{\partial T}{\partial x} + v\frac{\partial T}{\partial y} = \alpha_{nf} \frac{\partial^2 T}{\partial y^2} + \frac{16}{3}\frac{\sigma^*}{k^*}\frac{T_\infty^3}{(\rho c_p)_{nf}}\frac{\partial^2 T}{\partial y^2}, \tag{3.5}$$

$$u\frac{\partial a}{\partial x} + v\frac{\partial a}{\partial y} = D_A \frac{\partial^2 a}{\partial y^2} - k_1 a b^2, \tag{3.6}$$

$$u\frac{\partial b}{\partial x} + v\frac{\partial b}{\partial y} = D_B \frac{\partial^2 b}{\partial y^2} + k_1 a b^2, \tag{3.7}$$

$$\begin{gathered}
u = U_w(x) = U_0 (x + b^*)^m, \quad v = 0, \quad T = T_m, \quad D_A(\frac{\partial a}{\partial y}) = k_s a, \\
D_B(\frac{\partial b}{\partial y}) = -k_s a \quad \text{at} \quad y = B^* (x + b^*)^{\frac{1-m}{2}} \\
u \rightarrow U_e(x) = U_\infty (x + b^*)^m, \quad T \rightarrow T_\infty, \\
a \rightarrow a_0, \quad b \rightarrow 0 \quad \text{as} \quad y \rightarrow \infty.
\end{gathered} \tag{3.8}$$

The shape of the surface is highly dependent upon m. For $m = 1$, the surface becomes flat while for $m < 1$ thickness of surface enhances due to which the surface became outer convex. For $m > 1$ the thickness of wall reduces which is responsible for inner concave like shape of surface. The condition of melting heat transfer is

$$k_{nf}(\frac{\partial T}{\partial y})_{y=B^*(x+b^*)^{\frac{1-m}{2}}} = \rho_{nf} \left[\lambda_1 + c_s(T_m - T_0)\right] v_{y=B^*(x+b^*)^{\frac{1-m}{2}}}. \tag{3.9}$$

Xue elaborated that earlier nanofluid models only valid for rotational or spherical elliptical materials with very small axial ratio. On the basis of thermal conductivity space distribution, the properties of carbon nanotubes cannot be described by these models. To overcome this void, a theoretical model by Maxwell theory for elliptically rotational nanotubes having larger axial ratio and balancing the impacts of space distribution on carbon nanotubes is given by

$$\mu_{nf} = \frac{\mu_f}{(1-\phi)^{2.5}}, \quad \nu_{nf} = \frac{\mu_{nf}}{\rho_{nf}}, \quad \rho_{nf} = (1-\phi)\,\rho_f + \phi\rho_{_{CNTs}},$$

$$\alpha_{nf} = \frac{k_{nf}}{\rho_{nf}\,(c_p)_{nf}}, \quad \frac{k_{nf}}{k_f} = \frac{(1-\phi) + 2\phi\frac{k_{CNTs}}{k_{CNTs}-k_f}\ln\frac{k_{CNTs}+k_f}{2k_f}}{(1-\phi) + 2\phi\frac{kf}{k_{CNTs}-k_f}\ln\frac{k_{CNTs}+k_f}{2k_f}}. \tag{3.10}$$

Table. 3.1: Thermal characteristics for basefluids (water, gasoline oil) [58]:

Physical properties	Basefluids		Nanoparticles	
	Water	Gasoline oil	SWCNTs	MWCNTs
$\rho(\frac{kg}{m^3})$	997	750	2600	1600
$k(\frac{W}{mK})$	0.613	1.5	6600	3000
$c_p(\frac{J}{kgK})$	4179	2100	425	796

Transformations are taken as follows:

$$\zeta = y\sqrt{\frac{m+1}{2}\frac{U_0\,(x+b^*)^{m-1}}{\nu_f}}, \quad \psi = \sqrt{\frac{2}{m+1}\nu_f U_0\,(x+b^*)^{m+1}}F\,(\zeta)\,,$$

$$\Theta\,(\zeta) = \frac{T-T_m}{T_\infty - T_m}, \quad u = U_0\,(x+b^*)^m\,F'\,(\zeta)\,, \tag{3.11}$$

$$v = -\sqrt{\frac{m+1}{2}\nu_f U_0\,(x+b^*)^{m-1}}\left[F\,(\zeta) + \zeta F'\,(\zeta)\,\frac{m-1}{m+1}\right], \quad G(\zeta) = \frac{a}{a_0}, \quad H(\zeta) = \frac{b}{a_0}.$$

Continuity equations (3.3) is trivially satisfied while other equations yield

$$A^* F''' + FF'' - \frac{2m}{m+1}\left(F'\right)^2 + \frac{2m}{m+1}A^2 = 0, \tag{3.12}$$

$$A^{**}(1+\frac{4}{3}\frac{R^*}{\frac{k_{nf}}{k_f}})\Theta'' + \Pr F\Theta' = 0, \tag{3.13}$$

$$\frac{1}{Sc}G'' - \frac{2}{m+1}K^{*}GH^{2} + FG' = 0, \tag{3.14}$$

$$\frac{\delta}{Sc}H'' + \frac{2}{m+1}K^{*}GH^{2} + FH' = 0, \tag{3.15}$$

$$F'(\alpha) = 1, \quad \Theta(\alpha) = 0, \quad \frac{k_{nf}}{k_f}M\ \Theta'(\alpha) + \frac{\Pr}{A^{*}(1-\phi)^{2.5}}[F(\alpha) + \frac{m-1}{m+1}\alpha] = 0,$$

$$G'(\alpha) = \sqrt{\frac{2}{m+1}}K^{**}G(\alpha), \quad \delta H'(\alpha) = -\sqrt{\frac{2}{m+1}}K^{**}G(\alpha) \quad \text{at} \quad \alpha = B^{*}\frac{m+1}{2}\frac{U_0}{\nu_f},$$

$$F'(\alpha) \to A, \quad \Theta(\alpha) \to 1, \quad G(\alpha) \to 1, \quad H(\alpha) \to 1 \quad \text{as} \quad \alpha \to \infty. \tag{3.16}$$

Assuming that both D_A and D_B are equal such that $\delta = 1$, we have

$$G(\zeta) + H(\zeta) = 1. \tag{3.17}$$

Eqs. 3.14 and 3.15 yield

$$\frac{1}{Sc}G'' - \frac{2}{m+1}K^{*}G(1-G)^{2} + FG' = 0. \tag{3.18}$$

In above expressions prime depicts differentiation with respect to η, $\alpha = B^{*}\sqrt{\frac{m+1}{2}\frac{U_0}{\nu_f}}$ is wall thickness parameter and $\zeta = \alpha = B^{*}\sqrt{\frac{m+1}{2}\frac{U_0}{\nu_f}}$ indicates the flat surface. We define $F(\zeta) = f(\zeta - \alpha) = f(\eta)$, $\Theta(\zeta) = \theta(\zeta - \alpha) = \theta(\eta)$ and $G(\zeta) = h(\zeta - \alpha) = h(\eta)$. Therefore the Eqs. $3.12 - 3.18$ become

$$A^{*}f''' + ff'' - \frac{2m}{m+1}\left(f'\right)^{2} + \frac{2m}{m+1}A^{2} = 0, \tag{3.19}$$

$$A^{**}(1 + \frac{4}{3}\frac{R^{*}}{\frac{k_{nf}}{k_f}})\theta'' + \Pr f\theta' = 0, \tag{3.20}$$

$$\frac{1}{Sc}h'' - \frac{2K^{*}}{m+1}h(1-h)^{2} + fh' = 0, \tag{3.21}$$

$$f'(0) = 1, \quad \theta(0) = 0, \quad \frac{k_{nf}}{k_f}M\ \theta'(0) + \frac{\Pr}{A^{*}(1-\phi)^{2.5}}[f(0) + \frac{m-1}{m+1}\alpha] = 0,$$

$$h'(0) = \sqrt{\frac{2}{m+1}}K^{**}h(0), f'(\zeta) \to A, \quad \theta \to 1, \quad h \to 1 \quad \text{as} \quad \eta \to \infty. \tag{3.22}$$

In aforementioned expressions

$$A^* = \frac{1}{(1-\phi)^{2.5}\left(1-\phi+\phi\frac{\rho_{CNTs}}{\rho_f}\right)}, \tag{3.23}$$

$$A^{**} = \frac{\frac{k_{nf}}{k_f}}{1-\phi+\phi\frac{(\rho c_p)_{CNTs}}{(\rho c_p)_f}}. \tag{3.24}$$

Involved parameters are

$$M = \frac{c_p(T_\infty - T_m)}{\lambda_1 + c_s\left(T_m - T_0\right)}, \qquad \Pr = \frac{\mu_f(c_p)_f}{k_f}, \qquad A = \frac{U_\infty}{U_0},$$

$$\delta = \frac{D_B}{D_A}, \qquad K^* = \frac{a_0^2 k_1(b^*+x)}{U_{w(x)}}, \qquad R^* = \frac{4\sigma^*}{k^* k_f}T_\infty^3, \qquad K^{**} = \frac{k_s}{D_A}\sqrt{\frac{(b^*+x)v_f}{U_{w(x)}}}. \tag{3.25}$$

Skin friction and local Nusselt number are

$$C_{fx} = \frac{\tau_w}{\rho_f U_w^2}, \qquad Nu_x = \frac{\left(x+b^*\right)q_w}{k_f(T_\infty - T_m)}, \tag{3.26}$$

with

$$\tau_{wx} = \mu_{nf}\left(\frac{\partial u}{\partial y}\right)_{y=B^*(x+b^*)^{\frac{1-m}{2}}}, \qquad q_w = -\kappa_{nf}\left(\frac{\partial T}{\partial y}\right)_{y=B^*(x+b^*)^{\frac{1-m}{2}}}. \tag{3.27}$$

Dimensionless skin friction coefficient and local Nusselt number are

$$C_{fx}\sqrt{\mathrm{Re}} = \frac{1}{(1-\phi)^{2.5}}\sqrt{\frac{m+1}{2}}f''(0), \qquad \frac{Nu_x}{\sqrt{\mathrm{Re}}} = -\frac{k_{nf}}{k_f}\sqrt{\frac{m+1}{2}}\theta'(0). \tag{3.28}$$

Here Reynolds number is defined by $\mathrm{Re} = \frac{U_w(x+b^*)}{\nu_f}$.

3.3 Convergence analysis

Optimal values for convergence control parameters are obtained via OHAM. The optimal values for parameters in single-wall CNTs-water are $\hbar_f$=-0.35450, $\hbar_\theta$=-0.10309, $\hbar_h$=-0.30656 and gasoline are $\hbar_f$=-0.96961, $\hbar_\theta$=-0.09919, $\hbar_h$=-0.31119 while for multi-wall CNTs-water $\hbar_f$=-0.35083, $\hbar_\theta$=-0.10785, $\hbar_h$=-0.30478 and gasoline are $\hbar_f$=-0.68257, $\hbar_\theta$=-0.10164, $\hbar_h$=-0.30969.

In Figs.(3.1)-(3.4), total residual error verses order of approximations is presented for both single and multi-wall CNTs considering water and gasoline as baseliquids.

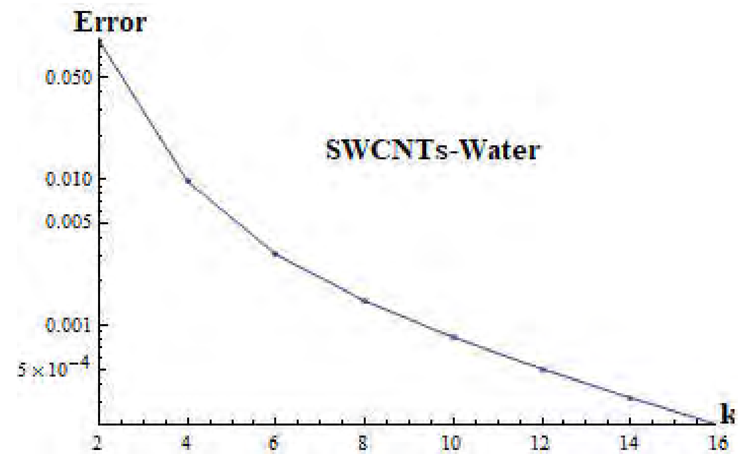

Fig. 3.1: Error with various iterations during SWCNTs-Water.

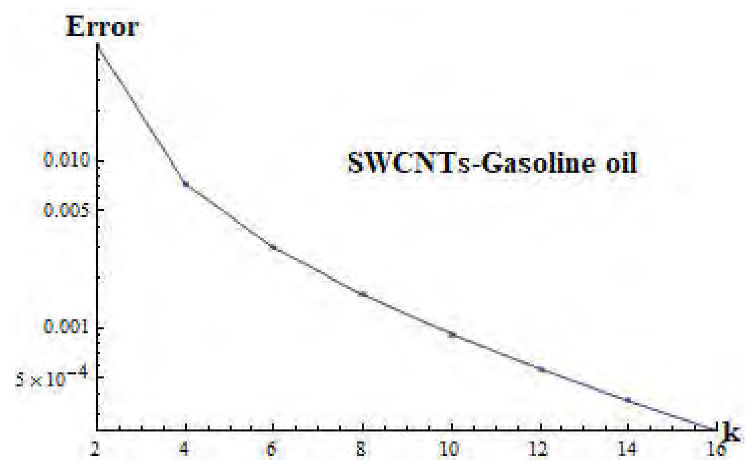

Fig. 3.2: Error with various iterations during SWCNTs-Gasoline oil.

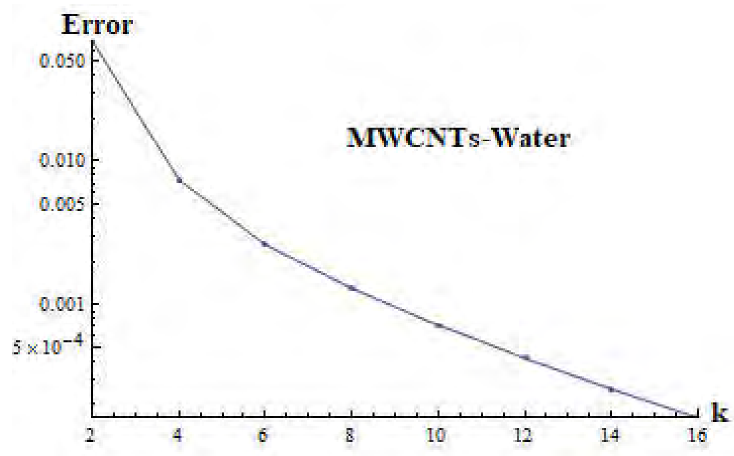

Fig. 3.3: Error with various iterations during MWCNTs-Water.

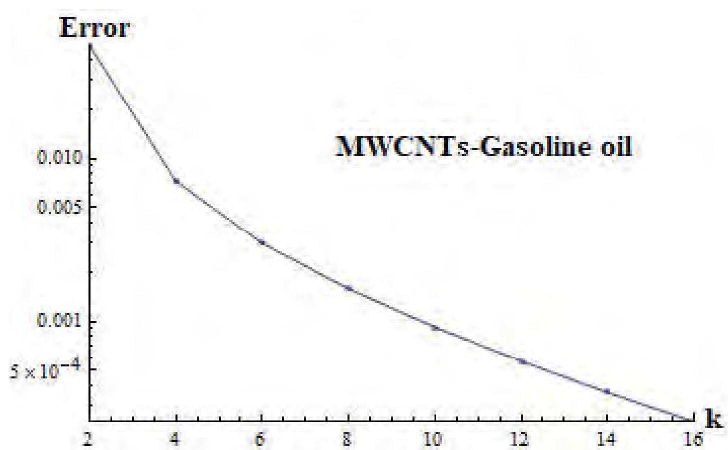

Fig. 3.4: Error with various iterations during MWCNTs-Gasoline oil.

Table. 3.2: Individual average square residual error using optimal data of auxiliary variables.

Iterations	SWCNTs			MWCNTs		
k	ε_k^f	ε_k^θ	ε_k^h	ε_k^f	ε_k^θ	ε_k^h
2 (Water)	7.8×10^{-6}	6.3×10^{-3}	2.5×10^{-3}	1.8×10^{-5}	4.4×10^{-3}	2.4×10^{-3}
Gasoline	5.6×10^{-5}	2.2×10^{-3}	2.5×10^{-3}	5.2×10^{-5}	1.5×10^{-3}	2.4×10^{-3}
4 (Water)	2.7×10^{-7}	3.1×10^{-3}	6.4×10^{-4}	6.8×10^{-7}	1.3×10^{-4}	6.0×10^{-4}
Gasoline	4.4×10^{-6}	3.6×10^{-5}	6.8×10^{-4}	9.8×10^{-6}	1.1×10^{-4}	3.0×10^{-4}
8 (Water)	3.4×10^{-7}	2.9×10^{-5}	2.7×10^{-4}	2.8×10^{-8}	4.3×10^{-6}	1.2×10^{-4}
Gasoline	1.2×10^{-7}	3.2×10^{-6}	1.5×10^{-4}	3.3×10^{-9}	4.0×10^{-6}	1.3×10^{-4}
12 (Water)	1.0×10^{-7}	3.0×10^{-6}	1.4×10^{-4}	1.0×10^{-9}	3.3×10^{-6}	4.1×10^{-5}
Gasoline	1.5×10^{-10}	4.3×10^{-8}	5.6×10^{-5}	5.9×10^{-11}	4.8×10^{-6}	4.6×10^{-5}
16 (Water)	6.7×10^{-11}	6.7×10^{-9}	2.0×10^{-5}	1.6×10^{-11}	1.9×10^{-7}	1.6×10^{-5}
Gasoline	2.4×10^{-13}	1.6×10^{-9}	2.4×10^{-6}	3.2×10^{-12}	8.9×10^{-7}	1.8×10^{-5}

3.4 Analysis

In this section velocity, temperature, skin fraction coefficient and Nusselt number are discussed under the influential variables for two cases i.e., single and multi-wall CNTs in the presence of water and gasoline oil. Figs. 3.5-3.9 are visualized for the behavior of velocity towards ϕ, M, m, A and α. It is inspected that velocity of fluid shows rapid growth for higher ϕ, M, $A, m \geq 1$and α whereas reverse impact is seen for larger $m \leq 1$. For velocity field, the impact of multi-wall CNTs dominates over single-wall CNTs through larger ϕ and m^* in case of both water and gasoline basefluids. Similarly for larger M, A and α, the influence of single-wall CNTs dominants over multi-wall CNTs in velocity field. It is due to the fact that for higher M rapid moment of heated fluids towards melting surface occurs due to which velocity enhances. It is also found that velocity is higher for larger A in both cases $A > 1$ and $A < 1$. Furthermore boundary layer has opposite trend for $A > 1$ and $A < 1$ but there in no development of boundary layer for $A = 1$ in case of both water and gasoline basefluids. Temperature under the impact of M, A and $R^*$is composed in Figs. 3.10-3.12. Temperature of fluid declines for higher M, A and R^*. Impact of single-wall CNTs dominants over multi-wall CNTs. For higher M, flow of heated fluids towards cooled surface increases, and thus velocity of fluid enhances and is responsible for decline of temperature of fluid. Moreover thermal boundary layer enhances for higher M. For higher A the temperature of fluid decays. It is because larger A is responsible for higher pressure and resistance to the flow reduces. Hence temperature of fluid enhances. Effects of K^*, K^{**} and Sc on concentration are marked in Figs. 3.13-3.15. It is found that there is intensification in the concentration for higher K^{**} and Sc while opposite behavior is inspected for larger K^*. Also solutal boundary layer enhances for larger K^*. It is examined that influence of multi-wall CNTs is more efficient than that of single-wall CNTs in both water and gasoline baseliquids. The ratio of momentum diffusivity to mass diffusivity is called Schmidt number. Thus due to increment in Sc mass diffusivity reduces which causes decline in concentration. Skin fraction coefficient under the impact of A, ϕ, M and m is traced in Figs. 3.16 and 3.17. Here skin fraction coefficient rises for higher M and A while it reduces for ϕ and m. Impacts of ϕ, M and R^*on Nusselt number are depicted in Figs. 3.18-3.19. Rate of heat transfer is higher for larger values of the mention parameters. Impact of single-wall CNTs dominates over multi-wall CNTs by considering parameters ϕ and M while considering ϕ and R^* the impact of multi-wall CNTs is efficient in terms of heat transfer. Density, specific heat and thermal conductivity of baseliquids (water and gasoline oil) and nanomaterials are given in Table 3.1 while at different order of approximations, average square residual error is labeled in Table 3.2.

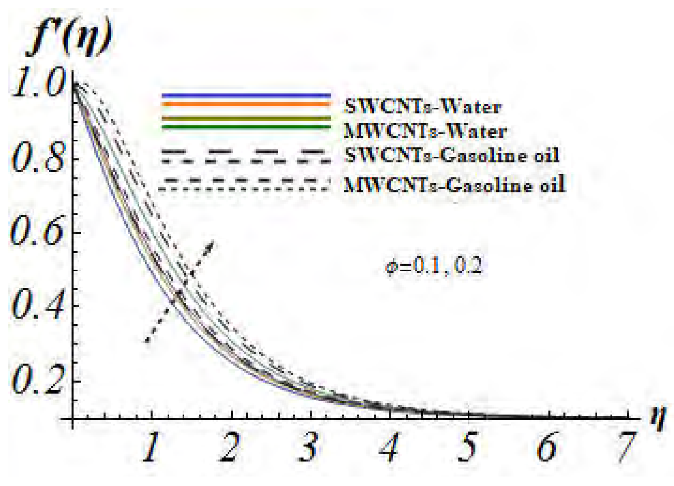

Fig. 3.5: $f'(\eta)$ for higher ϕ.

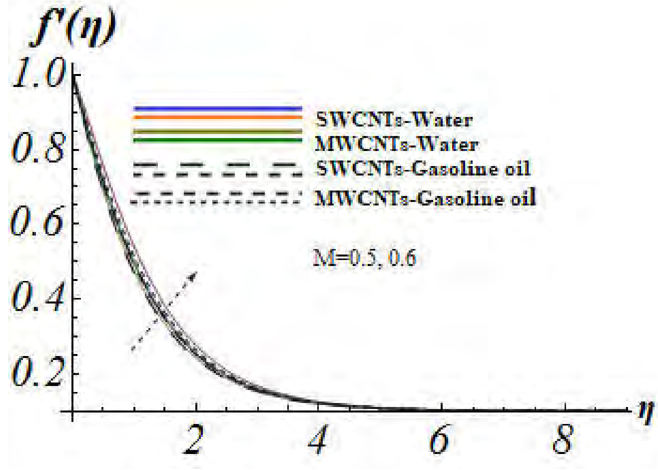

Fig. 3.6: $f'(\eta)$ for higher M.

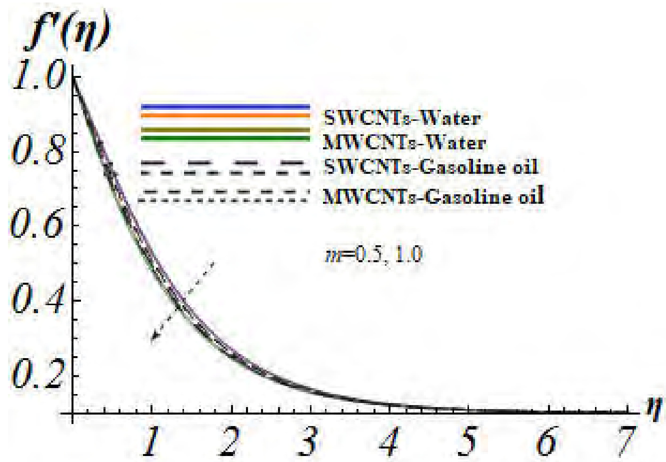

Fig. 3.7: $f'(\eta)$ for higher m.

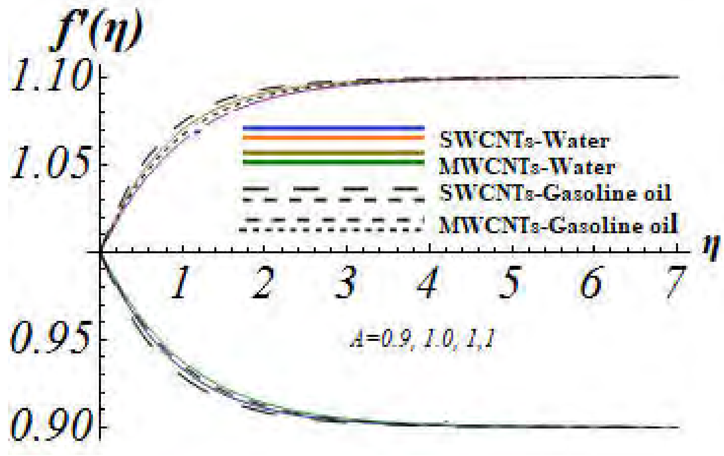

Fig. 3.8: $f'(\eta)$ for higher A.

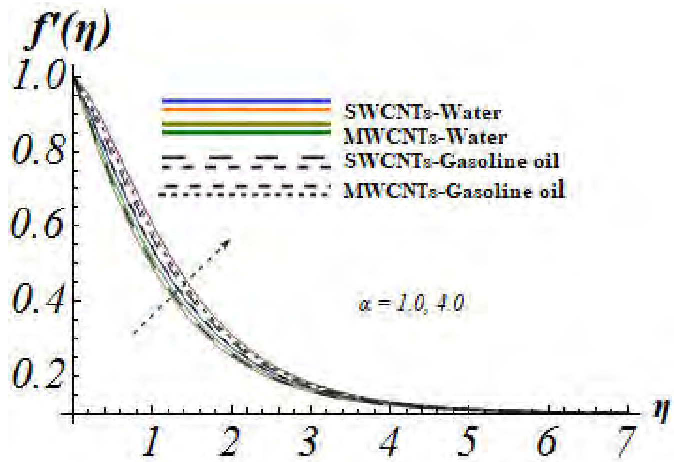

Fig. 3.9: $f'(\eta)$ for higher α.

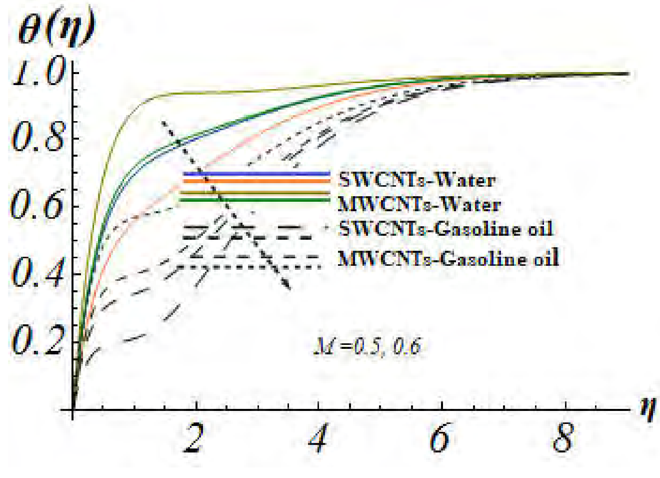

Fig. 3.10: $\theta(\eta)$ for higher M.

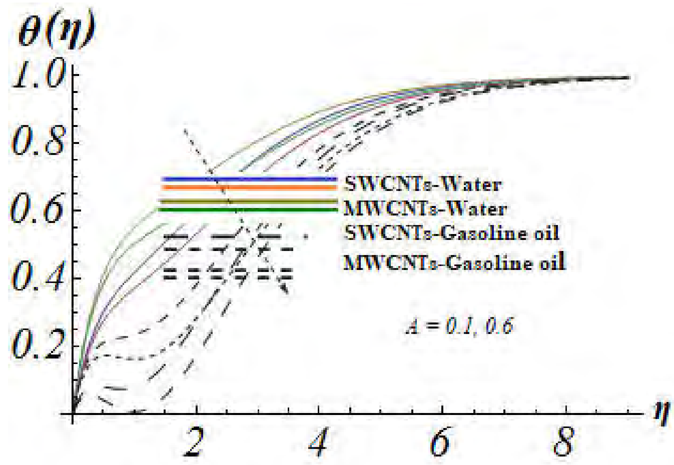

Fig. 3.11: $\theta(\eta)$ for higher A.

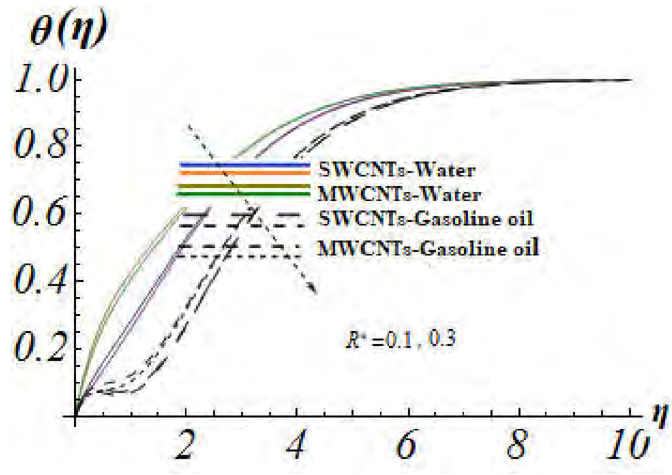

Fig. 3.12: $\theta(\eta)$ for higher R^*.

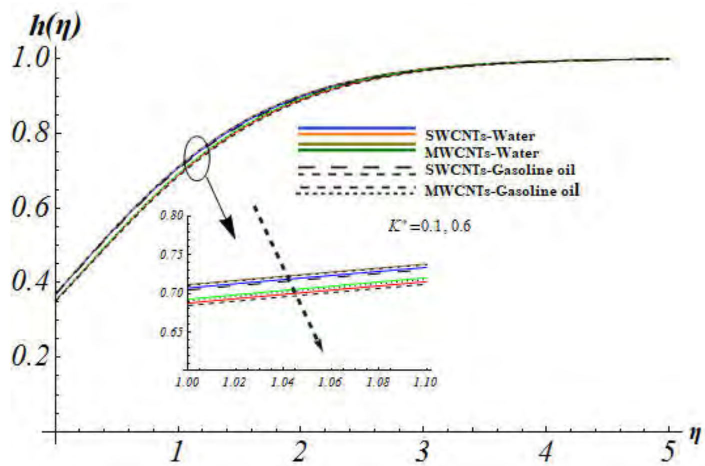

Fig. 3.13: $h(\eta)$ for higher K^*.

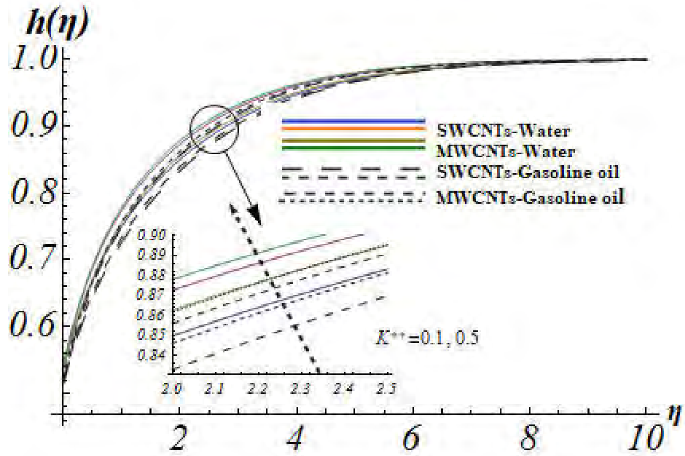

Fig. 3.14: $h(\eta)$ for higher K^{**}.

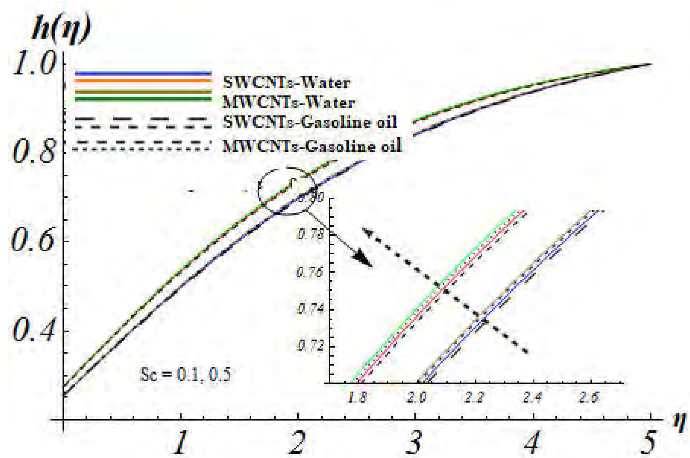

Fig. 3.15: $h(\eta)$ for higher Sc.

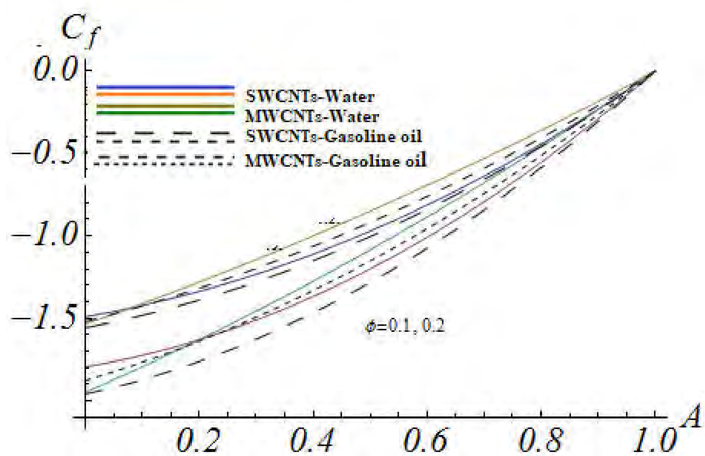

Fig. 3.16: C_f for higher A and ϕ.

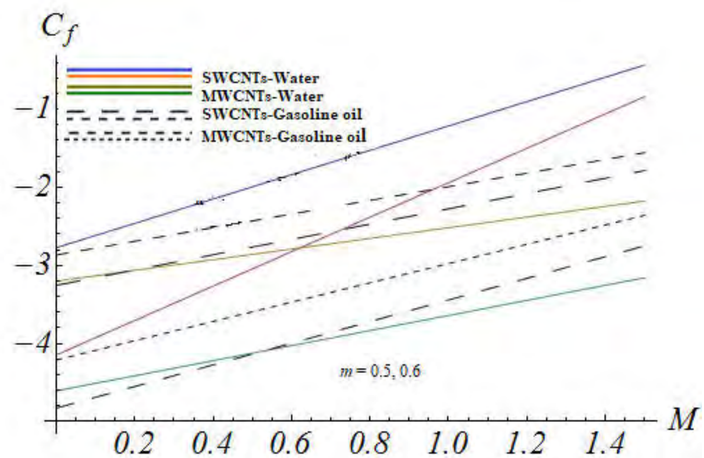

Fig. 3.17: C_f for higher M and m.

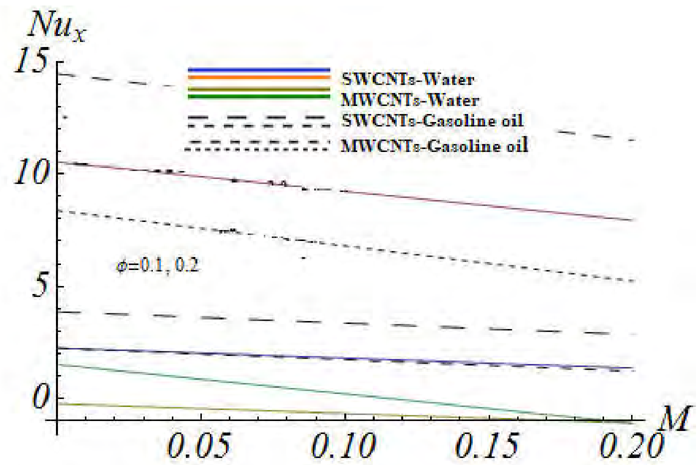

Fig. 3.18: Nu_x for higher M and ϕ.

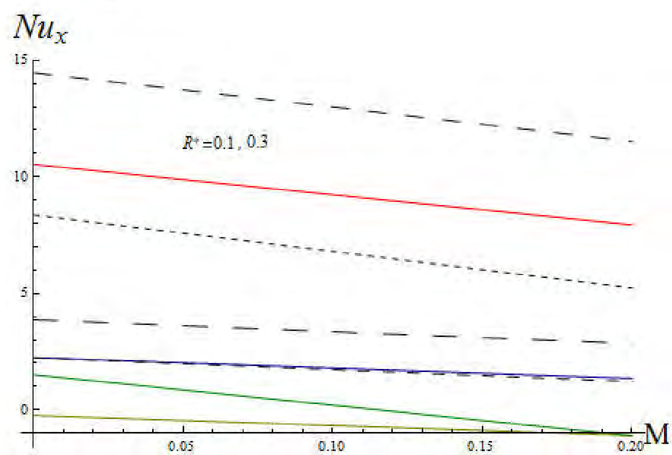

Fig. 3.19: Nu_x for higher M and R^*.

Table. 3.3: Numerical comparison of skin friction coefficient for the present work verses previous published work when $m = 1$, $\phi = 0$ at different values of A.

A	Mahapatra and Gupta	Sharma and Singh	Pop et al.	Present obtained results
0.1	-0.9694	-0.969386	-0.9694	-0.969261
0.2	-0.9181	-0.9181069	-0.9181	-0.91851
0.5	-0.6673	-0.667263	-0.6673	-0.66235
0.7				-0.43257
0.8				-0.29971
0.9				-0.15321
1.0				0.00000

3.5 Finalized Remarks

In the present work we have discussed melting heat transfer and thermal radiation effects in stagnation-point flow of CNTs towards a variable thickness surface. The outcomes are listed as follows:

- Velocity enhances for larger M and α. Also impact of single-wall CNTs is efficient than that of multi-wall CNTs in both water and gasoline baseliquids cases.
- For higher values of ϕ, velocity of fluid shows rapid growth while for increment in m there is opposite trend. Impact of multi-wall CNTs is greater than single wall CNTs.
- Temperature profile decreases with an increment in M, A and R^*. Single-wall CNTs show greater impact than multi-wall CNTs in both water and gasoline cases.
- Concentration profile shows an enlargement with an increase in Sc and K^{**} while reduction is inspected for higher K^*.
- For higher values of ϕ and m, a reduction in skin friction coefficient for both single-wall CNTs and multi-wall CNTs in water and gasoline is inspected while opposite behavior is studied for larger A and M.
- Local Nusselt number is increased by utilizing larger values of ϕ and R^*. Influence of multi-wall CNTs is more efficient when compared with single-wall CNTs.

Chapter 4

Entropy production and melting heat in squeezing flow of CNTs

4.1 Introduction

This chapter deals with optimization of entropy production in squeezing flow of CNTs (SWCNTs, MWCNTs). Nanomaterial consists of water as basefluid while CNTs as nanoparticles. Heat transport via melting effect is explored. Transformation technique is implemented for conversion of PDEs (flow and heat transfer expressions) into ODEs. Shooting technique (bvp4c) is employed for solutions development. Bejan number, entropy production rate, velocity and temperature are studied graphically while Nusselt number and skin friction are elaborated numerically under influential variables.

4.2 Mathematical modeling

Unsteady squeezed flow of carbon nanomaterial is assumed between two parallel plates. Both plates are distant $h(t)$ apart. Lower plate (at $y=0$) is stretched with velocity $U_w = \frac{U_0 x}{1-ct}$ while the plate at $y = h(t)$ is set in motion towards the plate at $y = 0$ with a squeezing velocity $v_h = \frac{dh}{dt} = \sqrt{\frac{v_f(1-ct)}{U_0}}$. Melting heat is considered for heat transfer. Entropy generation effect is considered. Flow is parallel to $x-$axis while $y-$axis normal to it. Expressions under interest are

$$\frac{\partial u}{\partial x}+\frac{\partial v}{\partial y}=0, \tag{4.1}$$

$$\rho_{nf}(\frac{\partial u}{\partial t}+u\frac{\partial u}{\partial x}+v\frac{\partial u}{\partial y})=-\frac{\partial p_1}{\partial x}+\mu_{nf}\ (\frac{\partial^2 u}{\partial x^2}+\frac{\partial^2 u}{\partial y^2}), \tag{4.2}$$

$$\rho_{nf}(\frac{\partial v}{\partial t}+u\frac{\partial v}{\partial x}+v\frac{\partial v}{\partial y})=-\frac{\partial p_1}{\partial y}+\mu_{nf}\ (\frac{\partial^2 v}{\partial x^2}+\frac{\partial^2 v}{\partial y^2}), \tag{4.3}$$

$$\frac{\partial T}{\partial t}+u\frac{\partial T}{\partial x}+v\frac{\partial T}{\partial y}=\alpha_{nf}(\frac{\partial^2 T}{\partial x^2}+\frac{\partial^2 T}{\partial y^2})+\frac{\mu_{nf}}{(\rho c_p)_{nf}}[4(\frac{\partial u}{\partial x})^2+(\frac{\partial v}{\partial x}+\frac{\partial u}{\partial y})^2], \tag{4.4}$$

with boundary conditions

$$u=U_w\,(x)=\frac{U_0x}{1-ct},\qquad T=T_m\qquad \text{at}\qquad y=0,$$

$$u=0,\qquad v=v_h=\frac{dh}{dt},\qquad T=T_h\qquad \text{at}\qquad y=h(t). \tag{4.5}$$

Melting condition is

$$k_{nf}(\frac{\partial T}{\partial y})=\rho_{nf}(\lambda_1+c_s(T_m-T_0))v\qquad \text{at}\qquad y=0. \tag{4.6}$$

Xue expression for CNTs are

$$\mu_{nf}=\frac{\mu_f}{(1-\phi)^{2.5}},\qquad \nu_{nf}=\frac{\mu_{nf}}{\rho_{nf}},\qquad \rho_{nf}=(1-\phi)\,\rho_f+\phi\rho_{_{CNTs}},$$

$$\alpha_{nf}=\frac{k_{nf}}{\rho_{nf}\,(c_p)_{nf}},\qquad \frac{k_{nf}}{k_f}=\frac{(1-\phi)+2\phi\frac{k_{CNTs}}{k_{CNTs}-k_f}\ln\frac{k_{CNTs}+k_f}{2k_f}}{(1-\phi)+2\phi\frac{kf}{k_{CNTs}-k_f}\ln\frac{k_{CNTs}+k_f}{2k_f}}. \tag{4.7}$$

Table. 4.1: Thermophysical features of baseliquid (water) and nanoparticles (SWCNTs, MWCNTs) [58].

Physical properties	CNTs		Baseliquid
	SWCNTs	MWCNTs	Water
$c_p(\frac{J}{kgK})$	425	796	4179
$k(\frac{W}{mK})$	6600	3000	0.613
$\rho(\frac{kg}{m^3})$	2600	1600	997

We set the transformations

$$\eta = \frac{y}{h(t)}, \quad u = (\frac{U_0 x}{(1-ct)}) f'(\eta), \quad v = -\sqrt{\frac{U_0 \upsilon_f}{1-ct}} f(\eta), \quad \theta(\eta) = \frac{T - T_m}{T_f - T_m},$$

$$\text{where} \quad h(t) = \sqrt{\frac{\upsilon_f (1-ct)}{a}}. \tag{4.8}$$

After implementing aforementioned transformations, Eq. 4.1 is verified while the other equations take the form

$$A^* f^{(iv)} - f'f'' + ff''' - \frac{Sq}{2}(3f'' + \eta f''') = 0, \tag{4.9}$$

$$A^{**}\theta'' + \Pr(f\theta' - \frac{Sq}{2}\eta\theta') + \frac{A^{**}\Pr}{(1-\phi)^{2.5}}(4Ecf'^2 + Ec_1 f''^2) = 0. \tag{4.10}$$

$$f'(0) = 1, \quad \theta(0) = 0, \quad \frac{k_{nf}}{k_f} M\theta'(0) + \frac{\Pr}{A^*(1-\phi)^{2.5}} f(0) = 0,$$

$$f'(1) = 0, \quad f(1) = 1, \quad \theta(1) = 1. \tag{4.11}$$

In aforementioned expressions we have

$$A^* = \frac{1}{(1-\phi)^{2.5}\left(1-\phi+\phi\frac{\rho_{CNTs}}{\rho_f}\right)}, \tag{4.12}$$

$$A^{**} = \frac{\frac{k_{nf}}{k_f}}{1-\phi+\phi\frac{(\rho c_p)_{CNTs}}{(\rho c_p)_f}}. \tag{4.13}$$

The involved dimensionless parameters are

$$Sq = \frac{c}{U_0}, \quad \Pr = \frac{\mu_f (c_p)_f}{k_f}, \quad Ec = \frac{\nu_f^2}{h^2 (c_p)_f (T_m - T_h)},$$

$$Ec_1 = \frac{U_w^2}{(c_p)_f(T_m - T_h)}, \quad M = \frac{c_p\,(T_\infty - T_m)}{\lambda_1 + c_s\,(T_m - T_0)}, \quad \eta = \frac{y}{h(t)}. \tag{4.14}$$

4.2.1 Expressions of skin friction coefficient ($C_f\sqrt{\mathrm{Re}}$) and Nusselt number ($\frac{Nu_x}{\sqrt{\mathrm{Re}}}$):

Expressions for $C_f\sqrt{\mathrm{Re}}$ and $\frac{Nu_x}{\sqrt{\mathrm{Re}}}$ in dimensional and non-dimensional forms are

$$C_{fx} = \frac{(\tau_{wx})_{y=0}}{\rho_f U_w^2}, \quad Nu_x = \frac{xq_w}{k_f(T_f - T_h)},$$

with

$$\tau_{wx} = \mu_{hnf}(\frac{\partial u}{\partial y})_{y=0}, \quad q_w = -k_{hnf}(\frac{\partial u}{\partial y})_{y=0}.$$

After implementing transformations (4.8) we get

$$C_{fx}\sqrt{\mathrm{Re}_x} = \frac{1}{(1-\phi_1)^{2.5}} f''(0), \quad \frac{Nu_x}{\sqrt{\mathrm{Re}_x}} = -\frac{k_{hnf}}{k_f}\theta'(0), \tag{4.15}$$

where $\mathrm{Re} = \sqrt{\frac{(1-ct)v_f}{U_0}}$ represents local Reynolds number.

4.2.2 Entropy analysis

Entropy generation rate is

$$S_G = S_H(\text{entropy via heat transfer}) + S_F(\text{entropy via fluid friction}), \tag{4.16}$$

or

$$S_G = \frac{k_{nf}}{T_h^2}((\frac{\partial T}{\partial x})^2 + (\frac{\partial T}{\partial y})^2) + \frac{\mu_{nf}}{T_h}(4(\frac{\partial u}{\partial x})^2 + (\frac{\partial v}{\partial x} + \frac{\partial u}{\partial y})^2). \tag{4.17}$$

Non-dimensional entropy generation is

$$Ns = N_H(\text{entropy via heat transfer}) + N_F(\text{entropy via fluid friction}), \tag{4.18}$$

$$Ns = \frac{S_G}{S_{G_0}} = \theta'^2 + \frac{\mathrm{Pr}}{\Omega(k_{nf}/k_f)\,(1-\phi)^{2.5}}(4Ecf'^2 + Ec_1 f''^2) \tag{4.19}$$

$$\text{where} \quad S_{G_0} = \frac{k_{nf}(T_m - T_h)}{T_h^2 h^2}.$$

Bejan number is

$$Be = \frac{N_H(\text{entropy via heat transfer})}{N_G(\text{Total entropy})},$$

or

$$Be = \frac{\theta'^2}{\theta'^2 + \frac{\Pr}{\frac{k_{nf}}{k_f}\Omega(1-\phi)^{2.5}}(4Ecf'^2 + Ec_1 f''^2)}. \tag{4.20}$$

Note that Bejan number (Be) lies between 0 and 1. N_H dominates over N_F when $0.5 < Be \leqslant 1.0$ and N_F overrides N_H for $0 \leqslant Be < 0.5$ while for $Be = 1.0$ both N_H and N_F are equal.

4.3 Solutions via bvp4c method

Governing equations for flow and heat transport are solved via shooting method (bvp4c). This method is implemented through writing first order ODEs. Thus we proceed as below

$$f = s_1, \quad f' = s_2, \tag{4.21}$$

$$f'' = s_3, \quad f''' = s_4, \tag{4.22}$$

$$s_4' = f^{(iv)} = (1-\phi)^{2.5}\left(1 - \phi + \phi\frac{\rho_{CNT}}{\rho_f}\right)\left(\frac{Sq}{2}(\eta s_4 + 3s_3) - s_2 s_3 + s_{1s_4}\right), \tag{4.23}$$

$$\theta = s_5, \quad \theta' = s_6 \tag{4.24}$$

$$s_6' = \frac{1}{A^{**}}\left(-\Pr(s_1 s_6 - \frac{Sq}{2}\eta s_6) - \frac{\Pr}{(1-\phi)^{2.5}}(Ec_1 s_3^2 + 4Ecs_2^2)\right) \tag{4.25}$$

with associated conditions

$$s_2(0) = 1, \quad \frac{k_{nf}}{k_f}Ms_6(0) + \frac{\Pr}{A^*(1-\phi)^{2.5}}s_1(0) = 0, \quad s_5(0) = 0,$$

$$s_3(1) = 1, \quad s_4(1) = 1, \quad s_6'(1) = 0. \tag{4.26}$$

Table. 4.2: Analysis of C_f via Sq, ϕ and M.

Sq	ϕ	M	C_f(SWCNTs)	C_f(MWCNTs)
-1.0	0.5	0.7	82.5	49.3
0.0			82.8	49.4
1.0			83.1	49.5
2.0			83.5	49.6
3.0			83.8	49.8
1.0	0.1	0.7	6.8	6.2
	0.2		7.8	6.3
	0.3		11.8	8.4
	0.4		20.3	13.2
1.0	0.5	0.7	38.6	23.9
1.0	0.1	0.1	3.6	3.7
		0.2	4.9	5.1
		0.3	6.8	7.4
		0.4	11.5	14.8
		0.5	25.7	29.4

Table. 4.3: Analysis of Nu_x via Sq, ϕ and M when $Ec = Ec_1 = 0.2$.

Sq	ϕ	M	Nu_x (SWCNTs)	Nu_x (MWCNTs)
-1.0	0.5	0.7	24.3	9.7
0.0			24.5	9.8
1.0			24.7	9.9
2.0			24.9	10.0
3.0			25.1	10.1
1.0	0.1	0.7	11.4	9.3
	0.2		12.0	9.4
	0.3		14.0	9.5
	0.4		16.5	9.6
	0.5		19.2	9.7
1.0	0.1	0.1	7.0	7.4
		0.2	9.6	10.3
		0.3	12.7	13.9
		0.4	16.7	18.7
1.0	0.1	0.5	21.9	29.9

4.4 Analysis

4.4.1 Analysis for flow and temperature

In this subsection influences of involved parameters on flow and temperature are analyzed graphically. Figs. 4.1-4.3 are plotted in order to study variations of flow under Sq, ϕ and M. Intensification in flow is seen for larger Sq. Variation in flow via Sq can be studied in two cases. i. $Sq > 0$ (motion of the squeezing plate (upper plate) towards stretchable plate (lower plate)), ii. (motion of the squeezing plate (upper plate) away from stretchable plate (lower plate)). For higher Sq ($Sq > 0$) the velocity of fluid rises due to influence of a force (squeezing force) felt by fluid particles. Also increments in ϕ and M lead to an enhancement in flow. Physically increment in M is associated with more rapid flow of heated fluid towards melting surface which intensifies flow. Interestingly single-walled CNTs shows overriding trends when compared with multiple-walled CNTs. Variations in temperature via Sq, ϕ and M are labeled in Figs. 4.4-4.6.

Reduction in temperature is observed for an increment in Sq ($Sq > 0$). Higher Sq lead to small collision among the fluid particles. Hence temperature decays while the associated penetration depth rises. Decay in temperature is noted with variations in ϕ and M while opposite trend is seen for associated penetration depth. Physically higher M leads to more flow from hot fluid towards the melting surface. Hence fluid temperature decays. Furthermore overriding impact is observed for single-walled CNTs.

4.4.2 Analysis for entropy generation and Bejan number

Variations in Ns and Be via Sq, ϕ and M are depicted in this subsection. Figs. 4.7, 4.9 and 4.11 illustrate variations in Ns via Sq, ϕ and M respectively. It is noticed that Ns reduces with an increment in Sq. Furthermore production of entropy is maximum at the both walls while it is minimum at the centre of channel. Higher ϕ leads to smaller Ns while Ns intensifies for larger M. At both walls production of entropy in maximum while at centre the entropy production is minimum. Further single-walled CNTs show overriding trend comparatively with multiple-walled CNTs. In order to analyze the dominance of entropy due to fluid friction over entropy due to heat transfer or vise versa, Be is labeled via η in Figs. 4.8, 4.10 and 4.12. Intensification in Be is noted with an increment in Sq. It is observed that at the lower wall the entropy due to fluid friction is prominent for higher Sq. Reduction in Be is noted for higher ϕ. It is also observed that entropy via fluid friction shows overriding behavior at both walls. Be decays with an increment in M and dominance in entropy via fluid friction is noticed at both walls over entropy via heat transfer. Furthermore single-walled CNTs shows prominent behavior. Tables 4.1 is constructed for thermophysical features of nanoparticles (CNTs) and baseliquid (water) while numerical values of C_f and Nu_x under Sq, ϕ and M are presented in Tables. 4.2 and 4.3.

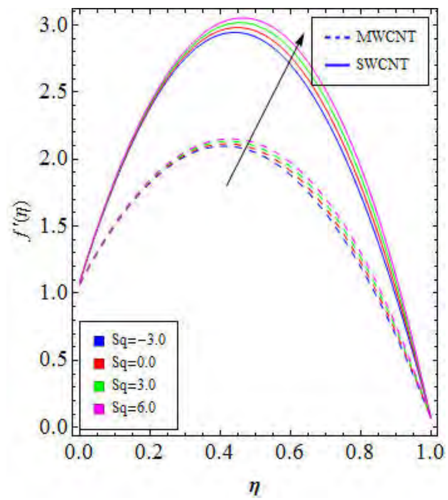

Fig. 4.1: $f'(\eta)$ for higher Sq.

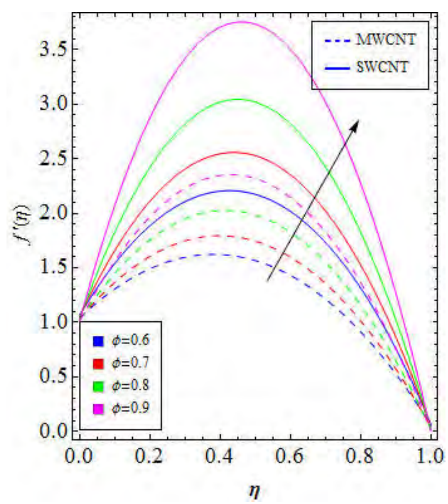

Fig. 4.2: $f'(\eta)$ for higher ϕ.

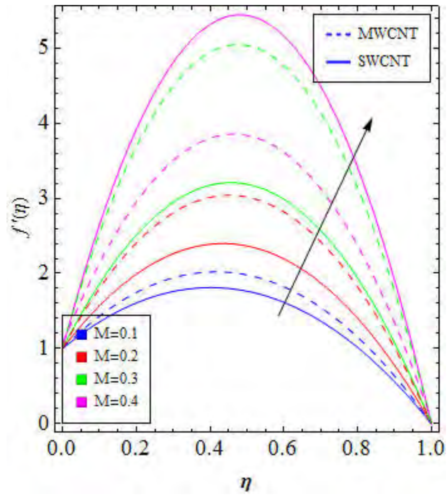

Fig. 4.3: $f'(\eta)$ for higher M.

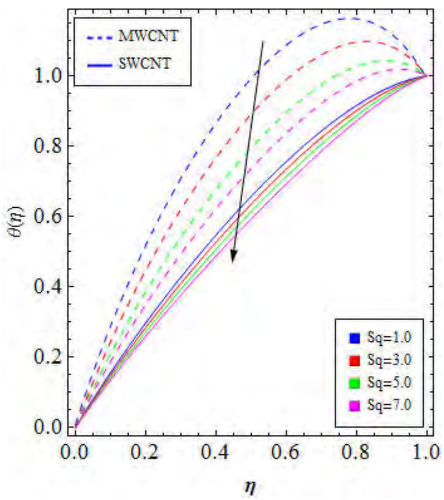

Fig. 4.4: $\theta(\eta)$ for higher Sq.

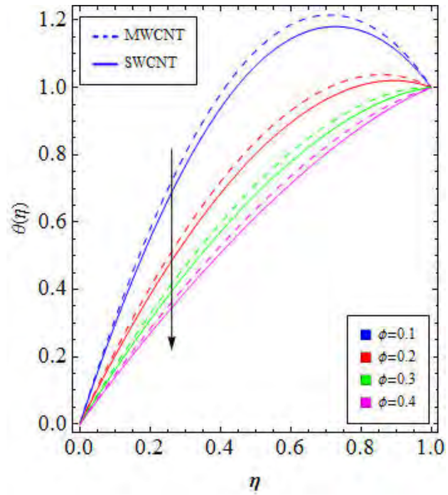

Fig. 4.5: $\theta(\eta)$ for higher ϕ.

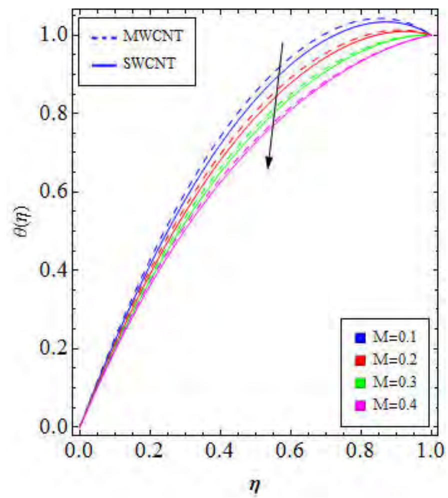

Fig. 4.6: $\theta(\eta)$ for higher M.

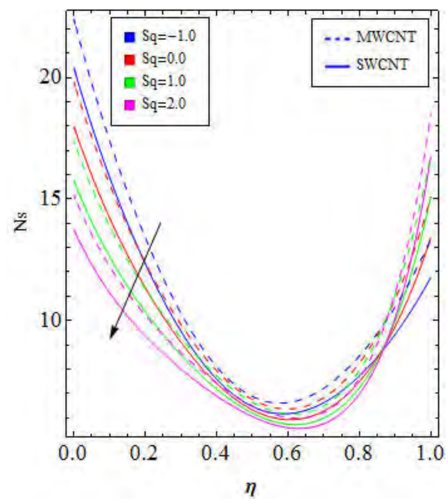

Fig. 4.7: Ns for higher Sq.

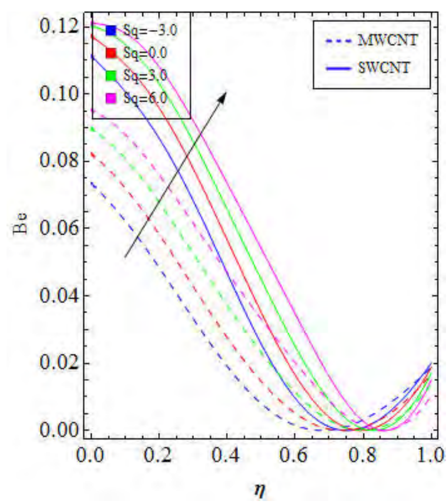

Fig. 4.8: Be for higher Sq.

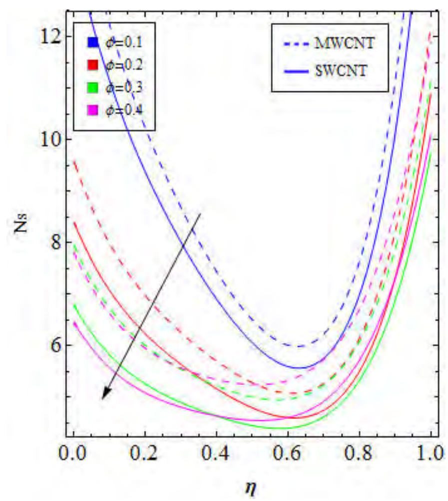

Fig. 4.9: Ns for higher ϕ.

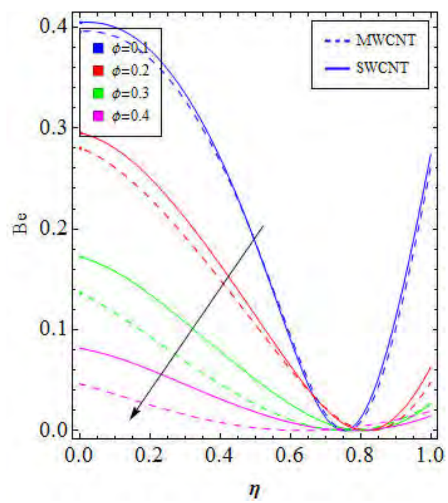

Fig. 4.10: Be for higher ϕ.

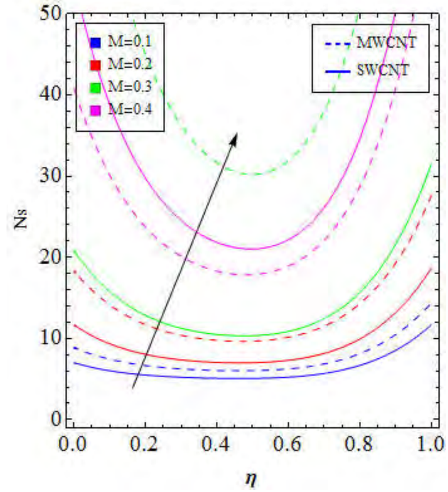

Fig. 4.11: Ns for higher M.

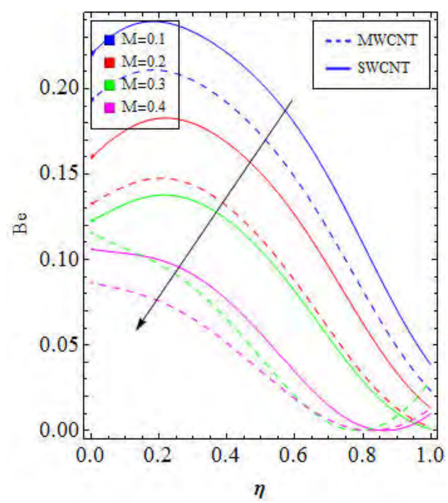

Fig. 4.12: Be for higher M.

4.5 Closing remarks

The key points of presented analysis are

- Intensification in flow is observed with the increment of Sq, ϕ and M.
- Decay in temperature is noted against Sq, ϕ and M.
- Single-walled CNTs shows overriding behavior than multiple-walled CNTs in terms of both flow and temperature.
- Intensification in heat transfer is analyzed for larger Sq, ϕ and M.

- Bejan number is an increasing function of Sq while it reduces for ϕ and M.
- Role of multiple-walled CNTs is prominent than single-walled CNTs for both entropy generation and Bejan number.

Chapter 5

Squeezed flow of Jeffrey nanomaterial with convective heat and mass conditions

5.1 Introduction

Time-dependent squeezed flow of Jeffrey nanofluid is discussed in this chapter. Brownian motion and thermophoresis effects are addressed. Convection conditions of heat and mass transfer are implemented. The resulting differential systems are computed for convergent solutions. The permissible values for convergence analysis are identified. Detail analysis is carried out for velocity, concentration, temperature, skin friction, Nusselt and Sherwood numbers.

5.2 Modeling

Consider unsteady nanofluid flow of Jeffrey material within two parallel plates. The plate at $y = 0$ (lower plate) is fixed while the plate at $y = h(t) = \sqrt{\frac{v(1-ct)}{U_0}}$ (upper plate) squeezed towards lower plate with velocity $v_h = \frac{dh}{dt}$. Brownian motion and thermophoresis are considered. Heat and mass transport is explored through convective conditions. Here x and y-axes in Cartesian coordinate system are perpendicular to each other. Under the mentioned assumptions the relevant equations are

$$\frac{\partial u}{\partial x}+\frac{\partial v}{\partial y}=0, \tag{5.1}$$

$$\rho_f(\frac{\partial u}{\partial t}+u\frac{\partial u}{\partial x}+v\frac{\partial u}{\partial y})=-\frac{\partial p}{\partial x}+\frac{\mu_f}{1+\lambda_2}(\frac{\partial^2 u}{\partial x^2}+\frac{\partial^2 u}{\partial y^2})$$

$$+\frac{\mu_f\lambda_3}{1+\lambda_2}\left(\begin{array}{c}\frac{\partial^3 u}{\partial x^2\partial t}+\frac{\partial 3u}{\partial y^2\partial t}+2\frac{\partial u}{\partial x}\frac{\partial^2 u}{\partial x^2}\\ +2\frac{\partial v}{\partial x}\frac{\partial^2 u}{\partial x\partial y}+u(\frac{\partial^3 u}{\partial x^3}+\frac{\partial^3 u}{\partial x\partial y^2})\\ +v(\frac{\partial^3 u}{\partial x^2\partial y}+\frac{\partial^3 u}{\partial y^3})+\frac{\partial u}{\partial y}(\frac{\partial^2 u}{\partial x\partial y}+\frac{\partial^2 v}{\partial x^2})\\ +\frac{\partial v}{\partial y}(\frac{\partial^2 u}{\partial y^2}+\frac{\partial^2 v}{\partial x\partial y})\end{array}\right), \tag{5.2}$$

$$\rho_f(\frac{\partial v}{\partial t}+u\frac{\partial v}{\partial x}+v\frac{\partial v}{\partial y})=-\frac{\partial p}{\partial y}+\frac{\mu_f}{1+\lambda_2}(\frac{\partial^2 v}{\partial x^2}+\frac{\partial^2 v}{\partial y^2})$$

$$+\frac{\mu\lambda_3}{1+\lambda_2}\left(\begin{array}{c}\frac{\partial^3 v}{\partial x^2\partial t}+\frac{\partial 3v}{\partial y^2\partial t}+2\frac{\partial v}{\partial y}\frac{\partial^2 v}{\partial y^2}\\ +2\frac{\partial u}{\partial y}\frac{\partial^2 v}{\partial x\partial y}+u(\frac{\partial^3 v}{\partial x^3}+\frac{\partial^3 v}{\partial x\partial y^2})\\ +v(\frac{\partial^3 v}{\partial x^2\partial y}+\frac{\partial^3 v}{\partial y^3})+\frac{\partial u}{\partial x}(\frac{\partial^2 u}{\partial x\partial y}+\frac{\partial^2 v}{\partial x^2})\\ +\frac{\partial v}{\partial x}(\frac{\partial^2 u}{\partial y^2}+\frac{\partial^2 v}{\partial x\partial y})\end{array}\right), \tag{5.3}$$

$$\frac{\partial T}{\partial t}+u\frac{\partial T}{\partial x}+v\frac{\partial T}{\partial y}=\alpha_f(\frac{\partial^2 T}{\partial x^2}+\frac{\partial^2 T}{\partial y^2})$$

$$+\tau_0(D_B(\frac{\partial C}{\partial x}\frac{\partial T}{\partial x}+\frac{\partial C}{\partial y}\frac{\partial T}{\partial y})+\frac{D_T}{T_m}((\frac{\partial T}{\partial x})^2+(\frac{\partial T}{\partial y})^2)), \tag{5.4}$$

$$\begin{aligned}\frac{\partial C}{\partial t}+u\frac{\partial C}{\partial x}+v\frac{\partial C}{\partial y} &= D_{B^*}(\frac{\partial^2 C}{\partial x^2}+\frac{\partial^2 C}{\partial y^2})+\frac{D_T}{T_h}(\frac{\partial^2 T}{\partial x^2}+\frac{\partial^2 T}{\partial y^2}),\\ \text{in which}\qquad \tau_0 &= \frac{\rho_f(c_p)_f}{\rho_{np}(c_p)_{np}}.\end{aligned} \tag{5.5}$$

Boundary conditions are

$$u=U_w(x)=0,\quad v=-V_0,\quad -k\frac{\partial T}{\partial y}=\gamma_0(T_f-T),\quad D_{B^*}\frac{\partial C}{\partial y}=\gamma_1(C_f-C)\quad \text{at}\quad y=0,$$

$$u=0,\quad v=v_h=\frac{dh}{dt},\quad T=T_h,\quad C=C_h\quad \text{at}\quad y=h(t). \tag{5.6}$$

After eliminating pressure gradient from Eqs. 5.2 and 5.3, we consider the following transformations

$$\eta = \frac{y}{h(t)}, \qquad u = (\frac{U_0 x}{2(1-ct)}) f'(\eta), \qquad v = -\sqrt{\frac{U_0 v_f}{1-ct}} f(\eta), \qquad \theta(\eta) = \frac{T-T_h}{T_f - T_h},$$

$$\phi(\eta) = \frac{C - C_h}{C_f - C_h}. \tag{5.7}$$

After implementation of the mentioned transformations, conservation of mass is verified trivially while other equations become

$$f^{(iv)} + (1+\lambda_2)\left(ff''' - f'f''\right) - \frac{Sq}{2}(1+\lambda_1)\left(3f'' + \eta f'''\right)$$

$$+\beta\left(2f''f''' - f'f^{(iv)} + \frac{Sq}{2}\left(\eta f^{(v)}\right) + 5f^{(iv)} - ff^{(v)}\right) = 0, \tag{5.8}$$

$$\theta'' + \Pr\left(N_b\theta'\phi' + N_t\theta'^2 + Sq(f\theta') - \eta\theta'\right) = 0, \tag{5.9}$$

$$\phi'' + (\frac{N_t}{N_B})\theta'' + ScSq(f\phi' - \eta\phi') = 0, \tag{5.10}$$

$$f(0) = 0, \qquad f'(0) = 0, \qquad \theta'(0) = -\beta_1(1-\theta(0)), \qquad \phi'(0) = -\beta_2(1-\phi(0)),$$

$$f'(1) = 0, \qquad f(1) = 1, \qquad \theta(1) = 0, \qquad \phi(1) = 0. \tag{5.11}$$

The dimensionless parameters are:

$$Sq = \frac{c}{U_0}, \qquad \Pr = \frac{v}{\alpha}, \qquad \beta = \frac{\lambda_3 U_0}{1-ct}, \qquad N_b = D_{B^*}\tau_0(\frac{C_f - C_h}{v}), \qquad Le = \frac{\alpha_f}{D_{B^*}},$$

$$N_t = \frac{D_T T_w \tau_0}{v_f T_h}(T_f - T_h), \qquad \beta_1 = \frac{\gamma_o}{k_f}\sqrt{\frac{\nu_f(1-ct)}{U_0}}, \qquad \beta_2 = \frac{\gamma_1}{D_{B^*}}\sqrt{\frac{\nu_f(1-ct)}{U_0}}. \tag{5.12}$$

Skin friction and local Nusselt and Sherwood numbers are

$$C_{fx} = \frac{(\tau_{wx})_{y=h(t)}}{\rho_f v_h^2}, \tag{5.13}$$

$$\tau_{wx} = \frac{\mu_f}{1+\lambda_2}(\frac{\partial u}{\partial y} + \frac{\partial v}{\partial x} + \lambda_3(\frac{\partial^2 u}{\partial y \partial t} + \frac{\partial^2 v}{\partial x \partial t} + u\frac{\partial^2 u}{\partial x \partial y} + v\frac{\partial^2 v}{\partial x \partial y} + u\frac{\partial^2 v}{\partial x^2} + v\frac{\partial^2 u}{\partial y^2})), \tag{5.14}$$

$$Nu_x = \frac{xq_w}{k_f(T_f - T_h)}, \qquad q_w = -k_f(\frac{\partial u}{\partial y})_{y=0}, \tag{5.15}$$

$$Sh_x = \frac{-x(\frac{\partial C}{\partial y})_{y=0}}{D_{B^*}(C_f - C_h)}. \tag{5.16}$$

In dimensionless form

$$C_{fx}\sqrt{\mathrm{Re}} = \frac{1}{1+\lambda_2}(f''(1) + \frac{\beta}{2}(f'''(1) + (3f''(1) - \frac{Sq}{2}f'''(1)), \tag{5.17}$$

$$\frac{Nu_x}{\sqrt{\mathrm{Re}}} = -\theta'(0) \quad \text{and} \quad \frac{Sh_x}{\sqrt{\mathrm{Re}}} = -\phi'(0), \tag{5.18}$$

where $\mathrm{Re} = \sqrt{\frac{(1-ct)v_f}{U_0}}$ represents local Reynolds number.

5.3 Series solutions

Obtained finalized ODEs are solved via HAM. Thus the initial guesses and operators are

$$f_0(\eta) = \frac{1}{2}(3Sq\eta^2 - 2Sq\eta^3), \qquad \theta_0(\eta) = \frac{\beta_1 - \beta_1\eta}{1+\beta_1} \quad \text{and} \quad \phi_0(\eta) = \frac{\beta_2 - \beta_2\eta}{1+\beta_2}. \tag{5.19}$$

$$\mathcal{L}_f(f) = \frac{d^4 f}{d\eta^3}, \qquad \mathcal{L}_\theta(\theta) = \frac{d^2\theta}{d\eta^2} \quad \text{and} \quad \mathcal{L}_\phi(\phi) = \frac{d^2\phi}{d\eta^2}. \tag{5.20}$$

5.3.1 Analysis for convergence

Fig. 5.1 is labeled for $\hbar_f$, $\hbar_\theta$ and $\hbar_\phi$ and its ranges of acceptance are $\hbar_f \epsilon[-0.9\ -0.1]$, $\hbar_\theta \epsilon[-1.6\ -0.1]$ and $\hbar_\phi \epsilon[-1.5\ -0.5]$.

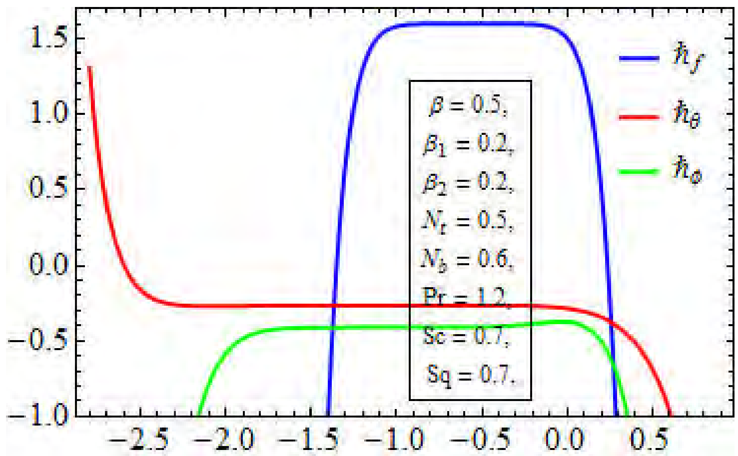

Fig. 5.1. Curves for $\hbar_f$, $\hbar_\theta$ and $\hbar_\phi$.

5.4 Analysis

Graphical results of involved parameters on flow, temperature, concentration, skin friction, heat and mass transfer rates are physically discussed in this section. Figs. 5.2-5.4 display the variation of flow due to Sq, λ_1 and β respectively. Flow rises with an increment in Sq. Physically $Sq < 0$ represents that the squeezing plate (upper plate) moves away from the fixed plate (lower plate). Hence in case $Sq > 0$, a force (squeezing force) in exerted on liquid due to which the flow rises. Reduction in flow in seen for larger λ_1. Physically λ_1 is referred to viscoelastic parameter (posses both viscous and elastic effects). Thus flow and corresponding penetration depth are retarded larger viscosity or elasticity. Intensification in flow is noted for larger β. As β involved λ_2 (retardation time). So larger λ_2 lead to rise in flow. Temperature variations due to Sq, β_1, N_b, N_t and Pr are plotted in Figs. 5.5-5.9. Increment in Sq (for $Sq > 0$) leads to less collision between fluid particles. It results in decay of fluid temperature. Temperature and associated depth enlarges for larger β_1. Physically an increment in β_1 leads to higher rate of heat transfer which intensifies temperature. Fluid temperature rises for both N_b and N_t. Higher N_b intensify the collision between fluid particles and so temperature rises.

Also larger N_t make more stable themophoretic force and thus locomotion of nanomaterial from warm to cold region. Hence temperature is increased. Higher Pr lead to decay in both temperature and thermal layer thickness. Higher Pr is due to lower thermal diffusivity. As a result decay of temperature occurs. Figs 5.10-5.14 elaborate the impacts of Sq, Sc, N_t, N_b, and β_2 on concentration. Concentration and corresponding penetration depth are reduced with increment in Sq (for $Sq > 0$). Reduction in concentration is also noticed for higher Sc. Sc refers as ratio of viscosity to mass diffusion (momentum to mass diffusivity). Hence an increment in Sc decays mass diffusion and thus concentration reduced. Higher N_t rises concentration. In fact higher N_t lead to thermophoretic force. Increment in N_b reduce both concentration and associated penetration depth. Concentration is also enhanced by larger β_2. Figs. 5.15 and 5.16 are plotted for variations in skin friction coefficient due to β, λ_1 and Sq. Skin friction increases with increments in β and Sq while it decays for λ_1. Heat transfer rate against $Sq, \Pr, \beta_1$ and N_b is portrayed in Figs. 5.17-5.19. Intensification in heat transfer rate is observed against mentioned parameters. Mass transfer rate against N_b, N_t, Sq and β_2 is labeled in Figs.5.20 and 5.21. Mass transfer rate is an increasing function of mentioned parameters.

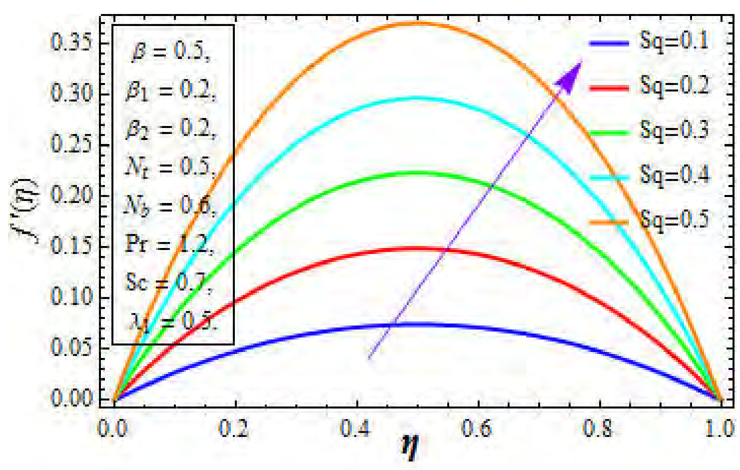

Fig. 5.2: $f'(\eta)$ for higher Sq.

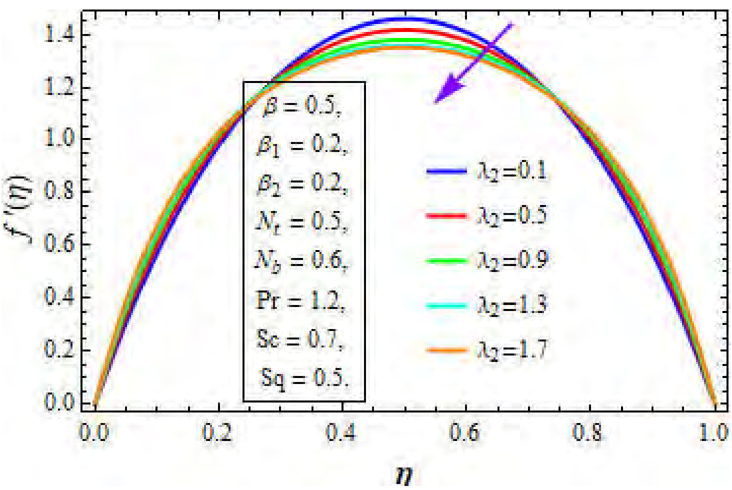

Fig. 5.3: $f'(\eta)$ for higher λ_2.

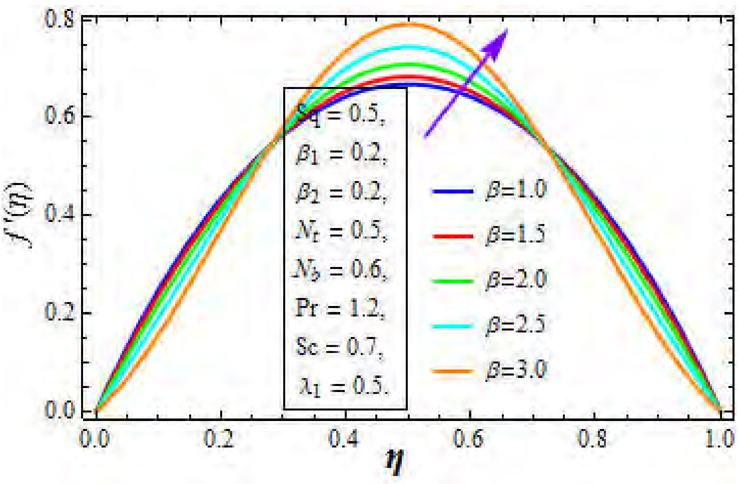

Fig. 5.4: $f'(\eta)$ for higher β.

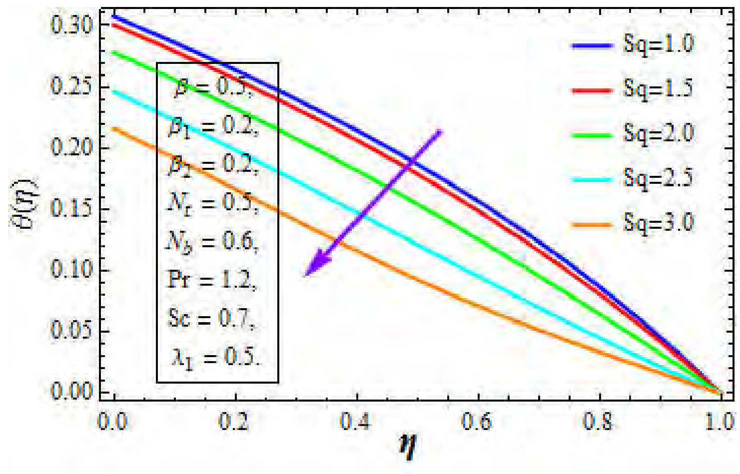

Fig. 5.5: $\theta(\eta)$ for higher Sq.

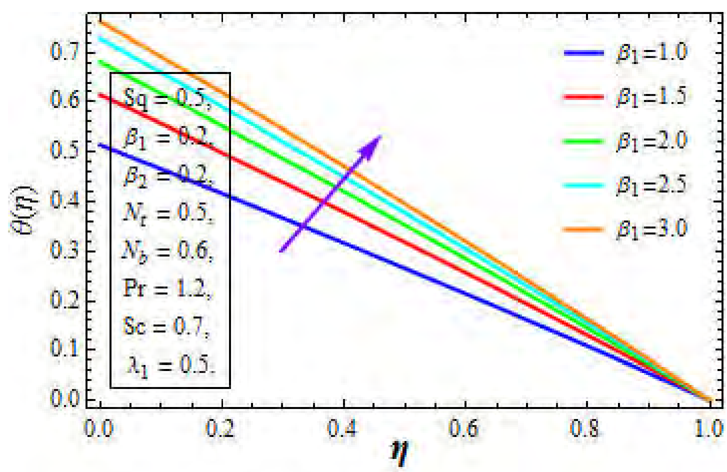

Fig. 5.6: $\theta(\eta)$ for higher β_1.

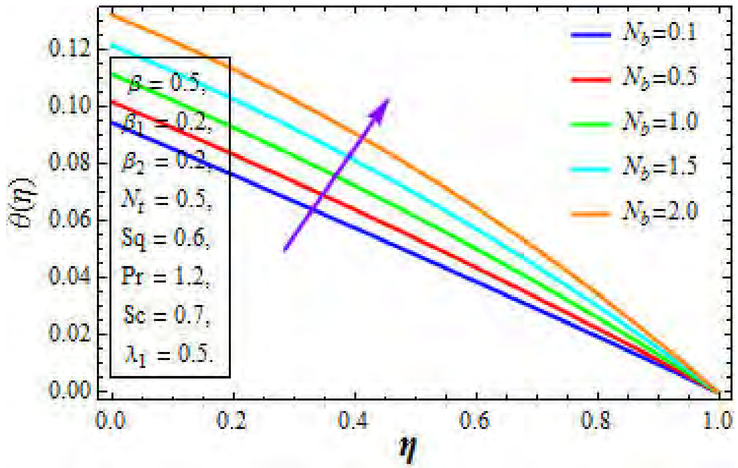

Fig. 5.7: $\theta(\eta)$ for higher N_b.

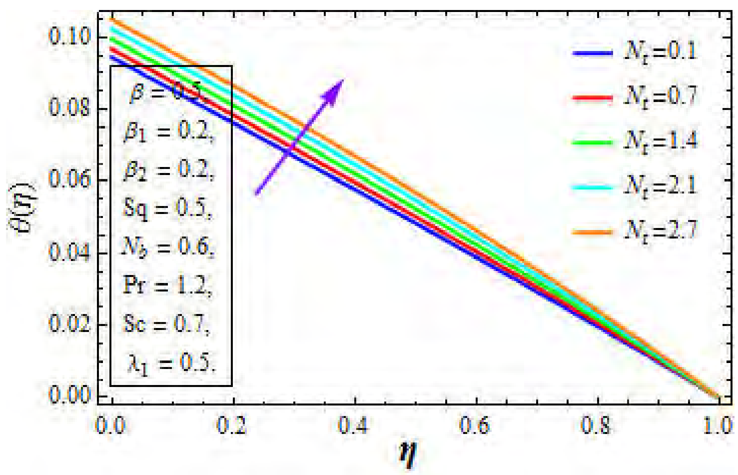

Fig. 5.8: $\theta(\eta)$ for higher N_t.

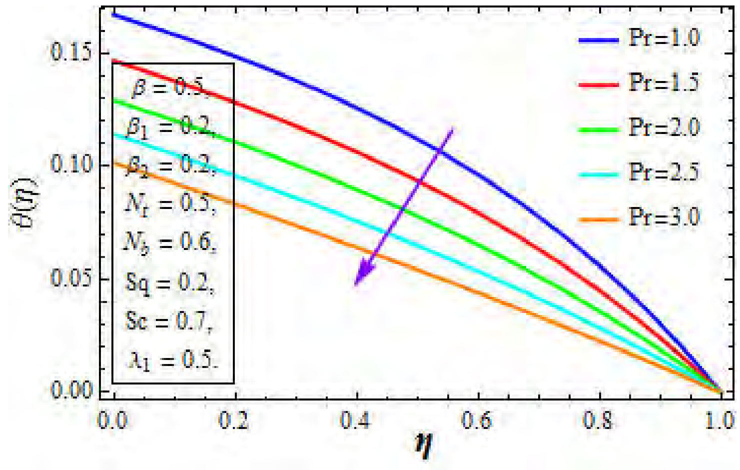

Fig. 5.9: $\theta(\eta)$ for higher Pr.

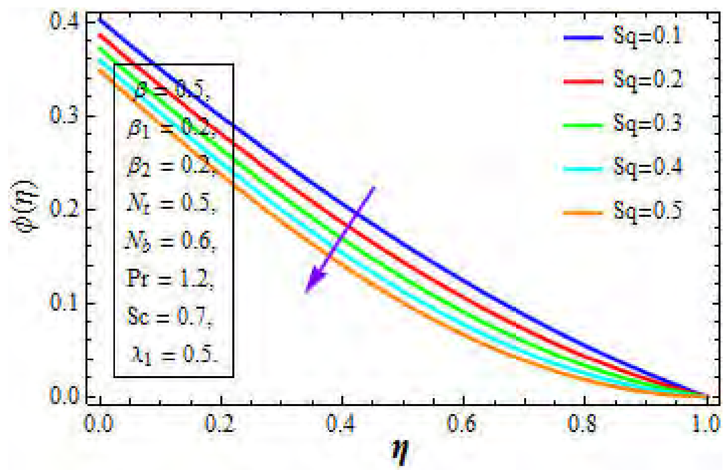

Fig. 5.10: $\phi(\eta)$ for higher Sq.

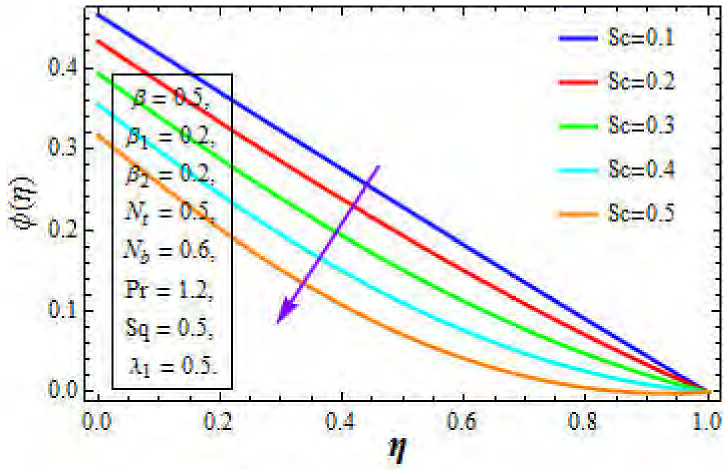

Fig. 5.11: $\phi(\eta)$ for higher Sc.

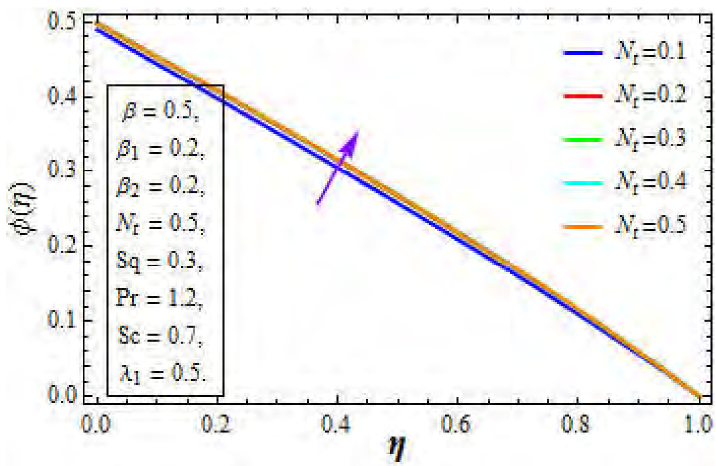

Fig. 5.12: $\phi(\eta)$ for higher N_t.

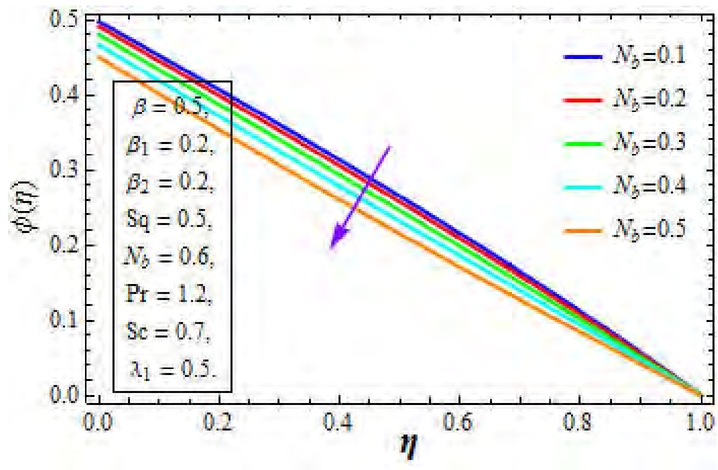

Fig. 5.13: $\phi(\eta)$ for higher N_b.

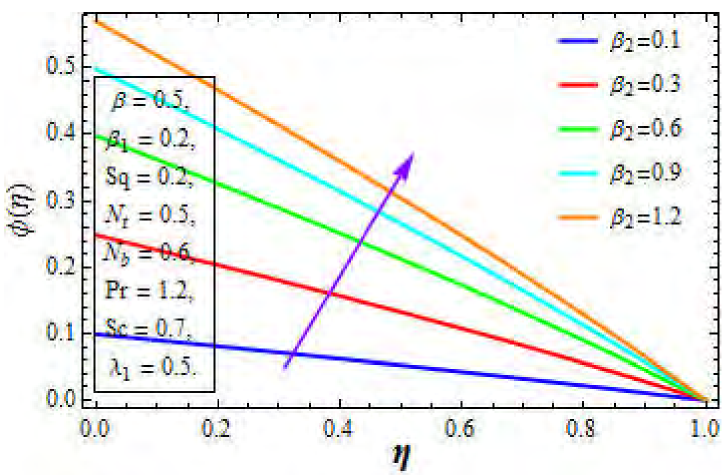

Fig. 5.14: $\phi(\eta)$ for higher β_2.

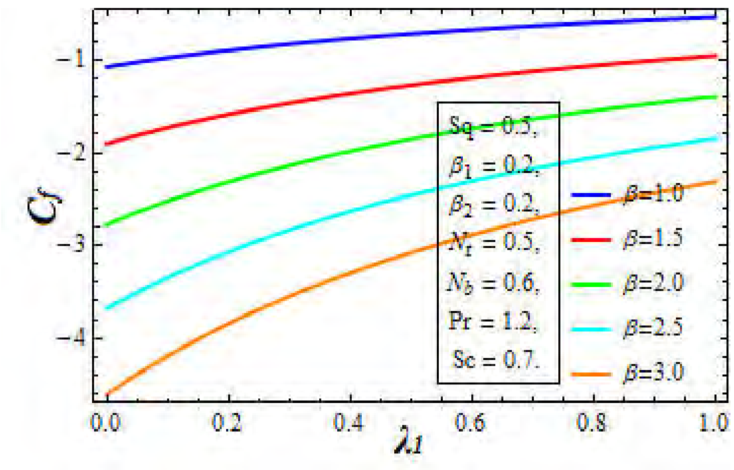

Fig. 5.15: C_f for higher β and λ_1.

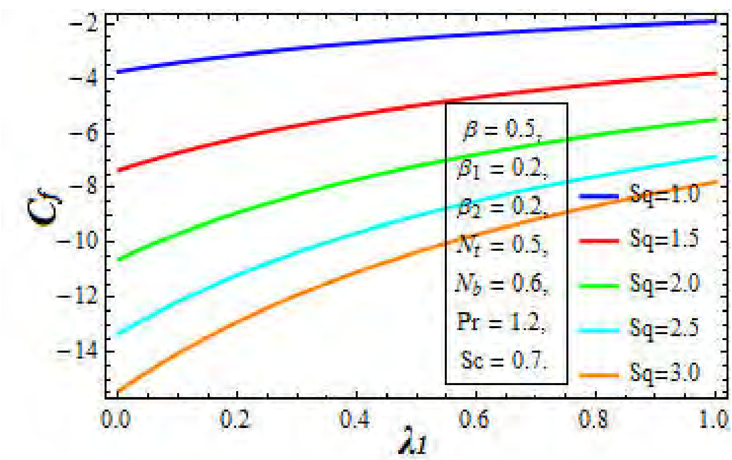

Fig. 5.16: C_f for higher Sq and λ_1.

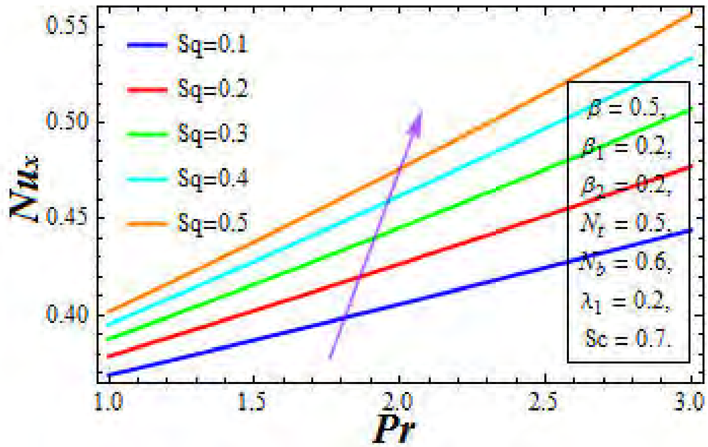

Fig. 5.17: Nu_x for higher Sq and Pr.

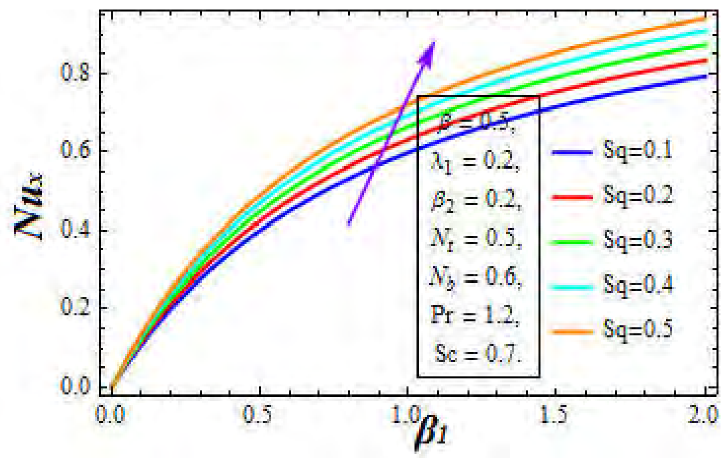

Fig. 5.18: Nu_x for higher Sq and β_1.

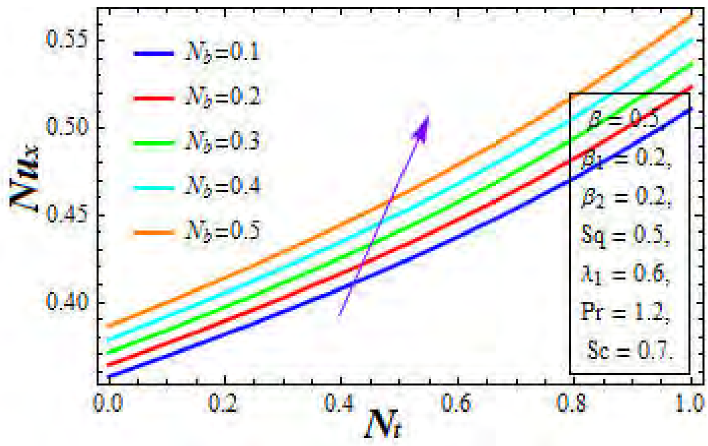

Fig. 5.19: Nu_x for higher N_t and N_b.

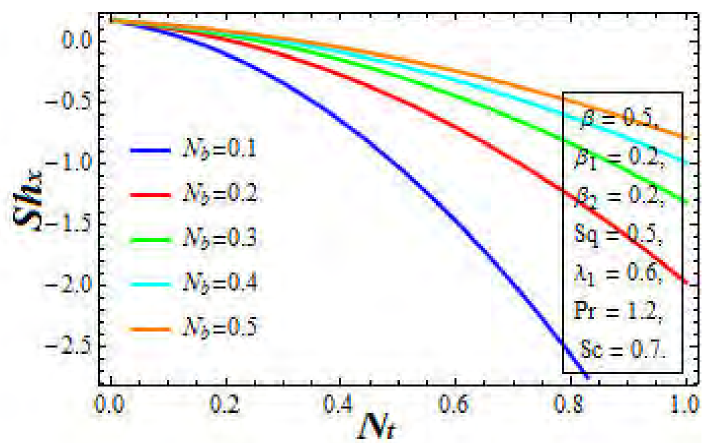

Fig. 5.20: Sh_x for higher N_t and N_b.

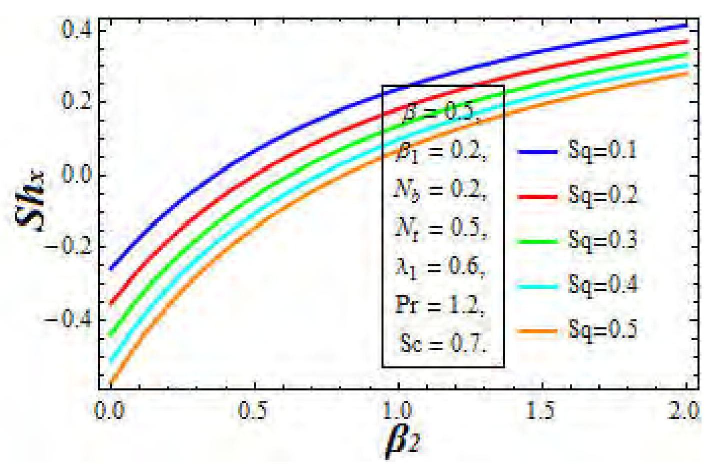

Fig. 5.21: Sh_x for higher Sq and β_2.

5.5 Key points

Major results of presented chapter are listed below.

- Intensification in flow is noted for increment of Sq, β while opposite trend is seen for higher λ_2.
- Increment in fluid temperature is observed for larger β_1, N_b, N_t while reverse impact on temperature is examined for Sq and $\Pr$.
- Increment in Sq, Sc and N_t leads to decay of concentration.
- Skin friction coefficient decays for λ_2.
- Heat transfer rate rises for higher $Sq, \Pr, \beta_1, N_t$ and N_b.
- An increase in mass transfer is seen with increment of Sq and N_t.

Chapter 6

Melting effect in MHD stagnation point flow of Jeffrey nanomaterial

6.1 Introduction

Our main intention in this chapter is to investigate melting phenomenon in magnetohydrodynamic flow of Jeffrey nanomaterial by a stretching surface. Mechanism of heat transfer is elaborated via Joule heating and viscous dissipation. Thermophoretic and Brownian motion characteristics are analyzed via Boungiorno nanofluid model. Additionally the chemical reaction is studied via activation energy. Further flow is addressed in stagnation point region. Flow field expressions (PDEs) are converted to ODEs via implementation of adequate transformations. The coupled non-linear systems of ODEs are solved via OHAM (Optimal homotopy analysis method). Velocity, skin friction coefficient, concentration, mass transfer rate (Sherwood number), temperature and heat transfer rate (Nusselt number) are examined. Flow can be controlled thorough higher estimations of Hartman number and ratio of relaxation to retardation time parameter. Temperature of fluid intensifies with larger thermophorasis parameter, Eckert number, Prandtl number, Hartman number and velocity ratio parameter. Concentration of fluid is higher for larger estimation of thermophorasis parameter, Brownian motion parameter and activation energy parameter. Further skin friction coefficient can be reduced via higher melting parameter, velocity ratio parameter and ratio of relaxation to retardation time parameter. Nusselt number enhances for Deborah number and thermophorasis parameter. Sherwood number is larger for higher Brownian motion parameter and reaction rate parameter.

6.2 Mathematical modeling

Magnetohydrodynamic stagnation point flow of an electrically conducting Jeffrey material is considered. Brownian motion and thermophoerasis characteristics are studied via Boungiorno nanofluid model. A transverse magnetic field is applied normal to flow. Induced magnetic field is neglected due to very low magnetic Reynolds number. Heat transport characteristics are examined via melting effect, Joule heating and viscous dissipation. Binary chemical reaction with activation energy is presented. Sheet is stretched along $x-$axis while $y-$axis normal to it (see Fig. (1)). After implementation of boundary layer approximations ($o(u) = o(1) = o(x)$ and $o(v) = o(\delta) = o(y)$), we get the relevant expressions with associated boundary conditions as

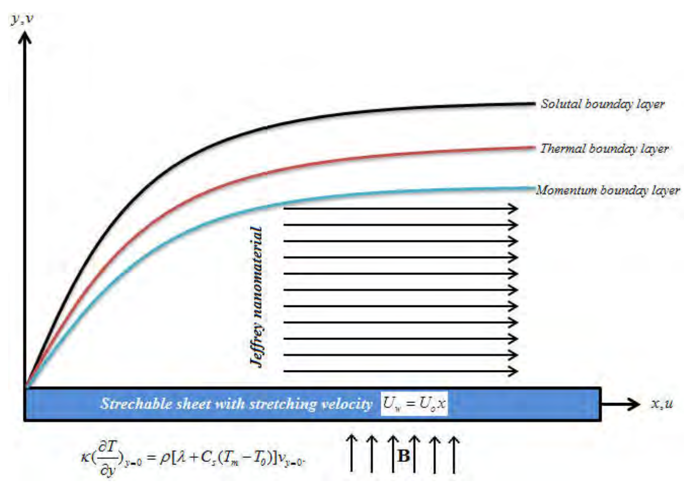

Fig. 6.1: Geometry for flow field.

$$\frac{\partial u}{\partial x} + \frac{\partial v}{\partial y} = 0, \tag{6.1}$$

$$\frac{\partial u}{\partial t} + u\frac{\partial u}{\partial x} + v\frac{\partial u}{\partial y} = U_e(x)\frac{dU_e(x)}{dx} + \frac{\sigma}{\rho_f}B_o^2 U_e(x) + \frac{v_f}{1+\lambda_2}\frac{\partial^2 u}{\partial y^2} + \frac{v_f\lambda_3}{1+\lambda_2}\begin{pmatrix} u\frac{\partial^3 u}{\partial x\partial y^2} \\ +v\frac{\partial^3 u}{\partial y^3} \\ +\frac{\partial^2 u}{\partial x\partial y}\frac{\partial u}{\partial y} \\ +\frac{\partial^2 u}{\partial y^2}\frac{\partial v}{\partial y} \end{pmatrix} - \frac{\sigma}{\rho}B_o^2 u, \tag{6.2}$$

$$u\frac{\partial T}{\partial x} + v\frac{\partial T}{\partial y} + \alpha_f(\frac{\partial^2 T}{\partial y^2}) + \tau_o\left(D_{B^*}\frac{\partial C}{\partial y}\frac{\partial T}{\partial y} + \frac{D_T}{T_\infty}(\frac{\partial T}{\partial y})^2\right)$$

$$+\frac{v_f}{(c_p)_f(1+\lambda_2)}(\frac{\partial^2 u}{\partial y^2})+\frac{\lambda_3 v_f}{(c_p)_f(1+\lambda_2)}\left(u\frac{\partial u}{\partial y}\frac{\partial^2 u}{\partial y^2}+u\frac{\partial u}{\partial y}\frac{\partial^2 u}{\partial y \partial x}\right), \tag{6.3}$$

$$u\frac{\partial C}{\partial x}+v\frac{\partial C}{\partial y}=D_{B^*}\frac{\partial C}{\partial y^2}+\frac{D_T}{T_\infty}\frac{\partial^2 T}{\partial y^2}-k_r^2 e^{-\frac{E_1 a}{k_2 t}(\frac{T}{T_\infty})^n}(C-C_\infty), \tag{6.4}$$

$$u\,(x,y)=U_w\,(x)=U_o x, \quad v\,(x,y)=0, \quad T=T_m, \quad C=C_w \quad \text{at} \quad y=0$$

$$u\,(x,y)=U_e(x)\to U_\infty x, \quad T\to T_\infty, \quad C\to C_\infty \quad \text{when} \quad y\to\infty. \tag{6.5}$$

Melting effect satisfies

$$k_f(\frac{\partial T}{\partial y})_{y=0} = \rho\left[\lambda_1+c_s(T_m-T_0)\right]v(x,y)_{y=0}. \tag{6.6}$$

Implementing the transformations:

$$\eta=\sqrt{\frac{U_o}{v_f}}y, \quad u=U_0 x f'(\eta), \quad v=-\sqrt{v_f U_0}f(\eta),$$

$$\theta=\frac{T-T_m}{T_\infty-T_m}, \quad \phi=\frac{C-C_\infty}{C_w-C_\infty}, \tag{6.7}$$

incompressibility condition (6.1) is identically verified while other equations with associated boundary conditions become:

$$f'''+\beta((f'')^2-f'f''-ff^{(iv)})+(1+\lambda_2)\left(A^2-A(Ha)^2-Haf'-(f')^2+ff''\right)=0, \tag{6.8}$$

$$\theta''+\Pr\left(f\theta'+N_t(\theta')^2+N_b\theta'\phi'+\frac{Ec}{1+\lambda_2}(f'')^2-\frac{\beta Ec}{1+\lambda_2}(ff'''-f'f''+EcHa(f')^2)\right)=0, \tag{6.9}$$

$$\phi''+Scf\phi'+\frac{N_t}{N_b}\theta''-Sc\sigma_1(1-\delta\theta)^n e^{(-\frac{E}{1-\delta\theta})}=0, \tag{6.10}$$

$$f'(0)=1, \quad \theta(0)=0, \quad ,\phi(0)=1, \quad M\theta'(0)+\Pr f(0)=0,$$

$$f'\to A, \quad \theta\to 1, \quad \phi\to 1. \tag{6.11}$$

Associated parameters are

$$\beta=\lambda_3 U_0, \quad N_b=\frac{D_B}{v_f T_\infty}\tau_0(C_w-C_\infty), \quad N_t=\frac{D_{B^*}}{v_f T_\infty}\tau_0(T_\infty-T_m),$$

$$Ec = \frac{U_0^2 x^2}{c_{pf}\left(T_\infty - T_m\right)}, \qquad Sc = \frac{v_f}{D_{B^*}}, \qquad M = \frac{c_p\left(T_\infty - T_m\right)}{\lambda_1 + c_s\left(T_m - T_0\right)},$$

$$\Pr = \frac{\nu_f}{\alpha_f}, \qquad Ha = \frac{\sigma B_0^2}{\rho_f U_0}, \qquad \delta = 1 - \frac{T_m}{T_\infty}, \qquad E = \frac{E_1 a^*}{k_2 T_\infty}, \qquad \sigma 1 = \frac{k_r^2}{U_0}. \tag{6.12}$$

Skin friction coefficient (C_{fx}), local Nusselt number (Nu_x) and local Sherwood number (Sh_x) in dimensional form are

$$C_{fx} = \frac{2(\tau_{wx})_{y=0}}{\rho_f U_w^2}, \qquad Nu_x = \frac{x(q_w)_{y=0}}{k_f}(T_\infty - T_m), \qquad Sh_x = -\frac{x(\frac{\partial C}{\partial y})_{y=0}}{C_w - C_\infty}, \tag{6.13}$$

where

$$\tau_{xy} = \frac{\mu_f}{1+\lambda_2}\left(\frac{\partial u}{\partial y} + \frac{\partial v}{\partial x} + \lambda_3(\frac{\partial^2 u}{\partial y^2} + \frac{\partial^2 v}{\partial x \partial y} + u(\frac{\partial^2 u}{\partial x \partial y} + \frac{\partial^2 v}{\partial x^2}))\right),$$

$$U_w = U_0 x, \qquad q_w = -k_f \frac{\partial T}{\partial y}. \tag{6.14}$$

Finally

$$\frac{1}{2} C_{fx}\sqrt{\mathrm{Re}} = \frac{f''(0)}{1+\lambda_2}(1+\beta), \qquad \frac{Nu_x}{\sqrt{\mathrm{Re}}} = -\theta'(0), \qquad \frac{Sh_x}{\sqrt{\mathrm{Re}}} = -\phi'(0). \tag{6.15}$$

Here $\mathrm{Re} = \frac{U_0 x^2}{v_f}$ represents local Reynolds number.

6.3 Methodology for solution

The governed problems are solved via OHAM. Initial guesses to the solutions and linear operators are

$$f_0 = A\eta + (1-A)(1-e^{-\eta}), \quad g_0 = 1 - e^{-\eta}, \quad \phi_0 = e^{-\eta}, \tag{6.16}$$

and

$$\mathcal{L}_f\left(f\right) = f'''(\eta) - f(\eta), \qquad \mathcal{L}_\theta\left(\theta\right) = \theta''(\eta) - \theta(\eta), \qquad \mathcal{L}_\phi\left(\phi\right) = \phi''(\eta) - \phi(\eta). \tag{6.17}$$

Total error against order of approximations is visualized in Fig. 6.2 while the ASRE through

Table 6.1.

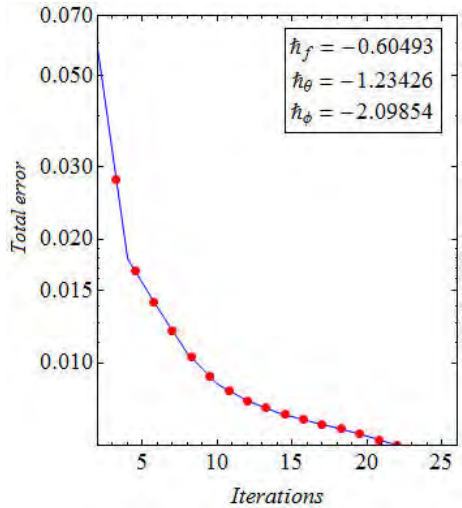

Fig. 6.2: Total error agaist k.

Thus we have

$$\varepsilon_f(\hbar_f, \hbar_\theta, \hbar_\phi) = \frac{1}{N+1} \sum_{H=0}^{N} \left[\sum_{i=0}^{k} (f_i)_{\eta=h\pi\eta} \right]^2, \tag{6.18}$$

$$\varepsilon_\theta(\hbar_f, \hbar_\theta, \hbar_\phi) = \frac{1}{N+1} \sum_{H=0}^{N} \left[\sum_{i=0}^{k} (f_i)_{\eta=j\pi\eta}, \sum_{i=0}^{k} (\theta_i)_{\eta=h\pi\eta} \right]^2, \tag{6.19}$$

$$\varepsilon_\phi(\hbar_f, \hbar_\theta, \hbar_\phi) = \frac{1}{N+1} \sum_{H=0}^{N} \left[\sum_{i=0}^{k} (f_i)_{\eta=j\pi\eta}, \sum_{i=0}^{k} (\theta_i)_{\eta=h\pi\eta}, \sum_{i=0}^{k} (\phi_i)_{\eta=h\pi\eta} \right]^2. \tag{6.20}$$

Table. 6.1. Various order of approximations and average square residual errors.

	Average square residual error		
Various approximation (k)	ε_k^f	ε_k^θ	ε_k^ϕ
2	1.14773×10^{-5}	3.60742×10^{-3}	2.19886×10^{-3}
4	6.12835×10^{-6}	1.44109×10^{-3}	3.52641×10^{-4}
6	7.1482×10^{-7}	8.71693×10^{-4}	4.92821×10^{-4}
8	2.97382×10^{-7}	8.70499×10^{-4}	1.84034×10^{-4}
10	1.76213×10^{-7}	8.48758×10^{-4}	4.03894×10^{-5}
12	1.03564×10^{-7}	7.98541×10^{-4}	1.14407×10^{-5}
14	5.94893×10^{-8}	7.52871×10^{-4}	5.72465×10^{-6}
16	3.38497×10^{-8}	7.20787×10^{-4}	3.43797×10^{-6}
18	1.95534×10^{-8}	6.93274×10^{-4}	2.00473×10^{-6}
20	1.18786×10^{-8}	6.63015×10^{-4}	1.32199×10^{-6}
22	7.74959×10^{-9}	6.30501×10^{-4}	1.14475×10^{-6}
24	5.35127×10^{-9}	5.99563×10^{-4}	1.14766×10^{-6}
26	3.7779×10^{-9}	5.72835×10^{-4}	1.18386×10^{-6}
28	2.65509×10^{-9}	5.50736×10^{-4}	1.09574×10^{-6}

6.4 Analysis

To analyze variations in skin friction coefficient ($\sqrt{\mathrm{Re}}C_f$), the velocity ($f'(\eta)$), Nusselt number ($\frac{Nu_x}{\sqrt{\mathrm{Re}}}$), temperature ($\theta(\eta)$), Sherwood number ($\frac{Sh_x}{\sqrt{\mathrm{Re}}}$) and concentration ($\phi(\eta)$) for various parameters are explained in this section. Fig. 6.2 is plotted for TRE (total residual error). The optimal convergence control parameters $\hbar_f = -0.604$, $\hbar_\theta = -1.234$ and $\hbar_\phi = -2.098$ are evaluated when $\mathrm{Pr} = 1.2$, $\lambda_2 = 0.6$, $A = 0.6$, $\beta = 0.1$, $N_t = 0.1$, $N_b = 0.2$, $Ha = 0.6$, $\sigma_1 = 0.9$, $\delta = 0.5$, $Ec = 0.5$, $Sc = 0.7$, $n = 0.5$ and $E_1 = 0.5$. Decay in TRE is examined with increase in k (number of iterations) as expected.

6.4.1 Flow ($f'(\eta)$) analysis

Impacts of $M,\ \beta,\ \lambda_2,\ A$ and Ha on velocity $(f'(\eta))$ of fluid are visualized in Figs. 6.3-6.7. Higher M lead to increment in velocity $(f'(\eta))$ of fluid. Indeed higher estimation of M lead to increment in convective flow towards melting surface from hot fluid. Thus intensification of velocity occurs. An increment in $(f'(\eta))$ is noticed for higher β. In fact higher β lead to increment in elasticity characteristics of the fluid. Thus $(f'(\eta))$ is intensified. Large λ_2 caused decay in velocity $(f'(\eta))$. Indeed λ_2 is the ratio of relaxation time to retardation time. Thus higher λ_2 lead to more relaxation time (time required from perturbed system to relaxed system) which is responsible for decay in velocity. Intensification in velocity $(f'(\eta))$ is noted for larger A. However $A < 1$ corresponds to thinning of momentum layer thickness, $A > 1$ corresponds to thickening of penetration depth while for $A = 1$ there is no formation of such layer. Further higher Ha lead to increment in Lorentz force (resistive force to flow) and so $(f'(\eta))$ decays.

6.4.2 Temperature ($\theta(\eta)$)

Behavior of temperature $(\theta(\eta))$ towards $M,\ N_t,\ N_b,\ Ec,\ \Pr$ and Ha is sketched in Figs. 6.8-6.13. Decay in temperature $(\theta(\eta))$ is seen for higher estimation of M. Indeed for larger M more cold particles are added to the heated fluid. Hence temperature of the fluid decays. Temperature $(\theta(\eta))$ is reduced with increment in N_t. Indeed due to thermophorasis the diffusion of particles form hot fluid towards cold surface intensifies. Thus temperature decays. Increment in N_b enhances the temperature $(\theta(\eta))$ of fluid. In fact higher N_b correspond to more Brownian motion due to which kinetic energy of nanofluid increases. Hence temperature $(\theta(\eta))$ intensifies. Higher Ec has a direct impact on temperature $(\theta(\eta))$. Clearly higher Ec is associated with more drag forces among fluid particles due to which production of heat increases. Hence temperature increases. Intensification in temperature $(\theta(\eta))$ is observed via higher estimations of $\Pr$ and Ha. Higher Ha is associated to more Lorentz forces. Thus heat production is higher and so temperature $(\theta(\eta))$ intensifies.

6.4.3 Concentration ($\phi(\eta)$)

Variations in concentration $(\phi(\eta))$ of nanomaterial via $Sc,\ N_t,\ N_b,\ E,\ \sigma_1,\ \delta$ and n are visualized in Figs. 6.14-6.20. Concentration $(\phi(\eta))$ reduces with higher estimation of Sc. Basically Sc is ratio of momentum to mass diffusivity. Thus higher Sc is associated with lower mass diffusion. Therefore concentration $(\phi(\eta))$ decays. Intensification in $(\phi(\eta))$ in noticed for N_t, N_b and E while reduction in $(\phi(\eta))$ is observed for higher σ_1, δ and n. Physically higher σ_1 and n lead to increase in factor $\sigma_1(1+\delta\theta)^n \exp(-\frac{E}{1+\delta\theta})$. Thus destruction of chemical reaction occurs due to which concentration rises.

6.4.4 Skin friction coefficient $(\sqrt{\mathrm{Re}}C_f)$, Nusselt number $(\frac{Nu_x}{\sqrt{\mathrm{Re}}})$ and Sherwood number $(\frac{Sh_x}{\sqrt{\mathrm{Re}}})$

Variations in skin friction coefficient $(\sqrt{\mathrm{Re}}C_f)$ via A, M, β and λ_2 are visualized in Figs. 6.21 and 6.22. Decay in skin friction coefficient in noted for higher estimations of M, A and λ_2 while it intensifies with β. Nusselt number $(\frac{Nu_x}{\sqrt{\mathrm{Re}}})$ under β, λ_2, M, A, N_t and N_b is sketched in Figs. 6.23-6.25. Heat transfer rate is higher for β and N_t while opposite response is seen for λ_2, M, A and N_b. Sherwood number $(\frac{Sh_x}{\sqrt{\mathrm{Re}}})$ under influential parameters N_t, N_b, δ, σ_1, E and n is visualized in Figs. 6.26-6.28. Intensification in rate of mass transfer is noticed for higher N_b and σ_1 whereas it reduces for higher δ, E, N_t and E. Table 6.1 is made for ASRE (average square residual error) verses various iterations (k). Clearly ASRE reduces with increasing number of iterations (k).

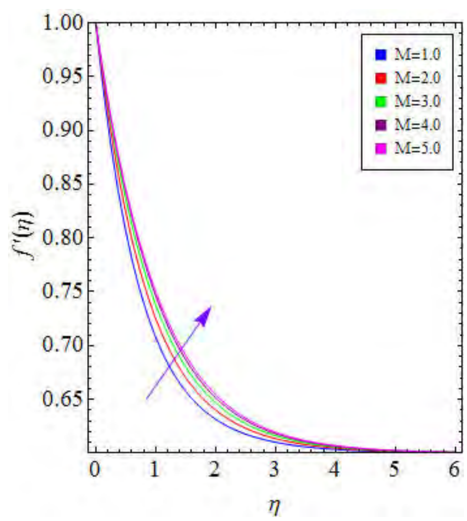

Fig. 6.3: $f'(\eta)$ for higher M.

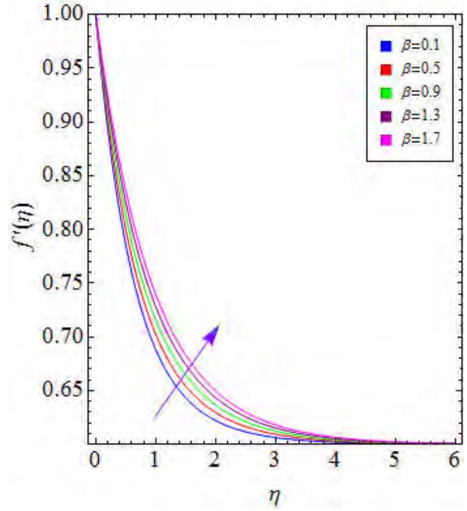

Fig. 6.4: $f'(\eta)$ for higher $.\beta$

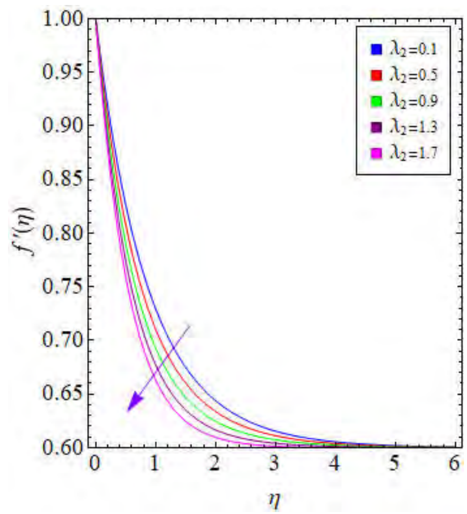

Fig. 6.5: $f'(\eta)$ for higher λ_2.

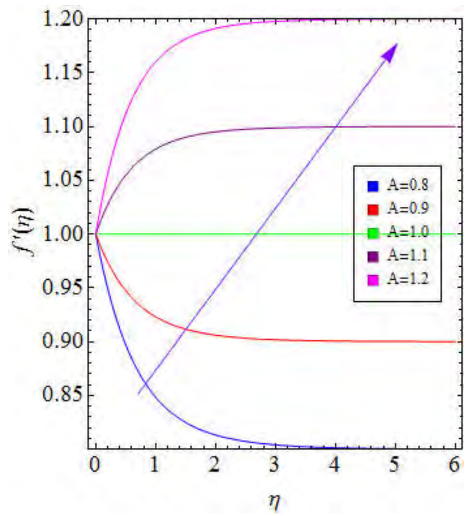

Fig. 6.6: $f'(\eta)$ for higher A.

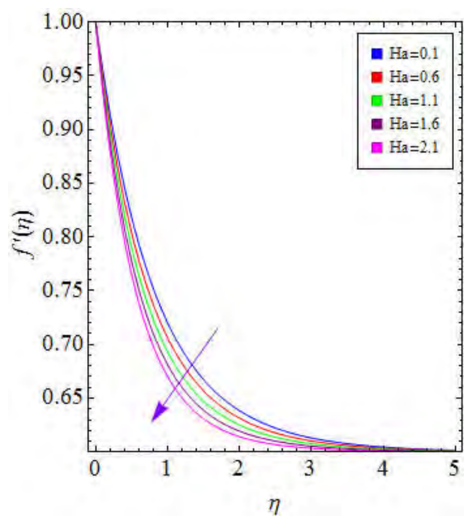

Fig. 6.7: $f'(\eta)$ for higher Ha.

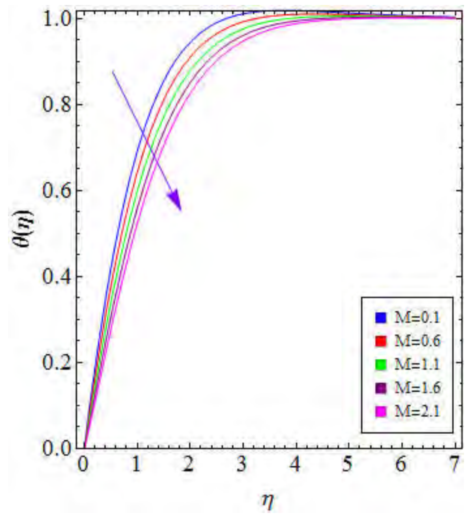

Fig. 6.8: $\theta(\eta)$ for higher M.

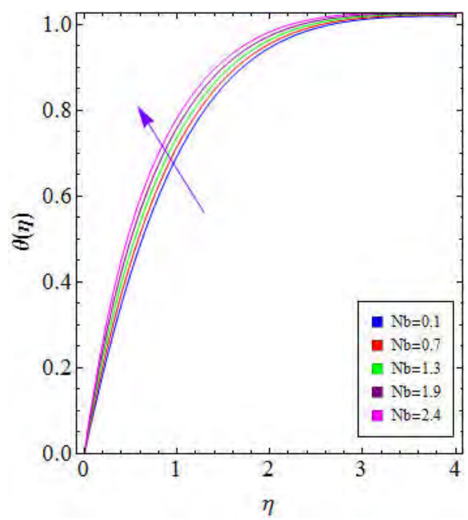

Fig. 6.9: $\theta(\eta)$ for higher N_b.

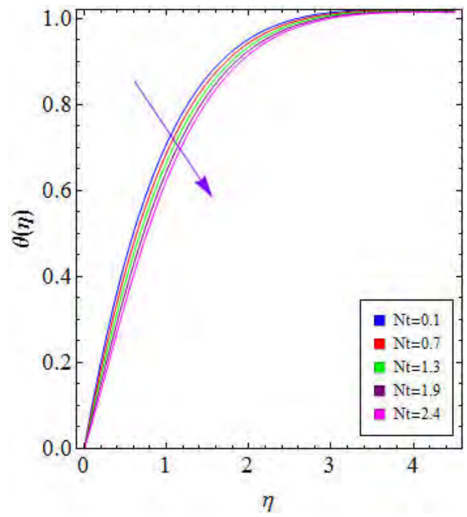

Fig. 6.10: $\theta(\eta)$ for higher N_t.

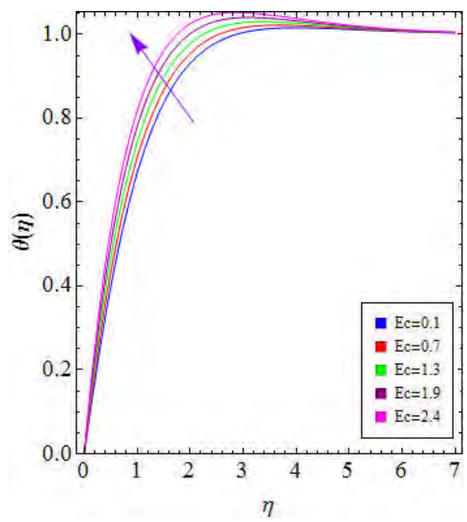

Fig. 6.11: $\theta(\eta)$ for higher Ec.

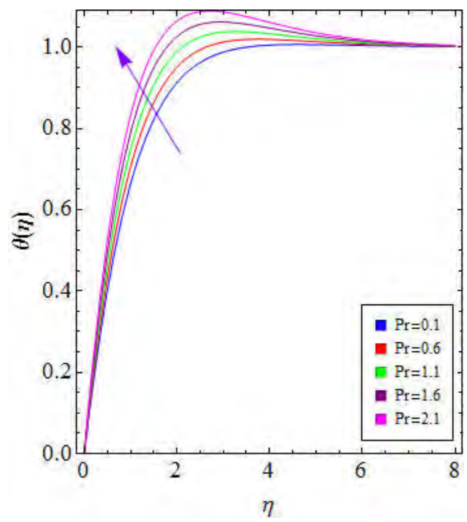

Fig. 6.12: $\theta(\eta)$ for higher Pr.

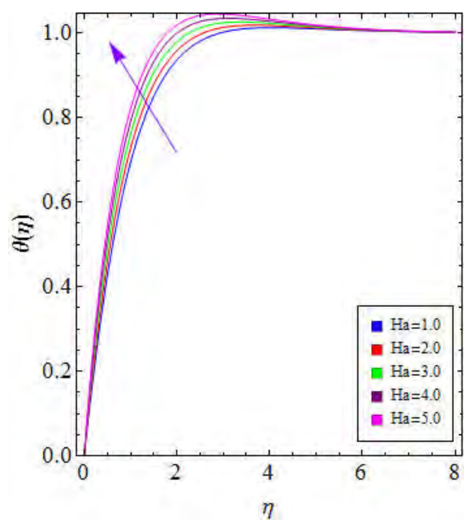

Fig. 6.13: $\theta(\eta)$ for higher Ha.

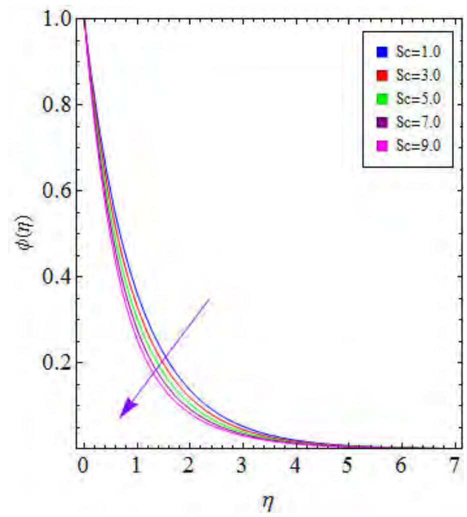

Fig. 6.14: $\phi(\eta)$ for higher Sc.

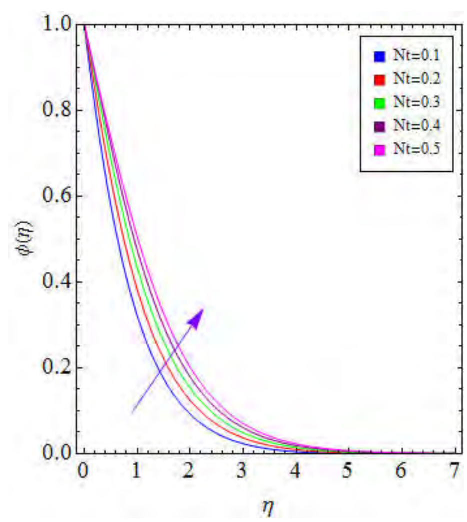

Fig. 6.15: $\phi(\eta)$ for higher N_t.

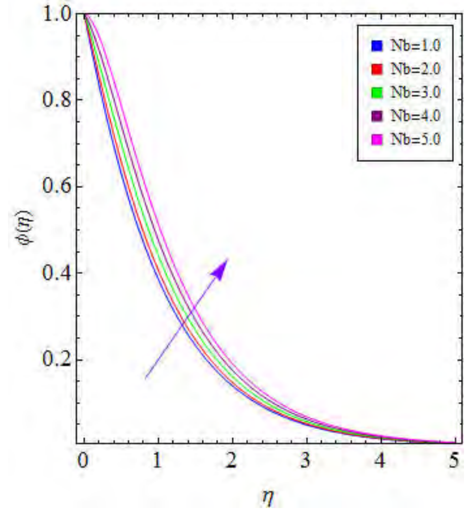

Fig. 6.16: $\phi(\eta)$ for higher N_b.

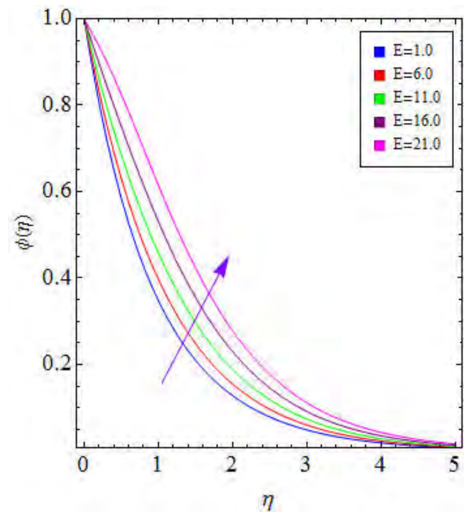

Fig. 6.17: $\phi(\eta)$ for higher E.

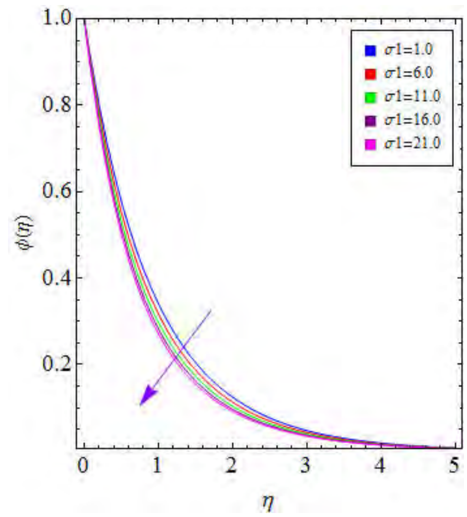

Fig. 6.18: $\phi(\eta)$ for higher σ_1.

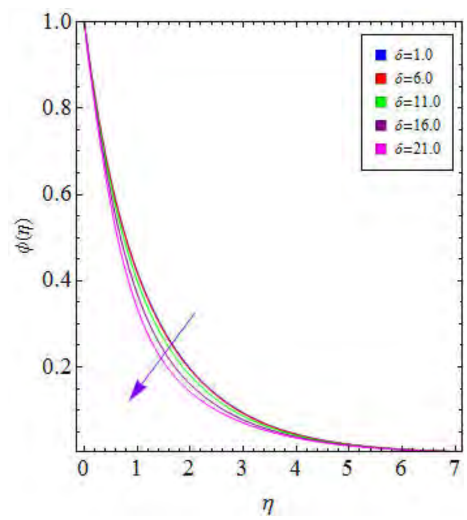

Fig. 6.19: $\phi(\eta)$ for higher δ.

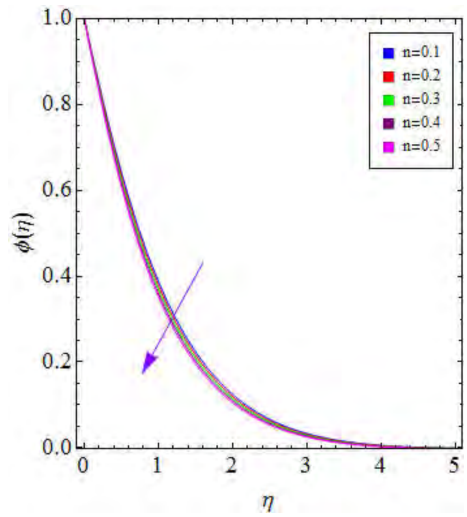

Fig. 6.20: $\phi(\eta)$ for higher n.

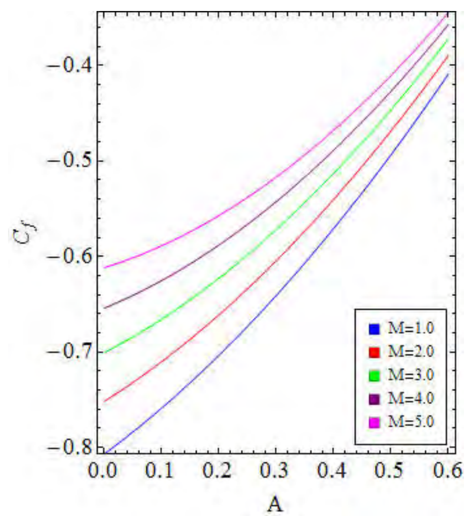

Fig. 6.21: C_f for higher M and A.

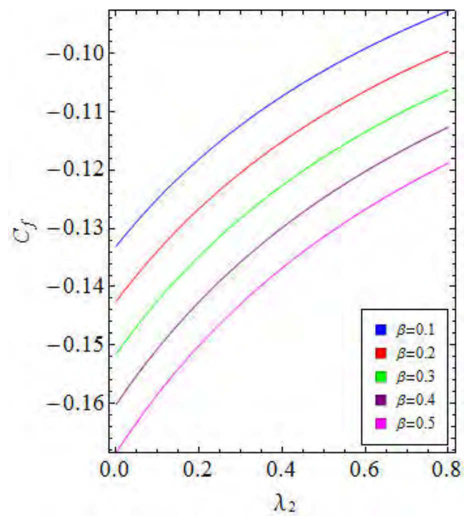

Fig. 6.22: C_f for higher λ_2 and β.

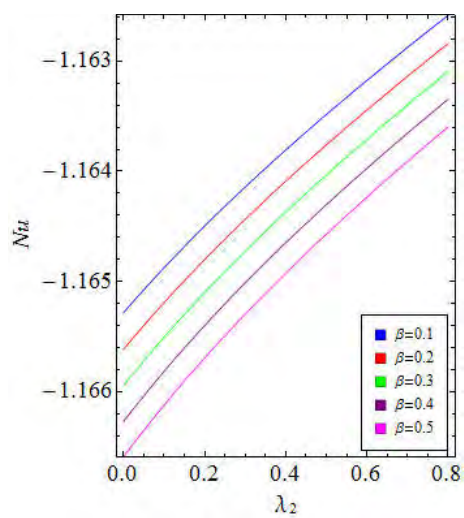

Fig. 6.23: Nu_x for higher β and λ_2.

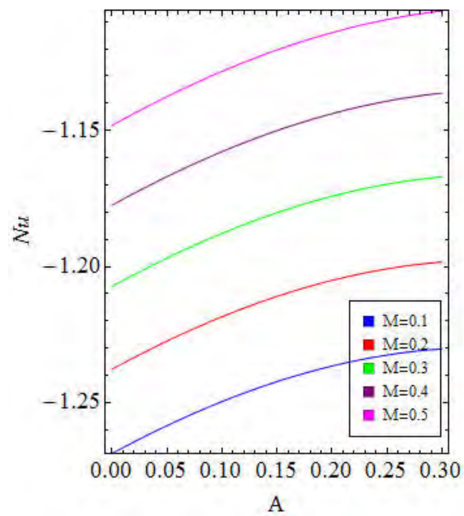

Fig. 6.24: Nu_x for higher M and A.

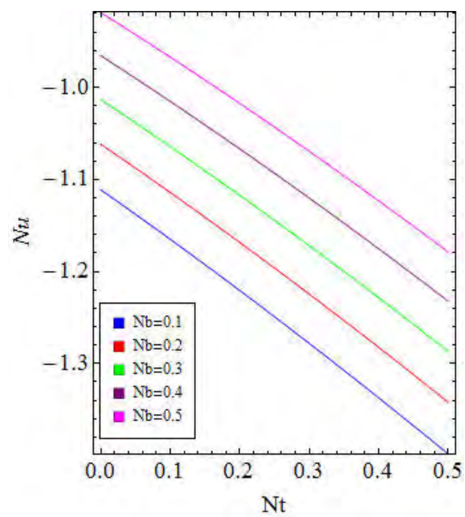

Fig. 6.25: Nu_x for higher N_t and N_b.

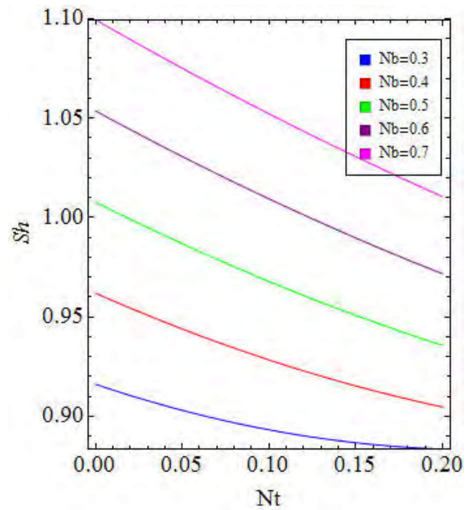

Fig. 6.26: Sh_x for higher N_t and N_b.

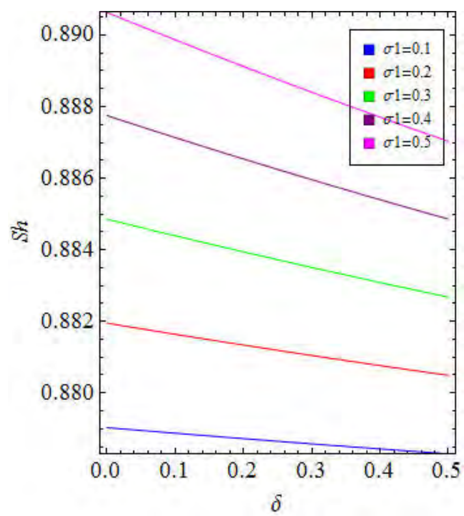

Fig. 6.27: Sh_x for higher δ and σ_1.

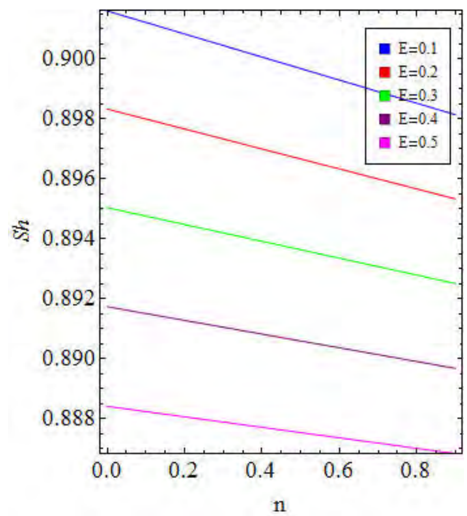

Fig. 6.28: Sh_x for higher E and n.

6.5 Conclusions

Here we have following key points.

- Flow $(f'(\eta))$ can be controlled via higher Ha and λ_2.
- Intensification in flow is noticed for larger $M,\ \beta$ and A.
- Decay in temperature $(\theta(\eta))$ of fluid is analyzed for larger estimations of M and N_b.
- Temperature of fluid rises with $N_t,\ Ec,\ \Pr,\ Ha$ and A.
- Concentration $(\phi(\eta))$ of fluid is higher for $N_t,\ N_b$ and E while reverse behavior is examined for $Sc,\ \sigma_1,\ \delta$ and n.
- Skin friction coefficient $(\sqrt{\text{Re}}C_f)$ can be controlled with higher $M,\ A$ and λ_2.
- Nusselt number $(\frac{Nu_x}{\sqrt{\text{Re}}})$ intensifies with larger estimations of β and N_t.
- Increment in Sherwood number $(\frac{Sh_x}{\sqrt{\text{Re}}})$ is noticed for larger N_b and σ_1.

Chapter 7

Thermally radiative flow of nanomaterial with viscous dissipation and convective heat and mass conditions

7.1 Introduction

This chapter addresses stagnation point flow of Jeffrey nanoliquid towards a permeable stretching cylinder. Brownian motion, thermophoresis, viscous dissipation and thermal radiation are explored. Convective heat and mass conditions are implemented. Moreover activation energy is taken into account. Suitable variables are utilized in order to convert expressions (continuity, momentum, energy and concentration) into ODEs (Ordinary differential equations). Resulting systems are solved by optimal homotopy analysis method (OHAM). Behaviors of involved flow, heat and mass transport parameters for velocity, concentration and temperature are examined graphically. Skin friction coefficient and Sherwood and Nusselt numbers are examined numerically.

7.2 Modeling

We assume steady flow of incompressible non-Newtonian nanomaterial (Jeffrey fluid) past a porous stretched cylinder. Features of nanofluid are investigated via thermophoresis and Brownian motion. Analysis of heat transport is explored in presence of viscous dissipation and thermal radiation. Convective heat and mass conditions are addressed. Cylindrical coordinates (r, x) are utilized. Flow is generated by stretching cylinder along $z-$axis in axial direction while $r-$axis being normal to it. After utilizing aforementioned assumptions and boundary layer approximations, the flow, energy and concentration expressions along with boundary conditions satisfy:

$$\frac{\partial(ru)}{\partial x}+\frac{\partial(rv)}{\partial r}=0, \tag{7.1}$$

$$u\frac{\partial u}{\partial x}+v\frac{\partial u}{\partial r}=U_e(x)\frac{dU_e(x)}{dx}+\frac{v_f}{1+\lambda_2}[\frac{\partial^2 u}{\partial r^2}+\frac{1}{r}\frac{\partial u}{\partial r}+\lambda_3(\frac{u}{r}\frac{\partial^2 u}{\partial r\partial x}+\frac{u}{r}\frac{\partial^2 v}{\partial r^2}+\frac{\partial u}{\partial r}\frac{\partial^2 u}{\partial r\partial x}$$
$$+u\frac{\partial^3 u}{\partial r^2\partial x}+\frac{\partial v}{\partial r}\frac{\partial^2 u}{\partial r^2}+v\frac{\partial^3 u}{\partial r^3})], \tag{7.2}$$

$$\rho_f c_{pf}(u\frac{\partial T}{\partial x}+v\frac{\partial T}{\partial r})=\frac{k_f}{r}\frac{\partial}{\partial r}(r\frac{\partial T}{\partial r})+\frac{16\sigma^* T_\infty^3}{3k^*}(\frac{1}{r}\frac{\partial T}{\partial r}+\frac{\partial^2 T}{\partial r^2})+\frac{\mu_f}{1+\lambda_2}[\frac{\partial^2 u}{\partial r^2}$$
$$+\lambda_3(u\frac{\partial u}{\partial r}\frac{\partial^2 u}{\partial r\partial x}+v\frac{\partial u}{\partial r}\frac{\partial^2 u}{\partial r^2})]+\rho_{np}(c_p)_{np}[D_{B^*}(\frac{\partial C}{\partial r}\frac{\partial T}{\partial r})+\frac{D_T}{T_\infty}(\frac{\partial T}{\partial r})^2], \tag{7.3}$$

$$u\frac{\partial C}{\partial x}+v\frac{\partial C}{\partial r}=D_{B^*}(\frac{\partial^2 C}{\partial r^2}+\frac{1}{r}\frac{\partial C}{\partial r})+\frac{D_T}{T_\infty}(\frac{\partial^2 T}{\partial r^2}+\frac{1}{r}\frac{\partial T}{\partial r})-k_r^2(\frac{T}{T_\infty})^n e^{-\frac{E_1 a^*}{k_2 T}}(C-C_\infty), \tag{7.4}$$

$$u=U_w(x)=U_o\frac{x}{l},\quad v=-V_0,\quad -k_f\frac{\partial T}{\partial r}=\gamma_0(T_f-T),\quad D_{B^*}\frac{\partial C}{\partial r}=\gamma_1(C_f-C)\quad \text{at}\quad r=R$$
$$u=U_e(x)\to U_\infty\frac{x}{l},\quad T\to T_\infty,\quad C\to C_\infty\quad \text{when}\quad r\to\infty. \tag{7.5}$$

In order to convert aforementioned PDEs into ODEs, we use the following transformations:

$$\eta=\frac{r^2-R^2}{2R}\sqrt{(\frac{U_0}{v_f l})},\quad u=U_0\frac{x}{l}f'(\eta),\quad v=-\frac{R}{r}\sqrt{\frac{v_f U_0}{l}}f(\eta),$$

$$\theta=\frac{T-T_\infty}{T_f-T_\infty},\quad \phi=\frac{C-C_\infty}{C_f-C_\infty}. \tag{7.6}$$

Putting above transformations in Eqs. 7.1-7.5, Eq. 7.1 is satisfied while Eqs. 7.2-7.5 become

$$(1+2\gamma\eta)f''' + 2\gamma f'' + (1+\lambda_2)\left(ff'' - f'^2\right) + \gamma\beta(f'f'' - 3ff'') + \beta(1+2\gamma\eta)(f''^2 - ff'''') + A^2 = 0, \tag{7.7}$$

$$(1+\frac{4}{3}R^*)[(1+2\gamma\eta)\theta'' + 2\gamma\theta'] + \Pr(f\theta' + N_t(\theta')^2 + N_b\theta'\phi')$$
$$+\frac{\Pr Ec}{1+\lambda_2}[(1+2\gamma\eta)(f'')^2 - \beta((1+2\gamma\eta)(ff'' - ff''f''') - \gamma ff'')] = 0, \tag{7.8}$$

$$(1+2\gamma\eta)\phi'' + 2\gamma\phi' + Scf\phi' + \frac{N_t}{N_b}[(1+2\gamma\eta)\theta'' + 2\gamma\theta'] - Sc\sigma 1\phi(1-\delta\theta)^n e^{(-\frac{E}{1-\delta\theta})} = 0, \tag{7.9}$$

$$f'(0) = 1, \quad f(0) = S, \quad \theta'(0) = -\beta_1(1-\theta(0)), \quad ,\phi'(0) = -\beta_2(1-\phi(0)),$$
$$f' \to A, \quad \theta \to 0, \quad \phi \to 0 \quad \text{as} \quad \eta \to \infty. \tag{7.10}$$

Associated variables are

$$\beta = \lambda_3\frac{U_0}{l}, \quad N_b = \frac{D_{B^*}}{v_f}\frac{\rho_{np}(c_p)_{np}}{\rho_f(c_p)_f}(C_w - C_\infty), \quad N_t = \frac{D_T}{v_f T_\infty}\frac{\rho_n c_{pn}}{\rho_f c_{pf}}(T_\infty - T_m),$$

$$A = \frac{U_\infty}{U_0}, \quad Ec = \frac{U_w^2}{(c_p)_f\,(T_w - T_\infty)}, \quad Sc = \frac{v_f}{D_B}, \quad R^* = \frac{4\sigma^* T_\infty^3}{k_f k^*}, \quad S = \sqrt{\frac{l}{v_f U_0}}V_0,$$

$$\gamma = \sqrt{\frac{lv_f}{U_0}}\frac{1}{R}, \quad \Pr = \frac{\nu_f}{\alpha_f}, \quad \delta = 1 - \frac{T_w}{T_\infty}, \quad E = \frac{E_1 a^*}{k_2 T_\infty}, \quad \sigma_1 = \frac{k_r^2}{U_0},$$

$$\beta_1 = \frac{\gamma_0 r}{k_f R}\sqrt{\frac{U_0}{v_f l}}, \quad \beta_2 = \frac{\gamma_1 r}{D_B R}\sqrt{\frac{U_0}{v_f l}}. \tag{7.11}$$

7.3 Expressions of surface friction coefficient, Sherwood number and Nusselt number

In dimensional forms we have

$$C_{fx} = \frac{2(\tau_w)_{r=R}}{\rho_f U_w^2}, \tag{7.12}$$

$$Sh_x = \frac{x(q_w)_{r=R}}{D_B(C_f - C_\infty)}, \tag{7.13}$$

$$Nu_x = \frac{x(q_{r_1})_{r=R}}{k_f(T_f - T_\infty)} + (q_r)_{r=R}, \tag{7.14}$$

where

$$\tau_{wx} = \frac{\mu_f}{1+\lambda_2}[\frac{\partial u}{\partial r} + \lambda_3(\frac{\partial^2 u}{\partial x \partial r} + v\frac{\partial^2 u}{\partial r^2})],$$

$$U_w = U_0\frac{x}{l}, \quad q_w = -D_B\frac{\partial T}{\partial y}, \quad q_{r_1} = -k_f\frac{\partial T}{\partial r} \quad \text{and} \quad q_r = -\frac{16}{3}\frac{\sigma^* T_\infty^3}{k^*}. \tag{7.15}$$

Invoking expressions 7.5 and 7.6 in Eqs. 7.12-7.15, we get dimensionless forms of C_f, Sh_x and Nu_x respectively as

$$\frac{1}{2}C_f\sqrt{\mathrm{Re}} = \frac{1}{1+\lambda_2}(1+\beta)f''(0), \quad \frac{Sh_x}{\sqrt{\mathrm{Re}}} = -\phi'(0) \quad \text{and} \quad \frac{Nu_x}{\sqrt{\mathrm{Re}}} = -(1+\frac{4}{3}R^*)\theta'(0). \tag{7.16}$$

Here $\mathrm{Re} = \frac{U_0\frac{x}{l}}{v_f}$ is known as local Reynolds number.

7.4 Solutions methodology

The governed flow, temperature and concentration expressions (PDEs) are solved by means of Optimal HAM. Initial approximations and linear operators are

$$f_0 = -S + A\eta + (1-A)(1-e^{-\eta}), \quad \theta_0 = \frac{\beta_1}{1+\beta_1}e^{-\eta}, \quad \phi_0 = \frac{\beta_2}{1+\beta_2}e^{-\eta}, \tag{7.17}$$

and

$$\mathcal{L}_f(f) = f'''(\eta) - f'(\eta), \quad \mathcal{L}_\theta(\theta) = \theta''(\eta) - \theta(\eta), \quad \mathcal{L}_\phi(\phi) = \phi''(\eta) - \phi(\eta). \tag{7.18}$$

Total error versus order of approximations (iterations) is plotted in Fig. 7.1. Table. 7.1 is constructed for ASRE versus order of approximations (k).

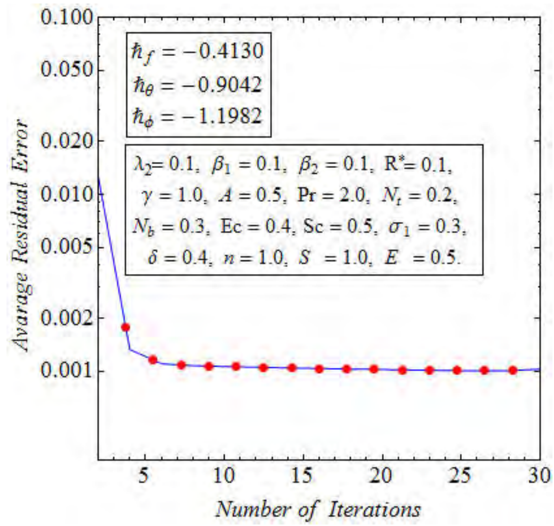

Fig. 7.1: Total error via higher iterations.

$$\epsilon_f(\hbar_f, \hbar_\theta, \hbar_\phi) = \frac{1}{M+1} \sum_{H=0}^{M} \left[\sum_{i=0}^{k} (f_i)_{\eta=h\pi\eta} \right]^2, \tag{7.19}$$

$$\epsilon_\theta(\hbar_f, \hbar_\theta, \hbar_\phi) = \frac{1}{M+1} \sum_{H=0}^{M} \left[\sum_{i=0}^{k} (f_i)_{\eta=j\pi\eta}, \sum_{i=0}^{k} (\theta_i)_{\eta=h\pi\eta} \right]^2, \tag{7.20}$$

$$\epsilon_\phi(\hbar_f, \hbar_\theta, \hbar_\phi) = \frac{1}{M+1} \sum_{H=0}^{M} \left[\sum_{i=0}^{k} (f_i)_{\eta=j\pi\eta}, \sum_{i=0}^{k} (\theta_i)_{\eta=h\pi\eta}, \sum_{i=0}^{k} (\phi_i)_{\eta=h\pi\eta} \right]^2. \tag{7.21}$$

Table 1. ASRE versus order of approximations (k) with CPU time.

Various approximation	Average square residual error			CPU
(k)	ϵ_k^f	ϵ_k^θ	ϵ_k^ϕ	Time
2	0.0117668	0.000799246	0.0000892354	1.08677 (sec)
4	0.00120522	0.0000763174	0.0000527797	5.19675 (sec)
6	0.00104837	0.0000138061	0.0000450906	16.3216 (sec)
8	0.00103228	7.42418×10^{-6}	0.0000407396	39.6874 (sec)
10	0.0010256	5.68529×10^{-6}	0.0000374021	81.9695 (sec)
12	0.00101941	4.37686×10^{-6}	0.0000349187	153.798 (sec)
14	0.0010135	3.48176×10^{-6}	0.0000329233	273.906 (sec)
16	0.00100782	2.78792×10^{-6}	0.0000312837	465.017 (sec)
18	0.00100238	2.25219×10^{-6}	0.0000298985	769.927 (sec)
20	0.000997131	1.82805×10^{-6}	0.0000287095	1258.51 (sec)
22	0.000992071	1.48978×10^{-6}	0.000027673	2043.21 (sec)
24	0.000987353	1.21866×10^{-6}	0.0000267586	3283.29 (sec)
26	0.000983615	9.99988×10^{-7}	0.0000259436	5186.08 (sec)
28	0.000985197	8.24765×10^{-7}	0.000025211	8101.64 (sec)
30	0.00100744	6.85946×10^{-7}	0.0000245469	12495.2 (sec)

7.5 Analysis

This section comprises analysis of fluid velocity ($f'(\eta)$), fluid temperature ($\theta(\eta)$), nanofluid concentration ($\phi(\eta)$), surface friction coefficient ($C_f\sqrt{\mathrm{Re}}$), Sherwood number ($\frac{Sh_x}{\sqrt{\mathrm{Re}}}$) and Nusselt number ($\frac{Nu_x}{\sqrt{\mathrm{Re}}}$) towards involved physical parameters. Optimal values of $\hbar_f$, $\hbar_\theta$ and $\hbar_\phi$ are -0.4130, -0.9042 and -0.1982 respectively. For evaluation of $\hbar_f, \hbar_\theta$ and $\hbar_\phi$, we have taken $\gamma = 0.1$, $\beta_1 = 0.1$, $R^* = 0.1$, $\gamma = 1.0$, $A = 0.5$, $\mathrm{Pr} = 2.0$, $N_t = 0.2$, $N_b = 0.3$, $Ec = 0.4$, $Sc = 0.5$, $\sigma_1 = 0.3$, $\delta = 0.4$, $S = 1.0$, $n = 1.0$ and $E = 0.5$.

7.5.1 Fluid velocity ($f'(\eta)$)

Behavior of fluid velocity ($f'(\eta)$) towards λ_2, β, γ, A, $S > 0$ and $S < 0$ is plotted in this subsection. Influence of λ_2 on $f'(\eta)$ is labeled in Fig. 7.2. Higher estimation of λ_2 correspond to decay of $f'(\eta)$. Here λ_2 is ratio of relaxation to retardations times also referred as viscoelastic parameter (posses both elastic and viscosity features). Thus $f'(\eta)$ retarded with increase in viscous or elastic effects. Impacts of β on $f'(\eta)$ are portrayed in Fig. 7.3. Rapid growth in $f'(\eta)$ is noticed with increase of β. As β is the Biot number via relaxation time. Higher β correspond to more relaxation time (time required from perturbed position to relaxed position). Here $f'(\eta)$ increases. Fluid viscosity ($f'(\eta)$) under influence of γ is expressed in Fig. 7.4. It is seen that $f'(\eta)$ enhances near surface while it reduces away from surface. Higher γ is associated with reduction in radius (R) of cylinder. Thus less particles are now stuck (due to no-slip condition) with the cylindrical surface. Hence $f'(\eta)$ decays near the surface while away from the surface it enhances. Effects of A ($A < 1$ and $A > 1$) on $f'(\eta)$ are sketched in Fig. 7.5. Fluid velocity ($f'(\eta)$) enhances for both $A < 1$ and $A > 1$. As $A = \frac{U_\infty}{U_0}$, thus for $A < 1$, $\frac{U_\infty}{U_0} < 1$ or $U_\infty < U_0$. Here reference stretching velocity is more than reference free steam velocity. Hence both $f'(\eta)$ and corresponding penetration depth increases. Also for $A < 1$, $U_0 < U_\infty$. Here reference free stream velocity dominates over reference stretching velocity. Clearly $f'(\eta)$ increases while associated penetration depth decreases. For $A = 1$, $U_0 = U_\infty$. Here both reference free stream and reference stretching velocity are equal in this case. Hence there is no formation of layer thickness. Effects of $S > 0$ and $S < 0$ on $f'(\eta)$ are plotted in Figs. 7.6 and 7.8 respectively. Both $S > 0$ and $S < 0$ disturb the flow and $f'(\eta)$ decreases.

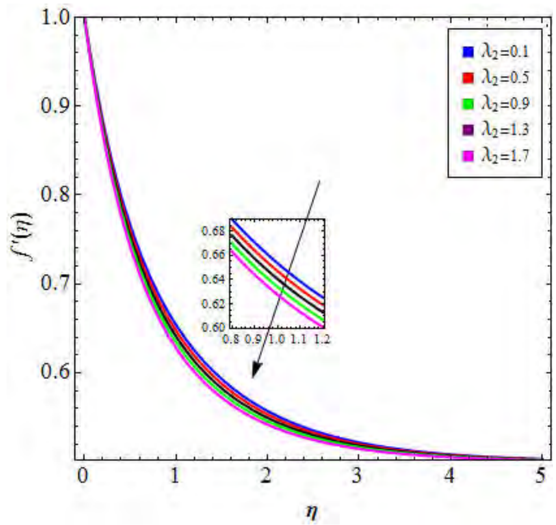

Fig. 7.2: $f'(\eta)$ for higher λ_2.

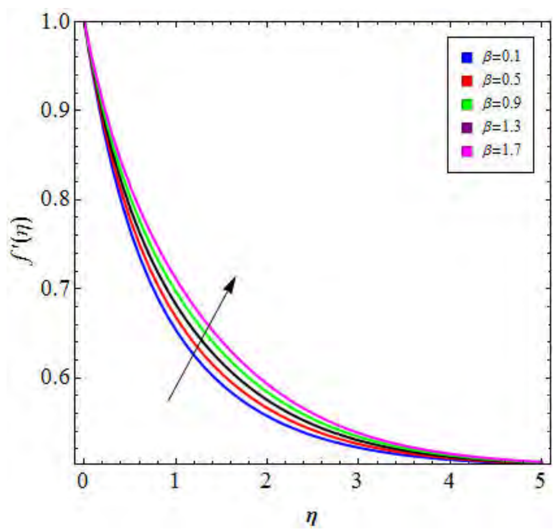

Fig. 7.3: $f'(\eta)$ for higher β.

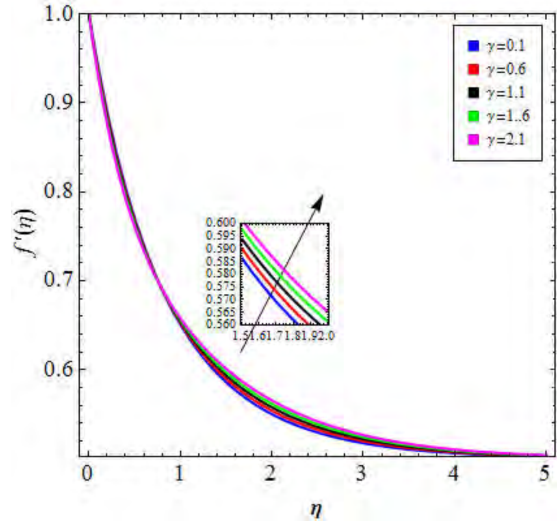

Fig. 7.4: $f'(\eta)$ for higher γ.

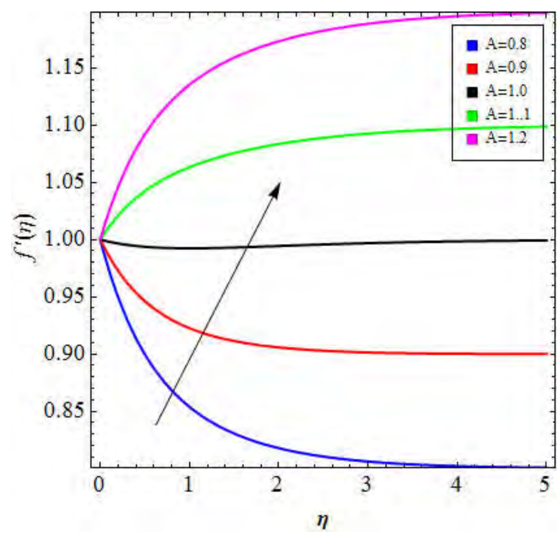

Fig. 7.5: $f'(\eta)$ for higher A.

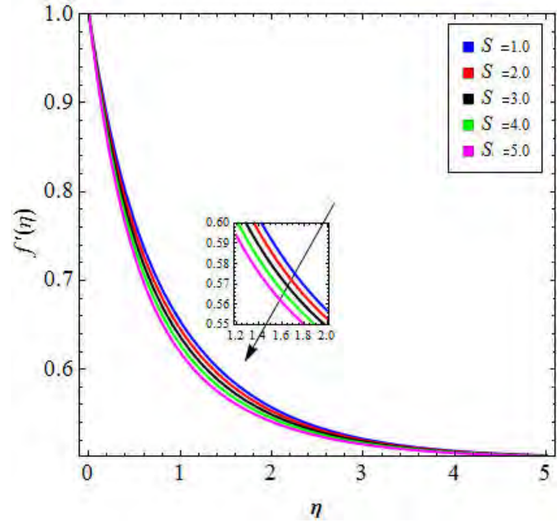

Fig. 7.6: $f'(\eta)$ for higher $S > 0$.

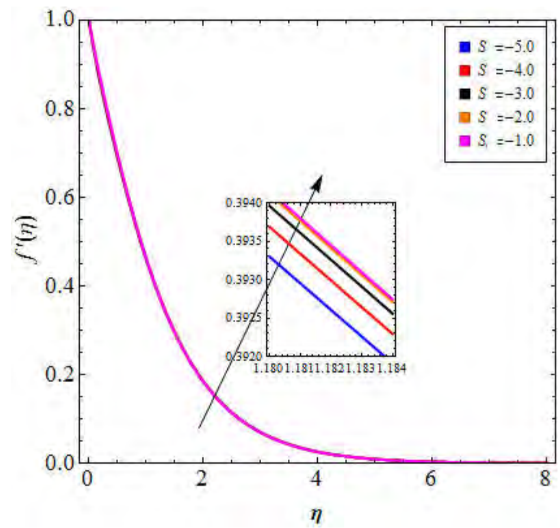

Fig. 7.7: $f'(\eta)$ for higher $S < 0$.

7.5.2 Temperature ($\theta(\eta)$)

Behavior of fluid temperature ($\theta(\eta)$) due to higher estimations of λ_2, β, γ, Pr, Ec, R^*, β_1, N_t and N_b is explored in this subsection Fig. 7.8 captured impact of λ_2 on $\theta(\eta)$. Clearly $\theta(\eta)$ rises with higher λ_2. As λ_2 is associated with higher viscosity or higher elasticity therefore more heat is generated due to dissipation and $\theta(\eta)$ enhances. Variation of $\theta(\eta)$ against β is shown in Fig. 7.9. Higher β cause reduction in $\theta(\eta)$. Fluid temperature ($\theta(\eta)$) against γ is plotted in Fig. 7.10. Increment in γ directly varies $\theta(\eta)$. In fact higher γ lead to small radius (R) of cylinder. Thus area of contact between nanofluid and cylindrical surface decreases and more heated particles join the cold nanofluid above the surface. Hence $\theta(\eta)$ intensifies. Effect of Pr on $\theta(\eta)$ is labeled in Fig. 7.11. $\theta(\eta)$ reduces with higher Pr. As Pr is ratio of momentum diffusivity (v_f) and thermal diffusivity (α_f). Higher Pr leads to small thermal diffusion and so $\theta(\eta)$ increases. Fluid temperature $(\theta(\eta))$ for Ec is examined in Fig. 7.12. Increment in Ec causes intensification of $\theta(\eta)$. Physically Ec is the ratio of K.E and enthalpy. Increase of Ec leads to increment in K.E and consequently $\theta(\eta)$ enhances. Fig. 7.13 displays influence of R^* on $\theta(\eta)$. Increment in R^* directly affects $\theta(\eta)$. Physically larger R^* is associated with increment in surface heat flux. Thus fluid becomes more worms and $\theta(\eta)$ rises. Fig. 7.14 demonstrate $\theta(\eta)$ via higher estimation of β_1. Higher β_1 is associated with increase in heat transfer coefficient. Here $\theta(\eta)$ enhances. Variation of fluid temperature $(\theta(\eta))$ against N_t and N_b is displayed in Figs. 7.15 and 7.16 respectively. Increase of both N_t and N_b intensifies $\theta(\eta)$. Higher N_t is responsible for more thermophoretic diffusion from heated cylinder towards cold fluid and so $\theta(\eta)$ increases. Larger N_b is associated with increase of Brownian motion which intensifies K.E of nanomaterial and so $\theta(\eta)$ intensifies.

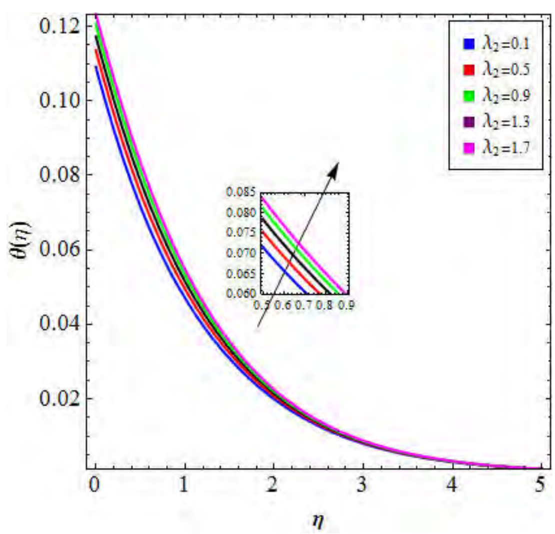

Fig. 7.8: $\theta(\eta)$ for higher λ_2.

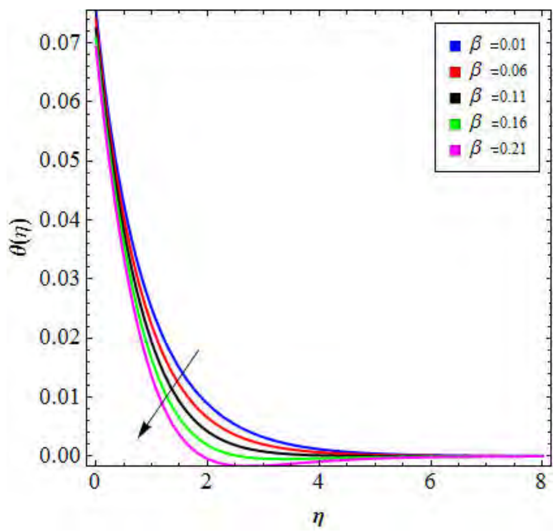

Fig. 7.9: $\theta(\eta)$ for higher β.

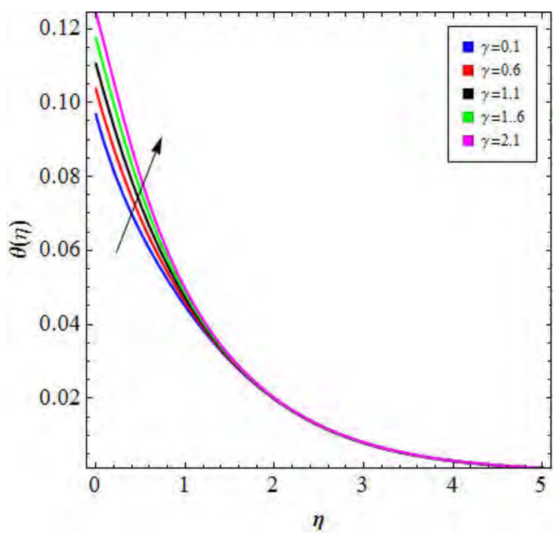

Fig. 7.10: $\theta(\eta)$ for higher γ.

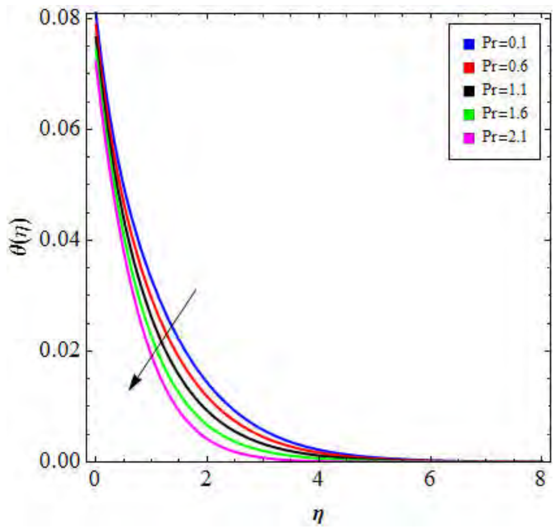

Fig. 7.11: $\theta(\eta)$ for higher Pr .

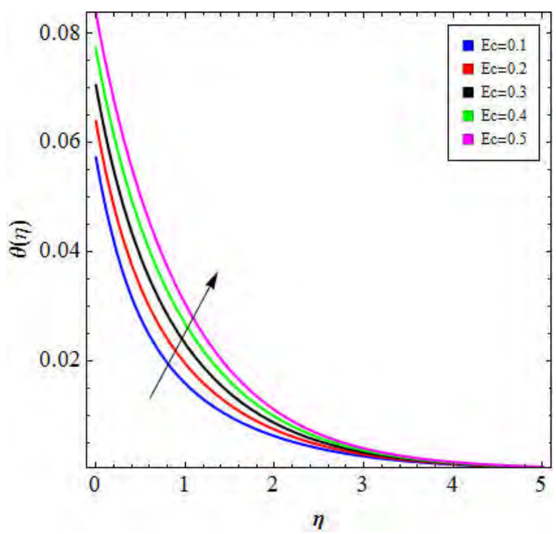

Fig. 7.12: $\theta(\eta)$ for higher Ec.

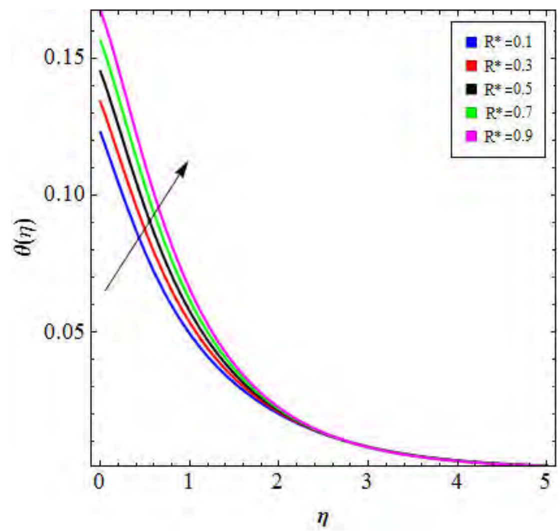

Fig. 7.13: $\theta(\eta)$ for higher R^*.

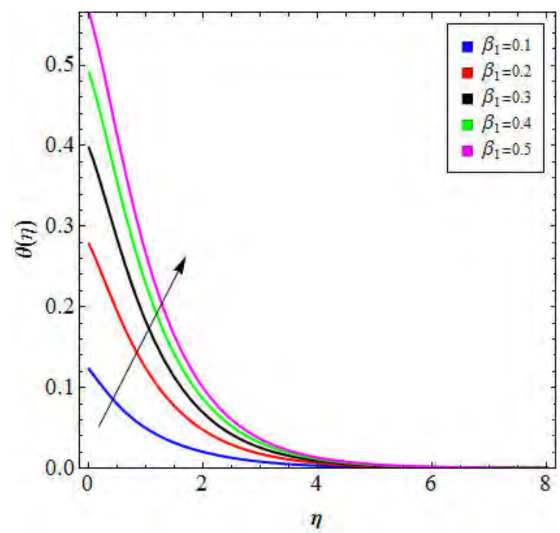

Fig. 7.14: $\theta(\eta)$ for higher β_1.

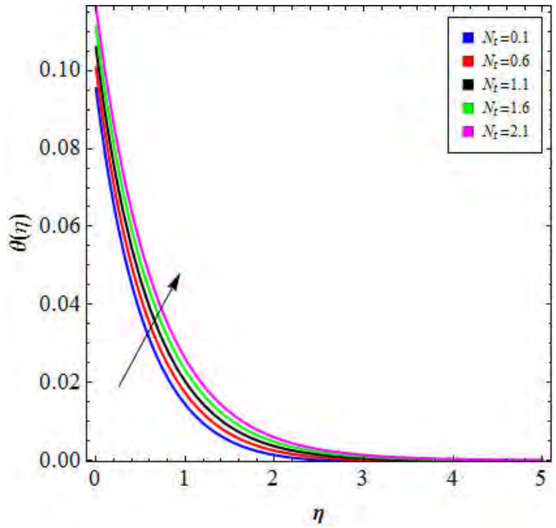

Fig. 7.15: $\theta(\eta)$ for higher N_t.

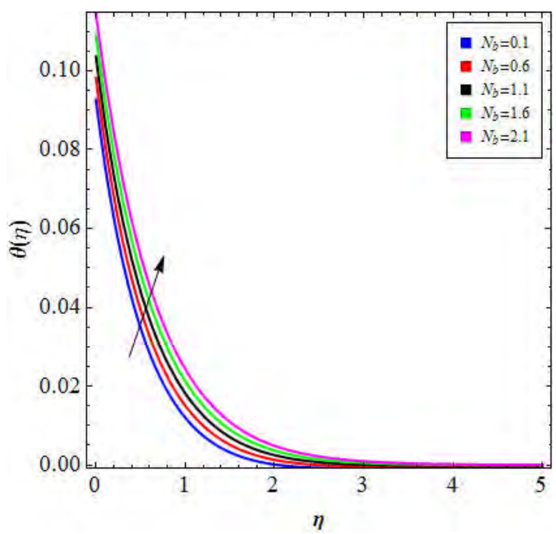

Fig. 7.16: $\theta(\eta)$ for higher N_b.

7.5.3 Concentration ($\phi(\eta)$)

This subsection is associated for impacts of N_b, N_t, β_2, E, Sc, δ, σ_1 and n on nanofluid concentration ($\phi(\eta)$). Fig. 7.17 captured the influence of N_b on $\phi(\eta)$. Decay in $\phi(\eta)$ is noticed for higher N_b. Further $\phi(\eta)$ via higher values of N_t is labeled in Fig. 7.18. Intensification of $\phi(\eta)$ is observed by larger N_t. Outcome of β_2 on nanofluid concentration ($\phi(\eta)$) is sketched in Fig. 7.19. Higher β_2 directly affect $\phi(\eta)$. An increase of β_2 give rise to more mass transfer coefficient and $\phi(\eta)$ enhances. Fig. 7.20 is sketched for influence of E on $\phi(\eta)$. Clearly $\phi(\eta)$

intensifies via E. Impact of Sc on $\phi(\eta)$ is shown in Fig. 7.21. Here $\phi(\eta)$ reduces with Sc. As Sc is ratio of momentum and mass diffusivity therefore higher Sc lead to small mass diffusivity and thus $\phi(\eta)$ decreases. Fig. 7.22 displayed $\phi(\eta)$ under impact of δ. Higher δ cause reduction in $\phi(\eta)$. Nanofluid concentration $\phi(\eta)$ against higher estimations of σ_1 and n is plotted in Figs. 7.23 and 7.24 respectively. Both σ_1 and n cause decay of $\phi(\eta)$.

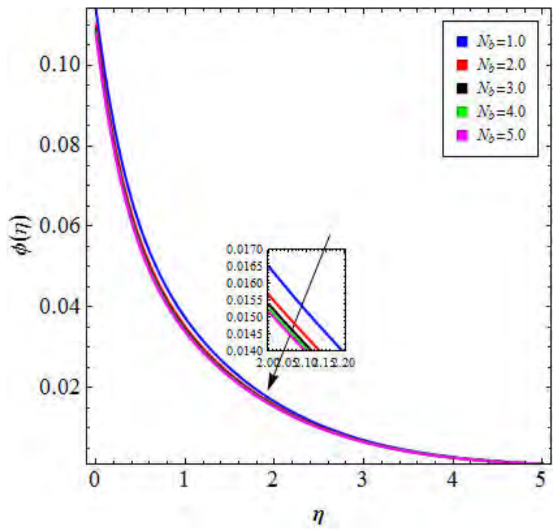

Fig. 7.17: $\phi(\eta)$ for higher N_b.

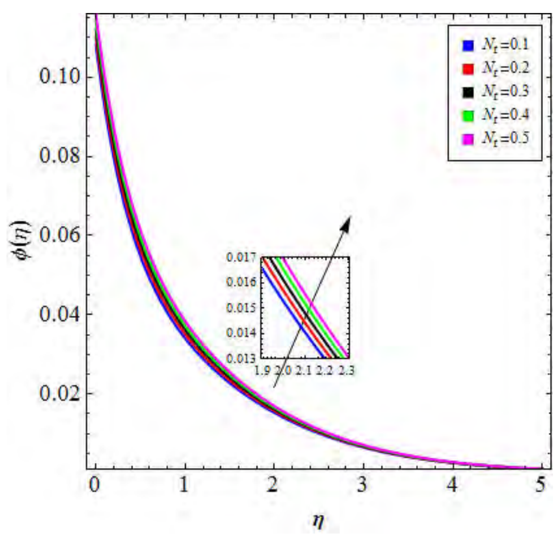

Fig. 7.18: $\phi(\eta)$ for higher N_t.

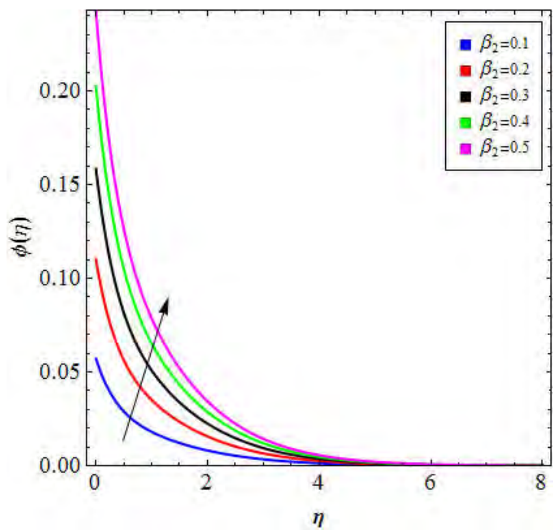

Fig. 7.19: $\phi(\eta)$ for higher β_2.

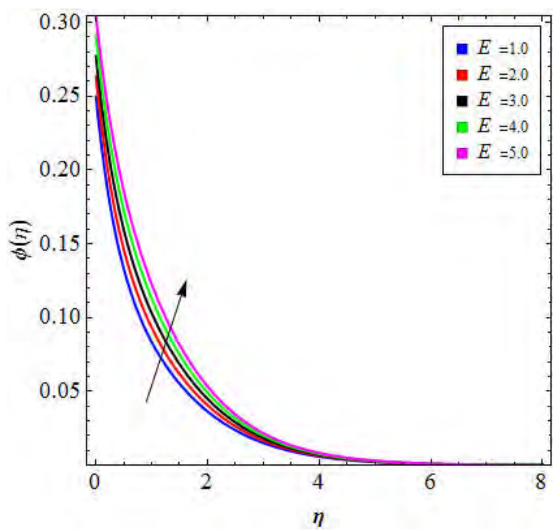

Fig. 7.20: $\phi(\eta)$ for higher E.

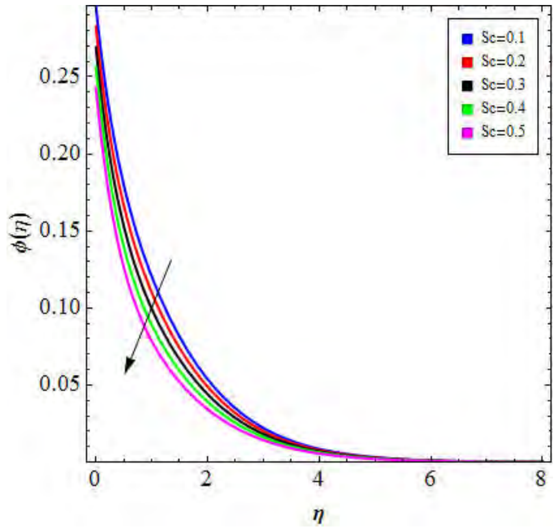

Fig. 7.21: $\phi(\eta)$ for higher Sc.

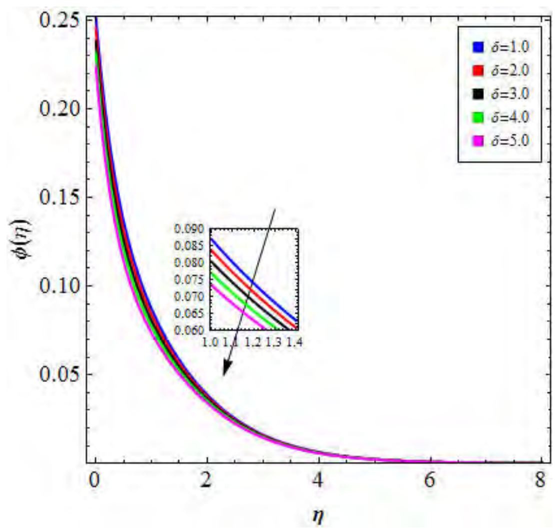

Fig. 7.22: $\phi(\eta)$ for higher δ.

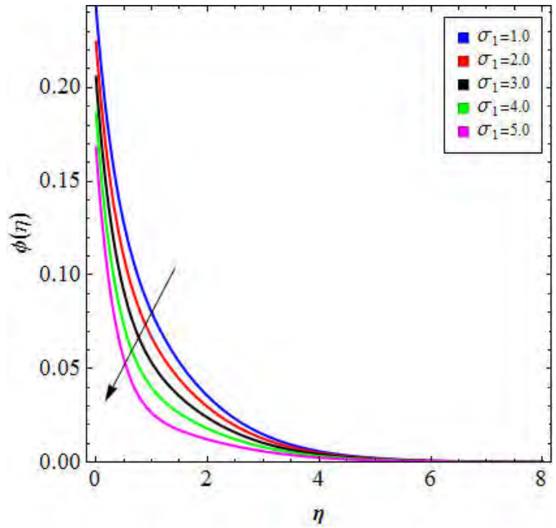

Fig. 7.23: $\phi(\eta)$ for higher σ_1.

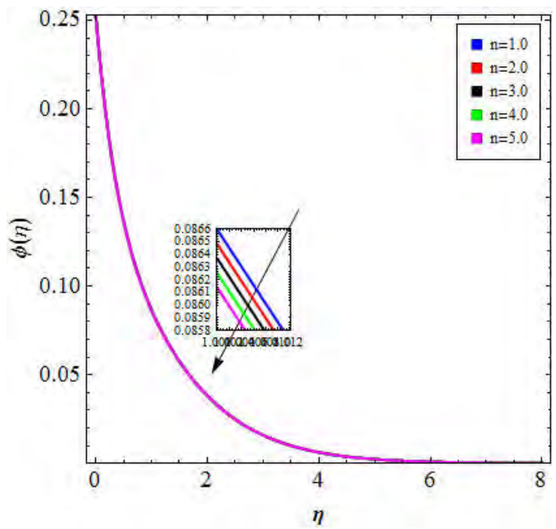

Fig. 7.24: $\phi(\eta)$ for higher n.

7.5.4 Skin friction $(C_f\sqrt{\mathrm{Re}})$, Sherwood number $(\frac{Sh_x}{\sqrt{\mathrm{Re}}})$ and Nusselt number $(\frac{Nu_x}{\sqrt{\mathrm{Re}}})$

Surface friction coefficient $(C_f\sqrt{\mathrm{Re}})$ under the influences of λ_2, β and γ is evaluated numerically in Table. 7.2. Sherwood number $(\frac{Sh_x}{\sqrt{\mathrm{Re}}})$ under N_b, N_t, β_2, Sc, E, σ_1 and Nusselt number $(\frac{Nu_x}{\sqrt{\mathrm{Re}}})$ for impacts of λ_2, β_3, γ, N_t, N_b, β_1, R^* and Pr are numerically evaluated in Tables. 7.3 and 7.4 respectively. Skin friction $(C_f\sqrt{\mathrm{Re}})$ increases with higher β and γ while reverse is noticed by higher λ_2. Sherwood number $(\frac{Sh_x}{\sqrt{\mathrm{Re}}})$ enhances with higher values of N_b, β_2, Sc, σ_1 while it reduces for N_t and E. Nusselt number $(\frac{Nu_x}{\sqrt{\text{Re}}})$ increases against β, γ, R^* and Pr while it decays through higher λ_2, N_t, N_b and β.

Table. 7.2: Evaluation of surface friction coefficient $(C_f\sqrt{\text{Re}})$ for λ_2, β and γ.

λ_2	β	γ	$-C_f\sqrt{\text{Re}}$
0.1	0.1	1.0	0.6894
0.2			0.6536
0.1	0.1	1.0	0.6895
	0.2		0.7079
0.1	0.1	1.0	0.6330
		2.0	0.6393

Table. 7.3: Evaluation of Sherwood number $(\frac{Sh_x}{\sqrt{\text{Re}}})$ for N_b, N_t, β_2, Sc, E and σ_1.

N_b	N_t	β_2	Sc	E	σ_1	$\frac{Sh_x}{\sqrt{\text{Re}}}$
0.1	0.1	0.1	0.2	0.1	0.1	0.09381
0.2						0.09412
0.1	0.1	0.1	0.2	0.1	0.1	0.09441
	0.2					0.09433
0.1	0.1	0.1	0.2	0.1	0.1	0.09440
		0.2				0.17840
0.1	0.1	0.1	0.1	0.1	0.1	0.35410
			0.2			0.36070
0.1	0.1	0.1	0.2	0.1	0.1	0.37700
				0.2		0.37020
0.1	0.1	0.1	0.2	0.1	0.1	0.37840
					0.2	0.38000

Table. 7.4: Evaluation of Nusselt number $(\frac{Nu_x}{\sqrt{\text{Re}}})$ for λ_2, β, γ, N_t, N_b, β_1, R^* and Pr.

λ_2	β	γ	N_t	N_b	β_1	R^*	Pr	$\frac{Nu_x}{\sqrt{\text{Re}}}$
0.1	0.1	1.0	0.2	0.2	0.2	0.1	2.0	0.10510
0.2								0.10560
0.1	0.1	1.0	0.2	0.2	0.2	0.1	2.0	0.10510
	0.2							0.10540
0.1	0.1	1.0	0.2	0.2	0.2	0.1	2.0	0.10370
		2.0						0.10380
0.1	0.1	1.0	0.1	0.2	0.2	0.1	2.0	0.10512
			0.2					0.10508
0.1	0.1	1.0	0.1	0.1	0.2	0.1	2.0	0.10519
				0.2				0.10512
0.1	0.1	1.0	0.1	0.2	0.1	0.1	2.0	0.10519
					0.2			0.10512
0.1	0.1	1.0	0.1	0.2	0.2	0.1	2.0	0.10510
						0.2		0.11760
0.1	0.1	1.0	0.1	0.2	0.2	0.1	1.0	0.11700
							1.5	0.11730

7.6 Conclusions

Key observations of presented chapter are mentioned below.

- Fluid velocity ($f'(\eta)$) can be reduced by higher λ_2, $S > 0$ and $S < 0$.
- $f'(\eta)$ grows rapidly through higher β, γ and A.
- Fluid temperature ($\theta(\eta)$) intensifies for λ_2, γ, Ec, R^*, β_1, N_t and N_b while it decays with β and Pr.
- Nanofluid concentration ($\phi(\eta)$) increases with higher N_t, β_2 and E while it decreases against N_b, Sc, δ, σ_1 and n.
- Surface friction coefficient ($C_f\sqrt{\text{Re}}$) is reduced via larger λ_2 while it enhances for β and γ.

- Sherwood number $\left(\frac{Sh_x}{\sqrt{\mathrm{Re}}}\right)$ enhances with N_b, β_2, Sc and σ_1.

- Nusselt number $\left(\frac{Nu_x}{\sqrt{\mathrm{Re}}}\right)$ intensifies through higher estimations of λ_2, β, γ, R^* and Pr.

Chapter 8

Mixed convective slip flow of hybrid nanofluid (MWCNTs+Cu+Water), nanofluid (MWCNTs+Water) and basefluid (Water): A comparative investigation

8.1 Introduction

In this chapter we have addressed comparative investigation of hybrid nanofluid (MWCNTs+Cu+Water), nanofluid (MWCNTs+Water) and basefluid (water). Flow is due to curved stretching sheet. Flow via slip boundary condition is examined. Heat transport with viscous dissipation, mixed convection and convective boundary condition is discussed. Transformation procedure is adopted for converting PDEs into ODEs. These non-linear coupled ODEs are solved via shooting method with RK-4 algorithms (bvp4c). Behaviors of involved parameters on flow, Nusselt number (heat transfer rate), temperature and skin friction coefficient are analyzed graphically. Velocity of fluid enhances with increment in nanoparticles volume fraction for multi-walled CNTs, nanoparticle volume fraction for Cu and mixed convection parameter while it reduced via higher estimations of velocity slip parameter. Temperature of the fluid varies directly with an increase in nanoparticles volume fraction for multi-walled CNTs, nanoparticle volume fraction for Cu, Eckert number and thermal Biot number. Skin friction coefficient is reduced via higher mixed convection and velocity slip parameters. Nusselt number intensifies with increment in nanoparticles volume fraction for multi-walled CNTs, nanoparticle volume fraction for Cu, Eckert and thermal Biot numbers. For comparative study amongst hybrid nanomaterial, nanomaterial and basefluid, efficient behavior is noted for hybrid nanomaterial.

8.2 Modeling

Consider flow of hybrid nanomaterial (MWCNTs+Cu+Water) due to a curved stretched surface. Flow is analyzed in presence of slip boundary condition. Heat transport characteristics are studied via viscous dissipation, mixed convection and convective boundary condition. Curvilinear coordinates (s, r) are taken. Further $s-$axis is taken along curved surface while $r-$axis is perpendicular to it (see Fig. 8.1).

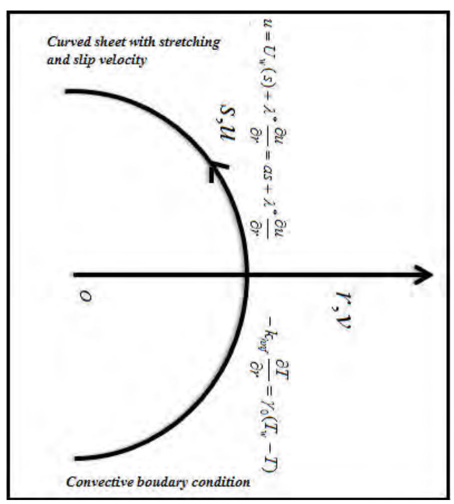

Fig. 8.1: Geometry for flow field.

Multiple-walled CNTs and Cu are taken as first and second nanoparticles in basefluid of water respectively for development of hybrid nanofluid (MWCNTs+Cu+Water). According to the mentioned assumptions and after implementation of boundary layer approximations the equations are

$$\frac{\partial}{\partial r}((r+R)v) + R\frac{\partial u}{\partial s} = 0, \tag{8.1}$$

$$\frac{1}{\rho_{hnf}}\frac{\partial p}{\partial r} = \frac{u^2}{r+R}, \tag{8.2}$$

$$v\frac{\partial u}{\partial r} + \frac{R}{r+R}u\frac{\partial u}{\partial s} + \frac{uv}{r+R} = -\frac{1}{\rho_{hnf}}\frac{R}{r+R}\frac{\partial p}{\partial s}$$

$$+v_{hnf}(\frac{\partial^2 u}{\partial r^2} + \frac{1}{r+R}\frac{\partial u}{\partial r} - \frac{u}{(r+R)^2}) + \frac{g(\beta\rho)_{hnf}}{\rho_{hnf}}(T-T_\infty), \tag{8.3}$$

$$v\frac{\partial T}{\partial r} + \frac{R}{r+R}u\frac{\partial T}{\partial s} = \frac{k_{hnf}}{(\rho c_p)_{hnf}}(\frac{\partial^2 T}{\partial r^2} + \frac{1}{r+R}\frac{\partial T}{\partial r}) + \frac{\mu_{hnf}}{(\rho c_p)_{hnf}}(\frac{\partial u}{\partial r} - \frac{1}{r+R}u)^2, \tag{8.4}$$

with

$$u = U_w(s) + \lambda^*\frac{\partial u}{\partial r} = U_0 s + \lambda^*\frac{\partial u}{\partial r}, \quad v = 0, \quad -k_{hnf}\frac{\partial T}{\partial r} = \gamma_0(T_w - T) \quad \text{at } r = 0,$$

$$u \to 0, \quad \frac{\partial u}{\partial r} \to 0, \quad T \to T_\infty \quad \text{as} \quad r \to \infty. \tag{8.5}$$

We choose the transformations

$$u = U_0 s f'(\eta), \quad v = -\frac{R}{r+R}\sqrt{U_0 v_f} f(\eta), \quad \eta = \sqrt{\frac{U_0}{v_f}}r,$$

$$\theta(\eta) = \frac{T-T_\infty}{T_w - T_\infty}, \quad p = \rho_f U_0^2 s^2 P(\eta). \tag{8.6}$$

Implementing these transformations, condition for incompressibility (8.1) is verified while other equations become

$$\frac{\partial P}{\partial \eta} = A_{11}\frac{f'^2}{\eta+\gamma}, \tag{8.7}$$

$$\frac{2\gamma}{\eta+\gamma}P = \frac{(1-\phi_1)^{2.5}(1-\phi_2)^{2.5}}{A_{11}}(\frac{\gamma}{\eta+\gamma}ff'' - \frac{\eta\gamma}{(\eta+\gamma)^2}f'^2 - \frac{\eta\gamma^2}{(\eta+\gamma)^2}f'^2 + \frac{\gamma}{(\eta+\gamma)^2}ff')$$

$$+\frac{f'}{(\eta+\gamma)^2} + \frac{1}{\eta+\gamma}f'' + f'''. \tag{8.8}$$

Eliminating P from Eqs. 9.7 and 9.8 we get

$$\frac{A_{11}}{(1-\phi_1)^{2.5}(1-\phi_2)^{2.5}}(f^{(iv)}+\frac{2}{\eta+\gamma}f'''-\frac{1}{(\eta+\gamma)^2}f''+\frac{1}{(\eta+\gamma)^3}f')+\frac{\gamma}{\eta+\gamma}ff'''+\frac{\gamma}{(\eta+\gamma)^2}ff''$$

$$-\frac{\gamma}{(\eta+\gamma)^3}ff'-\frac{\gamma}{(\eta+\gamma)^2}f'^2-\frac{\gamma}{\eta+\gamma}f'f''+\lambda_4 A_{22}(\theta'+\frac{1}{\eta+\gamma}\theta)=0, \tag{8.9}$$

$$\frac{\kappa_{hnf}}{\kappa_f}(\theta''+\frac{\theta'}{\eta+\gamma})+B_{11}\frac{\gamma}{\eta+\gamma}\Pr f\theta'+\frac{\Pr Ec}{(1-\phi_1)^{2.5}(1-\phi_2)^{2.5}}\frac{1}{(\eta+\gamma)^2}(f'+(\eta+\gamma)f'')^2=0, \tag{8.10}$$

$$f'(0)=1-\lambda_5 f''(0), \quad \theta'(0)=-\frac{\beta_1}{\frac{\kappa_{hnf}}{\kappa_f}}(1-\theta(0)), \quad f(0)=0,$$

$$f'\to 0, \quad \theta\to 0, \quad f''\to 0 \quad \text{as} \quad \eta\to\infty. \tag{8.11}$$

Here

$$A_{11}=\frac{1}{(1-\phi_2)\left((1-\phi_1)+\phi_1\frac{\rho_{m1}}{\rho_f}\right)+\phi_2\frac{\rho_{m2}}{\rho_f}}, \tag{8.12}$$

$$A_{22}=(1-\phi_2)\left((1-\phi_1)+\phi_1\frac{(\rho\beta)_{m1}}{(\rho\beta)_f}\right)+\phi_2\frac{(\rho\beta)_{m2}}{(\rho\beta)_f}, \tag{8.13}$$

$$B_{11}=(1-\phi_2)\left((1-\phi_1)+\phi_1\frac{(\rho c_p)_{m1}}{(\rho c_p)_f}\right)+\phi_2\frac{(\rho c_p)_{m2}}{(\rho c_p)_f}. \tag{8.14}$$

Involved physical parameters are

$$\lambda_5=\sqrt{\frac{U_0}{v_f}}\lambda^*, \quad \lambda_4=\frac{Gr}{\mathrm{Re}_s^2}, \quad Gr=\frac{g\beta_f(T_w-T_\infty)s^3}{v_f^2}, \quad \Pr=\frac{\nu_f}{\alpha_f},$$

$$Ec=\frac{(U_0 s)^2\rho_f}{(\rho c_p)_f(T_w-T_\infty)}, \quad \beta_1=\frac{\gamma_0}{k_f}\sqrt{\frac{v_f}{U_0}}, \quad \gamma=\sqrt{\frac{U_0}{v_f}}R. \tag{8.15}$$

8.2.1 Expressions for Skin friction coefficient ($C_f(\mathrm{Re})^{\frac{1}{2}}$) and Nusselt number ($Nu_s(\mathrm{Re})^{-\frac{1}{2}}$)

In dimensional form the ($C_f(\mathrm{Re})^{\frac{1}{2}}$) and ($Nu_s(\mathrm{Re})^{-\frac{1}{2}}$) are

$$C_{fs}=\frac{\tau_{ws}}{\rho_f U_w^2} \quad, Nu_s=\frac{sq_s}{k_f(T_f-T_\infty)}, \tag{8.16}$$

$$\text{with} \quad \tau_{ws} = \mu_{hnf}(\frac{\partial u}{\partial r} - \frac{1}{r+R}u)_{r=0}, \quad q_s = -k_{hnf}(\frac{\partial T}{\partial r}). \tag{8.17}$$

Implementation of transformations (8.6) leads to dimensionless form of above expression as:

$$C_{fs}\sqrt{\mathrm{Re}} = \frac{1}{(1-\phi_1)^{2.5}(1-\phi_2)^{2.5}}(f''(0) + \frac{1}{\gamma}f'(0)), \quad \frac{Nu_s}{\sqrt{\mathrm{Re}}} = -\frac{\kappa_{hnf}}{\kappa_f}\theta'(0), \tag{8.18}$$

where $\mathrm{Re} = \frac{U_w s}{v_f}$ is local Reynolds number.

8.3 Expressions for nanofluid (MWCNTs+Water) and Hybrid nanofluid (MWCNTs+Cu+Water) via Hamilton-Crosser model

For nanoflluid (MWCNTs+Water) [58]

$$\mu_{nf} = \frac{\mu_f}{(1-\phi_1)^{2.5}}, \quad v_{nf} = \frac{\mu_{nf}}{\rho_{nf}},$$

$$(\rho c_p)_{nf} = (1-\phi_1)(\rho c_p)_f + \phi_1(\rho c_p)_{m1},$$

$$\rho_{nf} = (1-\phi_1)\rho_f + \phi_1\rho_{m1},$$

$$\frac{\kappa_{nf}}{\kappa_f} = \frac{\kappa_{m1} + (n^*-1)\kappa_f - (n^*-1)\phi_1(\kappa_f - \kappa_{m1})}{\kappa_{m1} + (n^*-1)\kappa_f + \phi_1(\kappa_f - \kappa_{m1})}. \tag{8.19}$$

For hybrid nanofluid (SWCNTs+Cu+Water) we have [58]

$$\mu_{hnf} = \frac{\mu_f}{(1-\phi_1)^{2.5}(1-\phi_2)^{2.5}}, \quad v_{hnf} = \frac{\mu_{hnf}}{\rho_{hnf}},$$

$$(\rho c_p)_{hnf} = (1-\phi_2)((1-\phi_1)(\rho c_p)_f + \phi_1(\rho c_p)_{m1}) + \phi_2(\rho c_p)_{m2},$$

$$\rho_{hnf} = (1-\phi_2)\big((1-\phi_1)\rho_f + \phi_1\rho_{m1}\big) + \phi_2\rho_{m2},$$

$$\frac{\kappa_{hnf}}{\kappa_{bf}} = \frac{\kappa_{m2} + (n^*-1)\kappa_{bf} - (n^*-1)\phi_2(\kappa_{bf} - \kappa_{m2})}{\kappa_{m2} + (n^*-1)\kappa_{bf} + \phi_2(\kappa_{bf} - \kappa_{m2})},$$

$$\frac{\kappa_{nf}}{\kappa_f} = \frac{\kappa_{m1} + (n^*-1)\kappa_f - (n^*-1)\phi_1(\kappa_f - \kappa_{m1})}{\kappa_{m1} + (n^*-1)\kappa_f + \phi_1(\kappa_f - \kappa_{m1})}. \tag{8.20}$$

In above expressions $n^* = 6$ is taken for cylindrical shaped nanoparticles of both MWCNTs and Cu.

Table. 8.1: Thermal features of MWCNTs, Cu and water.

Nanoparticles\Thermophysical properties	$\rho(\frac{kg}{m^3})$	Pr	$c_p(\frac{J}{kgK})$	$\kappa(\frac{W}{mK})$
Cu	8933	-	385	400
MWCNTs	1600	-	796	3000
Water	997	6.7	4179	0.613

8.4 Methodology

The governing expressions after transmitting into ODEs via suitable transformations are solved through shooting technique (bvp4c). According to this method we convert the ODEs (momentum and energy equations) into system of first order ODEs. Thus we have

$$t_1 = f, \quad t_2 = t_1' = f', \quad t_3 = t_2' = f'', \quad t_4 = t_3' = f''', \tag{8.21}$$

$$t_5 = \theta, \quad t_6 = t_5' = \theta' \tag{8.22}$$

$$m^* = t_4' = f'''' = -(\frac{2}{\eta+\gamma}t_4 - \frac{1}{(\eta+\gamma)^2}t_3 + \frac{1}{(\eta+\gamma)^3}t_2) - \frac{(1-\phi_1)^{2.5}(1-\phi_2)^{2.5}}{A_{11}}(\frac{\gamma}{\eta+\gamma}t_1t_4 + \frac{\gamma}{(\eta+\gamma)^2}t_1t_3$$
$$-\frac{\gamma}{(\eta+\gamma)^3}t_1t_2 - \frac{\gamma}{(\eta+\gamma)^2}t_2^2 - \frac{\gamma}{\eta+\gamma}t_2t_3 + \lambda_4 A_{22}(t_6 + \frac{1}{\eta+\gamma}t_5)), \tag{8.23}$$

$$m^{**} = t_6' = \theta'' = \frac{1}{\frac{\kappa_{hnf}}{\kappa_f}}(B_{11}\Pr t_1 t_6 + \frac{\Pr Ec}{(1-\phi_1)^{2.5}(1-\phi_2)^{2.5}}\frac{1}{(\eta+\gamma)^2}(t_2 + (\eta+\gamma)t_3)^2) - \frac{t_6}{\eta+\gamma}, \tag{8.24}$$

$$t_2(0) = 1 - \lambda_5 t_3(0), \quad t_1(0) = 0, \quad f_6(0) = -\frac{\beta_1(1-t_5(0))}{\frac{k_{hnf}}{k_f}},$$

$$t_2 \to 0, \quad t_5 \to 0, \quad t_3 \to 0 \quad \text{as} \quad \eta \to \infty. \tag{8.25}$$

8.5 Analysis

Theme of this section is to visualize variations in temperature, flow, Nusselt number and skin friction coefficient for involved parameters. Note that for best results, values of ϕ_1 and ϕ_2 are adjusted in case of nanofluid (MWCNTs+Water) and hybrid nanofluid (MWCNTs+Cu+Water).

8.5.1 Variations in $f'(\eta)$(velocity)

Velocity under higher estimations of ϕ_1 is sketched in Fig. 8.2. Velocity ($f'(\eta)$) is an increasing function of ϕ_1. Also behavior of hybrid nanofluid (MWCNTs+Cu+water) dominates over nanofluid (MWCNTs+water). Impacts of ϕ_2 on $f'(\eta)$ are labeled in Fig. 8.3. Intensification in $f'(\eta)$ is seen for higher ϕ_2. As ϕ_2 is associated with only hybrid nanofluid (MWCNTs+Cu+water), so in case of nanofluid (MWCNTs+water) no impact of ϕ_2 on $f'(\eta)$ occur. $f'(\eta)$ under the variations in γ is portrayed in Fig. 8.4. Higher γ leads to enlargement in $f'(\eta)$. Physically higher γ is associated with increment in radius. Higher radius corresponds to increment in area of contact between fluid and surface. Thus due to no-slip condition, velocity of fluid enhances. Impacts of hybrid nanofluid (MWCNTs+Cu+water) are dominant when compared with nanofluid (MWCNTs+water). Variations in $f'(\eta)$ due to increment in λ_5 is visualized in Fig. 8.5. Higher λ_5 leads to decay in $f'(\eta)$. Further impacts of hybrid nanofluid (MWCNTs+Cu+water) are efficient. $f'(\eta)$ under higher estimations of λ_4 is sketched in Fig. 8.6. Higher λ_4 causes enhancement in $f'(\eta)$. Physically higher λ_4 corresponds to greater bouncy force, which enhances $f'(\eta)$. Comparative investigations among hybrid nanomaterial (MWCNTs+Cu+water), nanomaterial (MWCNTs+water) and basefluid (water) during the impact of ϕ_1, ϕ_2, γ, λ_5 and λ_4 on $f'(\eta)$ are visualized in Figs. 8.7-8.11 respectively. As consequence it is founded that better performance is show by hybrid nanofluid (MWCNTs+Cu+water) followed by nanofluid (MWCNTs+water) and basefluid (water) respectively.

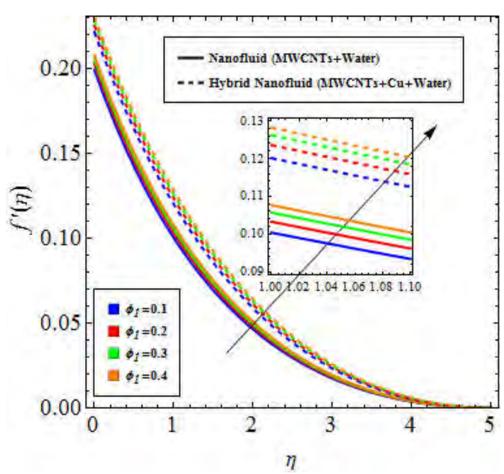

Fig. 8.2: $f'(\eta)$ for higher ϕ_1.

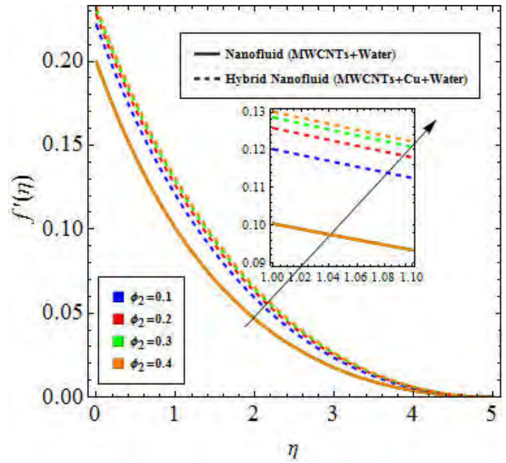

Fig. 8.3: $f'(\eta)$ for higher ϕ_2.

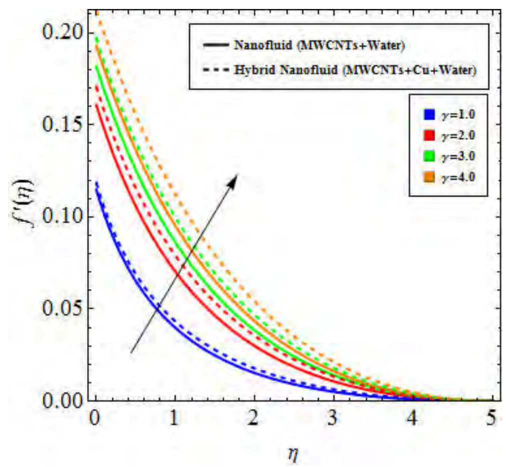

Fig. 8.4: $f'(\eta)$ for higher γ.

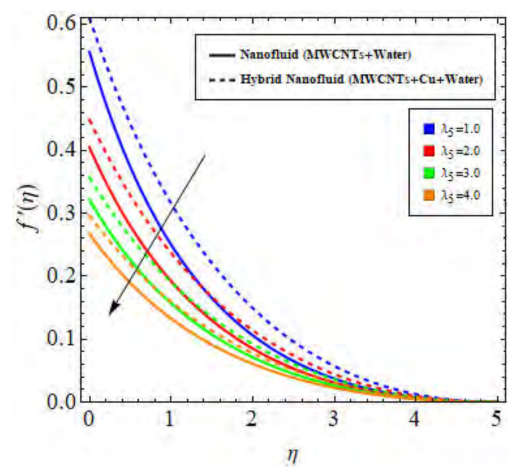

Fig. 8.5: $f'(\eta)$ for higher λ_5.

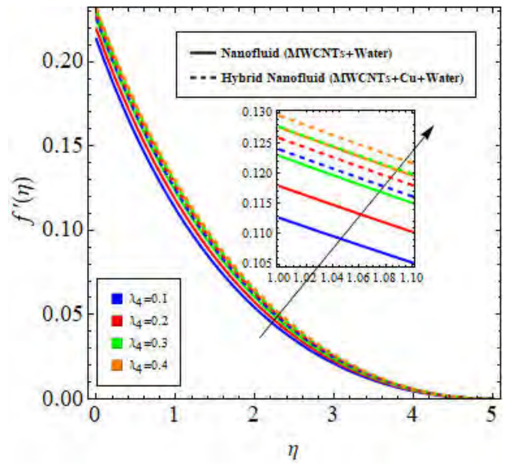

Fig. 8.6: $f'(\eta)$ for higher λ_4.

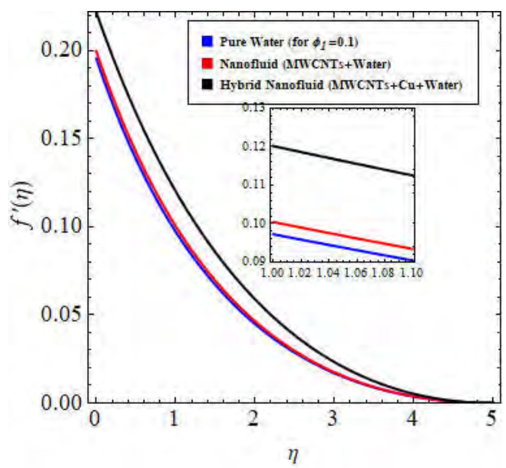

Fig. 8.7: Comparison of $f'(\eta)$ for higher ϕ_1.

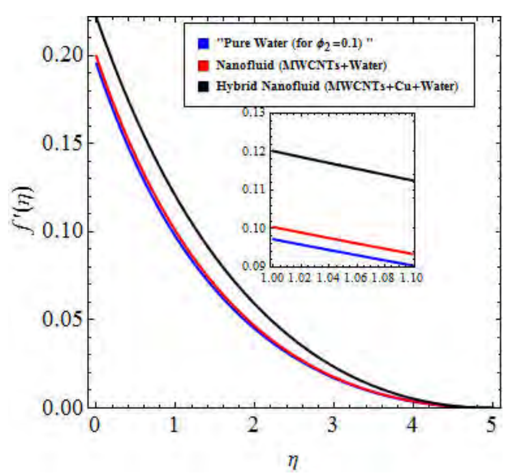

Fig. 8.8: Comparison of $f'(\eta)$ for higher ϕ_1.

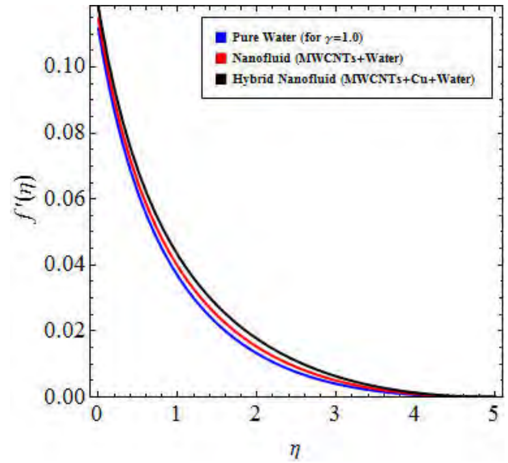

Fig. 8.9: Comparison of $f'(\eta)$ for higher γ.

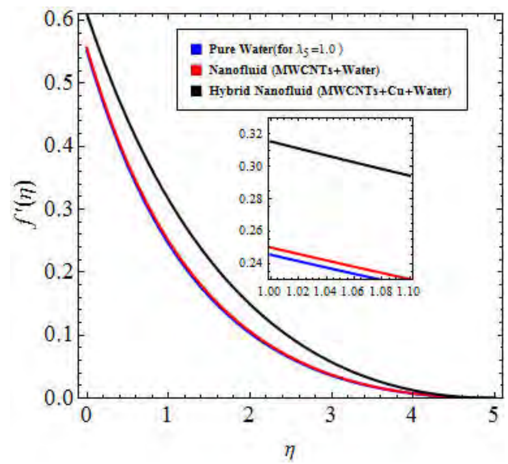

Fig. 8.10: Comparison of $f'(\eta)$ for higher λ_5.

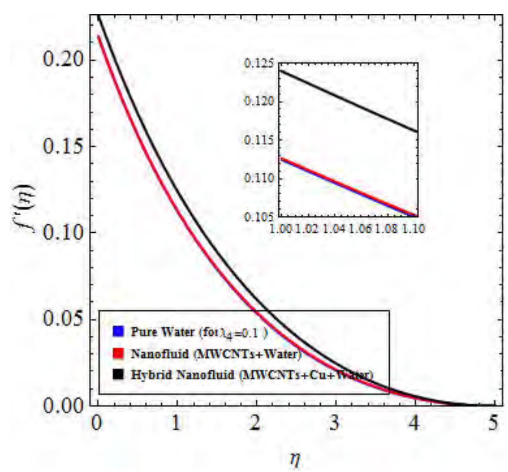

Fig. 8.11: Comparison of $f'(\eta)$ for higher λ_4.

8.5.2 Variations in $\theta(\eta)$ (temperature)

Fig. 8.12 is plotted for influence of ϕ_1 on $\theta(\eta)$. It is observed that higher ϕ_1 directly effect $\theta(\eta)$. Efficient behavior is observed for hybrid nanofluid (MWCNTs+Cu+water). $\theta(\eta)$ under the impacts of ϕ_2 is plotted in Fig. 8.13. Temperature ($\theta(\eta)$) directly varies with higher ϕ_2. Further as ϕ_2 is only associated with hybrid nanofluid (MWCNTs+Cu+water), so there is no impact of ϕ_2 on nanofluid (MWCNTs+Cu+water). Fig. 8.14 visualize impacts of Ec on $\theta(\eta)$. Intensification in $\theta(\eta)$ is examined via higher estimations of Ec. Basically Ec defines the ratio of K.E to the enthalpy, thus higher Ec leads to higher K.E. Hence $\theta(\eta)$ intensifies. Also hybrid nanofluid (MWCNTs+Cu+water) shows effective behavior. Impacts of β_1 on theta are presented in 8.15. Theta is directly impacted by β_1. Higher β_1 is associated with larger heat transfer coefficient. Hence $\theta(\eta)$ increases. Impact of hybrid nanofluid (MWCNTs+Cu+water) are prominent. Comparative investigation of basefluid (water), nanofluid (MWCNTs+water) and hybrid nanofluid (MWCNTs+Cu+water) during studying impacts of ϕ_1, ϕ_2, Ec and β_1 on $\theta(\eta)$ are visualized in Figs. 816-8.19 respectively. Efficient trend is shown by hybrid nanomaterial (MWCNTs+Cu+Water) which is followed by nanomaterial (MWCNTs+water) and basefluid (water).

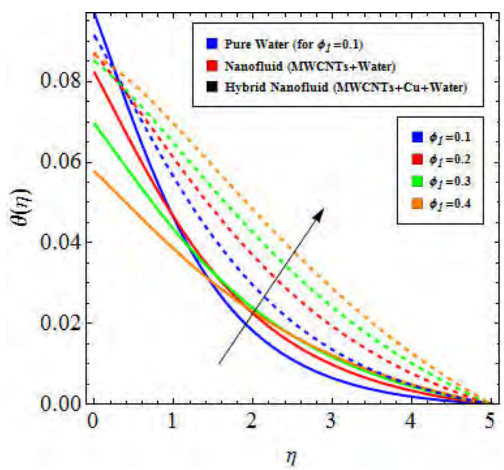

Fig. 8.12: $\theta(\eta)$ for higher ϕ_1.

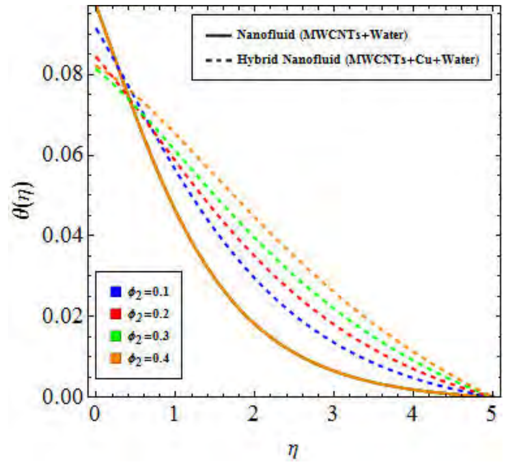

Fig. 8.13: $\theta(\eta)$ for higher ϕ_2.

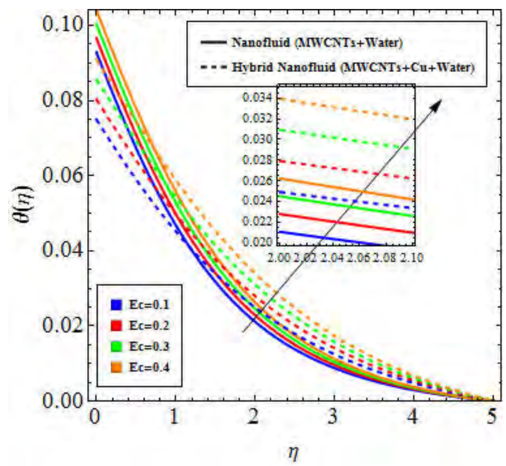

Fig. 8.14: $\theta(\eta)$ for higher Ec.

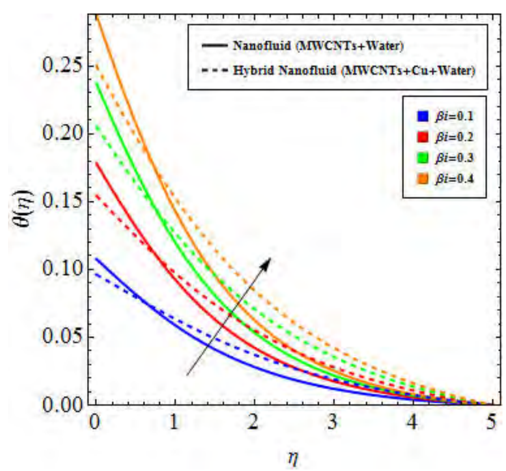

Fig. 8.15: $\theta(\eta)$ for higher β_1.

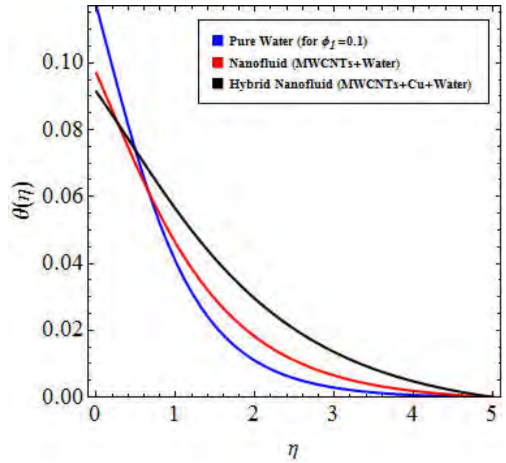

Fig. 8.16: Comparison during $\theta(\eta)$ for higher ϕ_1.

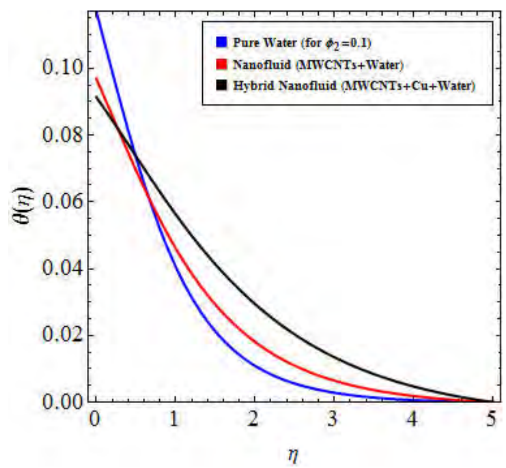

Fig. 8.17: Comparison during $\theta(\eta)$ for higher ϕ_2.

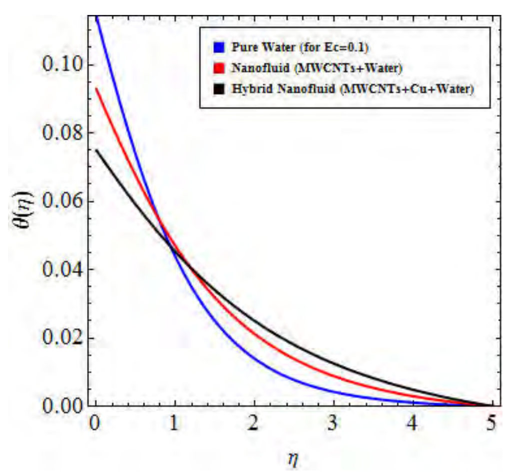

Fig. 8.18: Comparison during $\theta(\eta)$ for higher Ec.

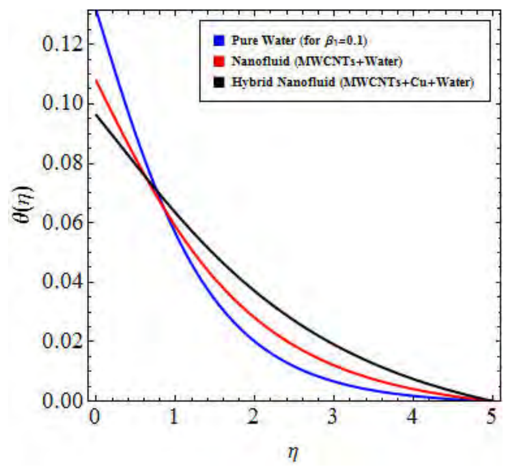

Fig. 8.19: Comparison during $\theta(\eta)$ for higher β_1.

8.5.3 Variations in C_f (skin friction coefficient) and Nu_s (Nusselt number)

C_f under the impacts of ϕ_1 and ϕ_2 is portrayed in Fig. 8.20. C_f directly varies with both ϕ_1 and ϕ_2. No impact of ϕ_2 on C_f is observed in case of nanomaterial (MWCNTs+Water). Impacts of hybrid nanomaterial (MWCNTs+Cu+Water) are more than nanomaterial (MWCNTs+water). Fig. 8.21 is labeled for variations in C_f through higher λ_4 and λ_5. Reduction in C_f is caused by both λ_1 and λ. Figs. 8.22 and 8.23 are plotted for comparison of hybrid nanofluid (MWCNTs+Cu+Water), nanofluid (MWCNTs+Water) and basefluid (water) during impacts of ϕ_1, ϕ_2 and λ_4, λ_5 on C_f. Effective behavior is observed for hybrid nanofluid (MWCNTs+Cu+Water) over nanofluid (MWCNTs+Water) and basefluid (water) respectively. Rate of heat transfer (Nu_s) under the impact of ϕ_1 and ϕ_2 is visualized in Fig. 8.24. Nu_s is enhanced by higher ϕ_1 and ϕ_2. Effective behavior is analyzed in case of hybrid nanofluid (MWCNTs+Cu+Water). Fig. 8.25 is plotted for variations in Nu_s via higher Ec and β_1. Intensification in Nu_s is examined for higher estimations of both Ec and β_1. Figs. 8.26 and 8.27 are sketched for comparative investigation among hybrid nanofluid (MWCNTs+Cu+water), nanofluid (MWCNTs+Water) and basefluid (water) during studying effects of ϕ_1, ϕ_2 and Ec, β_1 on Nu_s. As consequence it is found that efficient behavior is studied for hybrid nanomaterial (MWCNTs+Cu+Water) followed by nanomaterial (MWCNTs+Water) and basefluid (water) respectively.

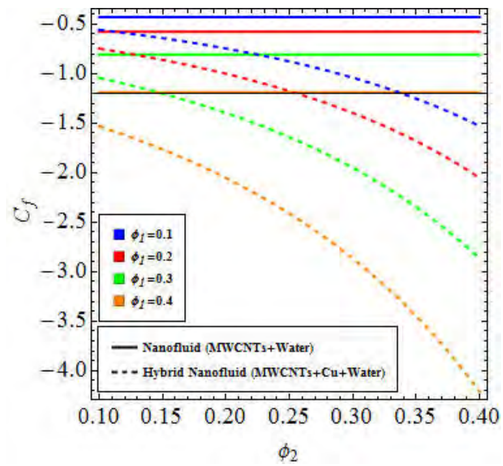

Fig. 8.20: C_f for higher ϕ_1 and ϕ_2.

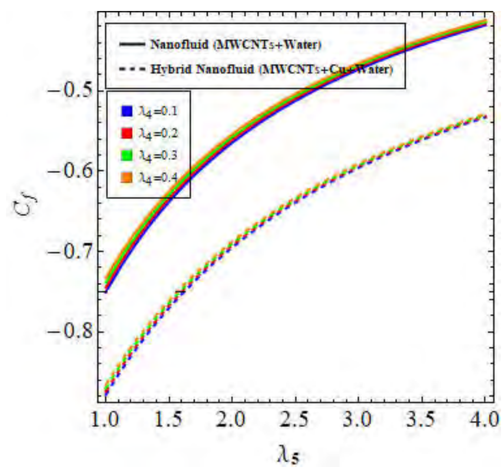

Fig. 8.21: C_f for higher λ_4 and λ_5.

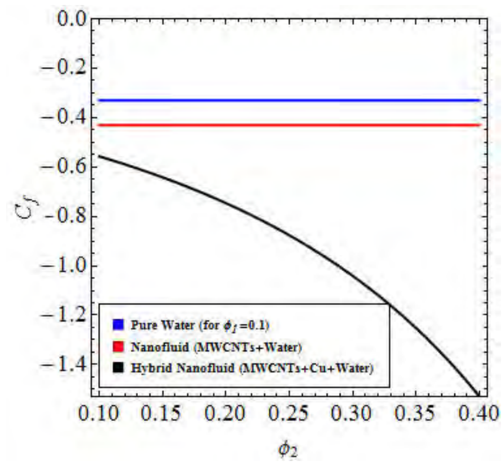

Fig. 8.22: Comparison of C_f for higher ϕ_1 and ϕ_2.

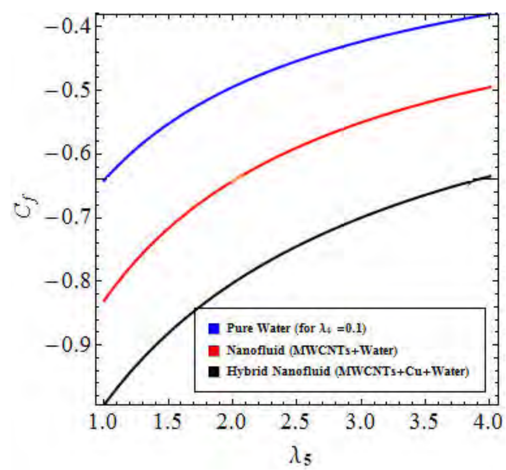

Fig. 8.23: Comparison of C_f for higher λ_4 and λ_5.

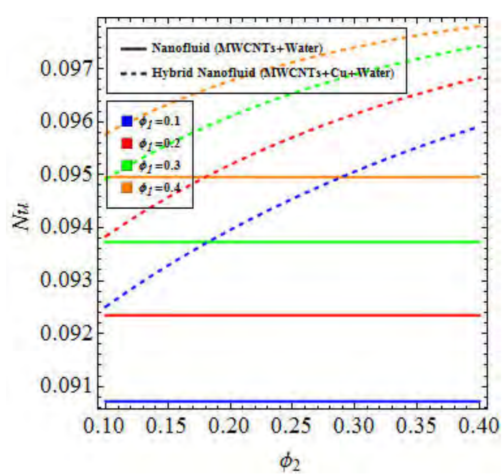

Fig. 8.24: Nu_x for higher ϕ_1 and ϕ_2.

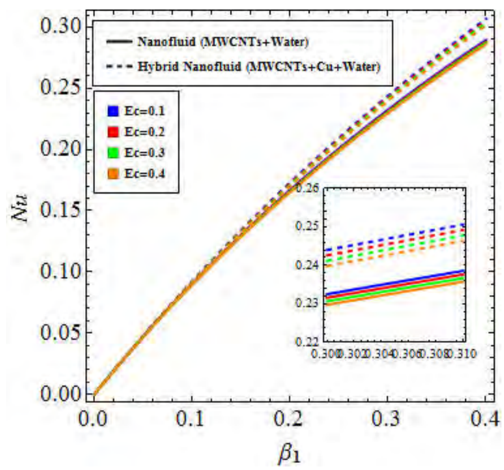

Fig. 8.25: Nu_x for higher Ec and β_1.

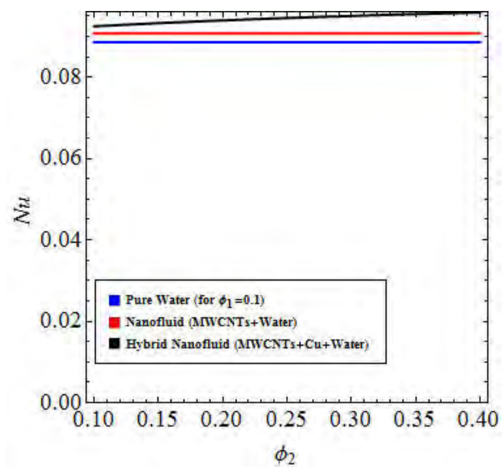

Fig. 8.26: Comparison of Nu_s for higher ϕ_1 and ϕ_2.

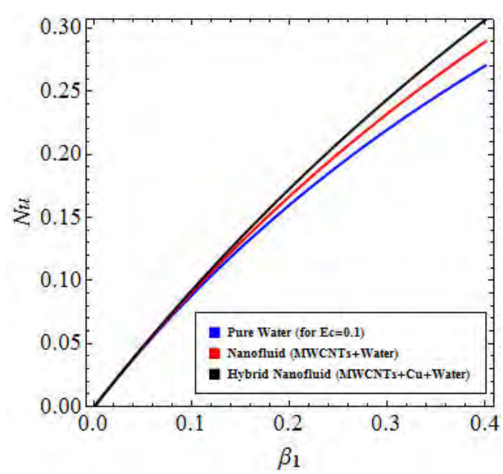

Fig. 8.27: Comparison of Nu_s for higher Ec and β_1.

8.6 Closing remarks

- Velocity of fluid is higher for larger ϕ_1, ϕ_2, γ and λ_4 while it reduces with higher λ_5.
- Temperature of fluid directly varies with higher estimations of ϕ_1, ϕ_2, Ec and β_1.
- Skin friction coefficient can be controlled with higher λ_4 and λ_5.
- Cooling process can be enhanced by higher estimations of ϕ_1, ϕ_2, Ec and β_1.
- During comparative analysis the efficient behavior is noted for hybrid nanomaterial

followed by nanomaterial and basefluid respectively.

Chapter 9

Numerical study for melting heat in dissipative flow of hybrid nanofluid over a variable thicked sheet

9.1 Introduction

This investigation is carried out to examine stagnation point flow of hybrid nanofluid (SWCNTs+Ag+Gasoline oil) towards a stretched sheet of variable thickness. The hybrid nanomaterials are acknowledged more suitable than ordinary nanoliquids. The idea is useful for enhancement of the properties of resultant nanomaterials better than the nanoliquids consisting of one nanoparticle. Viscous dissipation and melting effect are taken into consideration for heat transport characteristics. Adequate transformations are employed for reduction of PDEs (expressions) into ODEs. These ODEs are then converted into system of first order in order to solve by bvp4c (shooting method). Velocity, skin friction coefficient, Nusselt number and temperature are examined for influential parameters. Comparison of hybrid nanofluid (SWCNTs+Ag+Gasoline oil) with nanofluid (SWCNTs+Gasoline oil) and basefluid (Gasoline oil) is also presented graphically. Velocity of fluid enhances via rise in nanoparticle volume fraction for single-walled CNTs, nanoparticle volume fraction for Ag, velocity ratio and melting parameters. Reduction in temperature of fluid occurs with higher Eckert number, nanoparticle volume fraction for CNTs, nanoparticle volume fraction for Ag and melting parameter. Higher velocity ratio parameter controls the skin friction coefficient. Nusselt number rises with an increment in nanoparticle volume fraction for CNTs, velocity ratio parameter and nanoparticle volume fraction for Ag. Moreover during comparative study better performance is noticed for hybrid nanofluid (SWCNTs+Ag+Gasoline oil) over nanofluid (SWCNTs+Gasoline oil) than basefluid (Gasoline oil).

9.2 Mathematical Modeling

Assume steady dissipative flow of hybrid nanofluid (SWCNTs+Ag+Gasoline oil) over a stretched sheet having variable thickness. In Cartesian (x, y) coordinates sheet is stretched along x-axis with stretching velocity $U_w = U_0(x+b)^m$ and y-axis perpendicular to stretching sheet. Sheet thickness is taken as $y = B(x+b)^{\frac{1-m}{2}}$, which shows that the thickness of sheet varies with x-axis and is not of same size (see Fig. 9.1).

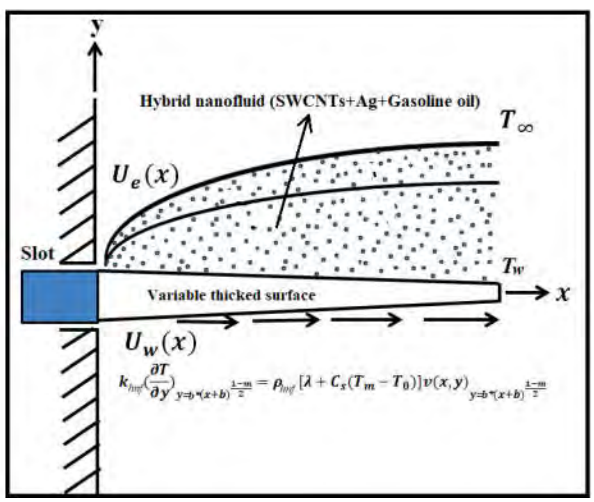

Fig. 9.1: Geometry for the flow field.

Melting effect describes heat transport features while flow is examined in stagnation-point region. After implementing mentioned assumptions and boundary layer approximations we get

$$\frac{\partial u}{\partial x} + \frac{\partial v}{\partial y} = 0, \tag{9.1}$$

$$u\frac{\partial u}{\partial x}+v\frac{\partial u}{\partial y}=U_e\frac{dU_e}{dx}+v_{hnf}\frac{\partial^2 u}{\partial y^2}, \tag{9.2}$$

$$u\frac{\partial T}{\partial x}+v\frac{\partial T}{\partial y}=\alpha_{hnf}\frac{\partial^2 T}{\partial y^2}+\frac{\mu_{hnf}}{(\rho c_p)_{hnf}}(\frac{\partial u}{\partial y})^2, \tag{9.3}$$

with

$$u=U_w\left(x\right)=U_0(x+b^*)^m,\quad v=0,\quad T=T_m,\quad \text{at}\quad y=B^*\left(x+b^*\right)^{\frac{1-m}{2}},$$

$$u\rightarrow U_e\left(x\right)=U_\infty\left(x+b^*\right)^m,\quad T\rightarrow T_\infty,\quad \text{as}\quad y\rightarrow\infty. \tag{9.4}$$

Melting heat condition is

$$k_{hnf}(\frac{\partial T}{\partial y})_{y=B^*(x+b^*)^{\frac{1-m}{2}}}=\rho_{hnf}\left[\lambda_1+c_s(T_m-T_0)\right]v_{y=B^*(x+b^*)^{\frac{1-m}{2}}}. \tag{9.5}$$

Consider the transformations

$$\xi=\sqrt{\frac{m+1}{2v_f}U_0\left(x+b^*\right)^{m-1}}y,\quad \psi=\sqrt{\frac{2v_f}{m+1}U_0\left(x+b^*\right)^{m+1}}F\left(\xi\right),\quad \Theta\left(\xi\right)=\frac{T-T_m}{T_\infty-T_m},$$

$$u=U_0\left(x+b^*\right)^m F'\left(\xi\right),\quad v=-\sqrt{\frac{(m+1)v_f}{2}U_0\left(x+b^*\right)^{m-1}}(F\left(\xi\right)+\xi F'(\xi)\frac{m-1}{m+1}). \tag{9.6}$$

We have

$$\frac{A_{11}}{(1-\phi_1)^{2.5}(1-\phi_2)^{2.5}}F'''+FF''-\frac{2m}{m+1}(F')^2+\frac{2m}{m+1}A^2=0, \tag{9.7}$$

$$\frac{k_{hnf}}{k_f}\Theta''+B_{11}\Pr F\Theta'+\frac{\Pr Ec}{(1-\phi_1)^{2.5}(1-\phi_2)^{2.5}}(F'')^2=0, \tag{9.8}$$

$$F'(\alpha)=1,\quad \Theta\left(\alpha\right)=0,\quad \frac{k_{hnf}}{k_f}M\Theta'\left(\alpha\right)+A_{11}(\Pr F\left(\alpha\right)+\frac{m-1}{m+1}\alpha)=0\quad \text{at}\quad \alpha=B^*\sqrt{\frac{m+1}{2v_f}U_0}$$

$$F'(\alpha)\rightarrow A,\quad \Theta\left(\alpha\right)\rightarrow 1\quad \text{as}\quad \alpha\rightarrow\infty. \tag{9.9}$$

In above expressions

$$A_{11}=\frac{1}{(1-\phi_2)\left((1-\phi_1)+\phi_1\frac{\rho_{m1}}{\rho_f}\right)+\phi_2\frac{\rho_{m2}}{\rho_f}}, \tag{9.10}$$

$$B_{11} = (1-\phi_2)\left((1-\phi_1) + \phi_1\frac{(\rho c_p)_{m1}}{(\rho c_p)_f}\right) + \phi_2\frac{(\rho c_p)_{m2}}{(\rho c_p)_f}, \tag{9.11}$$

and prime represents derivative w.r.t ξ and wall thickness is $\alpha = B^*\sqrt{\frac{m+1}{2v_f}U_0}$. Thus $\alpha = \xi = B^*\sqrt{\frac{m+1}{2v_f}U_0}$ gives flat surface. Here we define $F(\xi) = f(\xi-\alpha) = f(\eta)$, $\Theta(\xi) = \theta(\xi-\alpha) = \theta(\eta)$ and write

$$\frac{A_{11}}{(1-\phi_1)^{2.5}(1-\phi_2)^{2.5}}f''' + ff'' - \frac{2m}{m+1}(f')^2 + \frac{2m}{m+1}A^2 = 0, \tag{9.12}$$

$$\frac{k_{hnf}}{k_f}\theta'' + B_{11}\Pr f\theta' + \frac{\Pr Ec}{(1-\phi_1)^{2.5}(1-\phi_2)^{2.5}}(f'')^2 = 0, \tag{9.13}$$

$$f'(0) = 1, \quad \theta(0) = 0, \quad \frac{k_{hnf}}{k_f}M\theta'(0) + A_{11}(\Pr f(0) + \frac{m-1}{m+1}\alpha) = 0,$$
$$f'(\infty) \to A, \quad \theta(\infty) \to 1 \quad \text{when} \quad \eta \to \infty. \tag{9.14}$$

Associated parameters are

$$A = \frac{U_\infty}{U_0}, \quad \alpha = B^*\sqrt{\frac{m+1}{2v_f}U_0}, \quad M = \frac{c_p(T_\infty - T_m)}{\lambda_1 + c_s(T_m - T_0)}, \quad \Pr = \frac{\nu_f}{\alpha_f}, \quad Ec = \frac{(U_0x)^2\rho_f}{(\rho c_p)_f(T_\infty - T_m)}.$$

9.3 Expressions for skin friction coefficient (C_{fx}) and local Nusselt number (Nu_x)

Skin friction coefficient (C_{f_x}) and local Nusselt number (Nu_x) are

$$C_{fx} = \frac{\tau_w}{\rho_f U_w^2}, \tag{9.15}$$

$$\tau_{wx} = \mu_{hnf}(\frac{\partial u}{\partial y})_{y=B^*\sqrt{\frac{m+1}{2v_f}U_0}}, \tag{9.16}$$

and

$$Nu_x = \frac{(x+b^*)q_w}{k_f(T_\infty - T_m)}, \tag{9.17}$$

$$q_w = -k_{hnf}(\frac{\partial T}{\partial y})_{y=B\sqrt{\frac{m+1}{2v_f}U_0}}. \tag{9.18}$$

Substituting Eqs. 9.6, 9.16 and 9.18 in Eq. 9.15 and 9.18, we get dimensionless forms of C_{fx} and Nu_x as

$$C_{fx}\sqrt{\mathrm{Re}} = \frac{1}{(1-\phi_1)^{2.5}(1-\phi_2)^{2.5}}\sqrt{\frac{m+1}{2}}f''(0), \tag{9.19}$$

$$\frac{Nu_x}{\sqrt{\mathrm{Re}}} = -\frac{\kappa_{hnf}}{\kappa_f}\sqrt{\frac{m+1}{2}}\theta'(0), \tag{9.20}$$

with local Reynolds number defined by $\mathrm{Re} = \frac{U_0(x+b^*)}{\upsilon_f}$.

9.4 Expressions for nanofluid (SWCNTs+Gasoline oil) and hybrid nanofluid (SWCNTs+Ag+Gasoline oil) using Hamilton-Crosser model

For nanoflluid [58]

$$\mu_{nf} = \frac{\mu_f}{(1-\phi_1)^{2.5}}, \qquad \upsilon_{nf} = \frac{\mu_{nf}}{\rho_{nf}},$$

$$(\rho c_p)_{nf} = (1-\phi_1)(\rho c_p)_f + \phi_1(\rho c_p)_{m1},$$

$$\rho_{nf} = (1-\phi_1)\rho_f + \phi_1\rho_{m1},$$

$$\frac{\kappa_{nf}}{\kappa_f} = \frac{\kappa_{m1} + (n^*-1)\kappa_f - (n^*-1)\phi_1(\kappa_f - \kappa_{m1})}{\kappa_{m1} + (n^*-1)\kappa_f + \phi_1(\kappa_f - \kappa_{m1})}. \tag{9.21}$$

For hybrid nanofluid we have [58]

$$\mu_{hnf} = \frac{\mu_f}{(1-\phi_1)^{2.5}(1-\phi_2)^{2.5}}, \qquad \upsilon_{hnf} = \frac{\mu_{hnf}}{\rho_{hnf}},$$

$$(\rho c_p)_{hnf} = (1-\phi_2)((1-\phi_1)(\rho c_p)_f + \phi_1(\rho c_p)_{m1}) + \phi_2(\rho c_p)_{m2},$$

$$\rho_{hnf} = (1-\phi_2)\big((1-\phi_1)\rho_f + \phi_1\rho_{m1}\big) + \phi_2\rho_{m2},$$

$$\frac{\kappa_{hnf}}{\kappa_{bf}} = \frac{\kappa_{m2} + (n^*-1)\kappa_{bf} - (n^*-1)\phi_2(\kappa_{bf} - \kappa_{m2})}{\kappa_{m2} + (n^*-1)\kappa_{bf} + \phi_2(\kappa_{bf} - \kappa_{m2})},$$

$$\frac{\kappa_{nf}}{\kappa_f} = \frac{\kappa_{m1} + (n^*-1)\kappa_f - (n^*-1)\phi_1(\kappa_f - \kappa_{m1})}{\kappa_{m1} + (n^*-1)\kappa_f + \phi_1(\kappa_f - \kappa_{m1})}. \tag{9.22}$$

In aforementioned expressions both for nanofluid and hybrid nanofluid we have taken $n^* = 6$ due to consideration of cylindrical shaped nanoparticles.

Table. 9.1: Thermal characteristics of SWCNTs, Ag and Gasoline oil [58].

Nanoparticles\Thermophysical properties	$\rho(\frac{kg}{m^3})$	Pr	$c_p(\frac{J}{kgK})$	$\kappa(\frac{W}{mK})$
Ag	10490	-	235	429
SWCNTs	1600	-	796	3000
Gasoline oil	750	9.4	425	0.144

9.5 Solution methodology

Bvp4c (shooting method) is employed in order to develop solutions of governed expressions (ODEs). Bvp4c is implemented for first order differential equations. Thus we adopt the below procedure

$$f_1 = f, \quad f_2 = f_1' = f', \quad f_3 = f_2' = f'', \tag{9.23}$$

$$f_5 = \theta, \quad f_6 = f_5' = \theta' \tag{9.24}$$

$$f_4 = f_3' = f'''' = -\frac{(1-\phi_1)^{2.5}(1-\phi_2)^{2.5}}{A_{11}}(f_1 f_3 - \frac{2m}{m+1}(f_2)^2 + \frac{2m}{m+1}A^2) \tag{9.25}$$

$$f_6 = f_5' = \theta'' = \frac{-1}{\frac{\kappa_{hnf}}{\kappa_f}}(B_{11} \Pr f_1 f_6 + \frac{\Pr Ec}{(1-\phi_1)^{2.5}(1-\phi_2)^{2.5}}(f_3)^2), \tag{9.26}$$

$$f_2(0) = 1, \quad f_5(0) = 0, \quad \frac{k_{hnf}}{k_f} M f_6(0) + A_{11}(\Pr f_1(0) + \frac{m-1}{m+1}\alpha) = 0,$$

$$f_2(\eta) \to A, \quad f_5(\eta) \to 1 \quad \text{as} \quad \eta \to \infty.$$

9.6 Analysis

We have analyzed the effects of influential variables on surface friction coefficient, velocity, temperature and local Nusselt number graphically in this section. Comparative analysis of hybrid nanofluid (SWCNTs+Ag+Gasoline oil) with nanofluid (SWCNTs+Gasoline oil) and basefluid (Gasoline oil) is also performed. It is remarked that during comparative study for basefluid (Gasoline oil) $\phi_1 = \phi_2 = 0.0$ and values of ϕ_1 and ϕ_2 are adjusted for hybrid nanofluid (SWCNTs+Ag+Gasoline oil) while $\phi_2 = 0.0$ for nanofluid (SWCNTs+Gasoline oil).

9.6.1 Impacts of influential parameters on $f'(\eta)$ (velocity)

Fig. 9.2 delineates the effects of $\phi_1\epsilon[0.1, 0.4]$ on $f'(\eta)$. $f'(\eta)$ exhibits increasing trend via higher ϕ_1. Impacts for hybrid nanofluid (SWCNTs+Ag+Gasoline oil) are more than nanofluid (SWCNTs+Gasoline oil). Effects of $\phi_2\epsilon[0.1, 0.4]$ on $f'(\eta)$ are delineated in Fig. 9.3. Higher ϕ_2 cause intensification in $f'(\eta)$. Hybrid nanofluid (SWCNTs+Ag+Gasoline oil) impacts are efficient and also nanofluid (SWCNTs+Gasoline oil) remains invariant through ϕ_2 due to its correspondence with hybrid nanofluid (SWCNTs+Ag+Gasoline oil) only. Fig. 9.4 portrays the variations of $f'(\eta)$ due to higher $M\epsilon[0.1, 0.4]$. Here $f'(\eta)$ varies directly with M. Impacts of M for hybrid nanofluid (SWCNTs+Ag+Gasoline oil) are more when compared with nanofluid (SWCNTs+Gasoline oil). Fig. 9.5 is sketched for influences of $A\epsilon[0.8, 1.2]$ on $f'(\eta)$. Clearly $f'(\eta)$ enhances against higher A. It is also noticed that $A = 1.0$ reveals no formation of boundary layer while $A > 1$ and $A < 1$ correspond to boundary layer thinning and thickening respectively. Fig. 9.6 displays the variations in $f'(\eta)$ via increase of $\alpha\epsilon[1.0, 4.0]$. Decay in $f'(\eta)$ in examined via higher α. Influence of α during hybrid nanofluid (SWCNTs+Ag+Gasoline oil) is more when compared with nanofluid (SWCNTs+Gasoline oil). $f'(\eta)$ under higher values of $m\epsilon[0.1, 0.4]$ is plotted in Fig. 9.7. $f'(\eta)$ in this sketch reduces with increment in m ($m < 1$) due to enlargement of wall thickness. Impacts of m on hybrid nanofluid (SWCNTs+Ag+Gasoline oil) are more than nanofluid (SWCNTs+Gasoline oil). Figs. 9.8-9.13 are constructed for performing comparative investigation of hybrid nanofluid (SWCNTs+Ag+Gasoline oil) with nanofluid (SWCNTs+Gasoline oil) and basefluid (Gasoline oil) during examining influences of ϕ_1, ϕ_2, M, A, α and m on $f'(\eta)$. It is noticed that best performance is illustrated by hybrid nanofluid (SWCNTs+Ag+Gasoline oil) proceeded by nanofluid (SWCNTs+Gasoline oil) and baseliquid

(Gasoline oil) respectively.

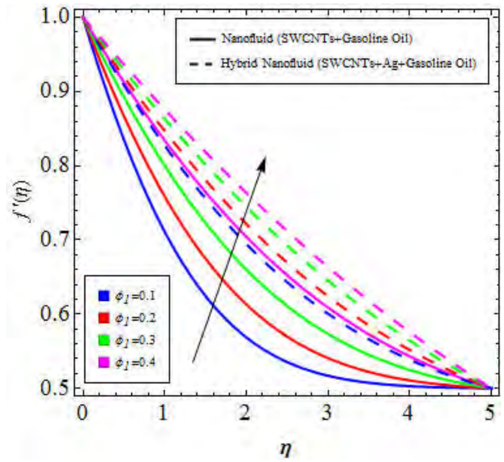

Fig. 9.2: $f'(\eta)$ for higher ϕ_1.

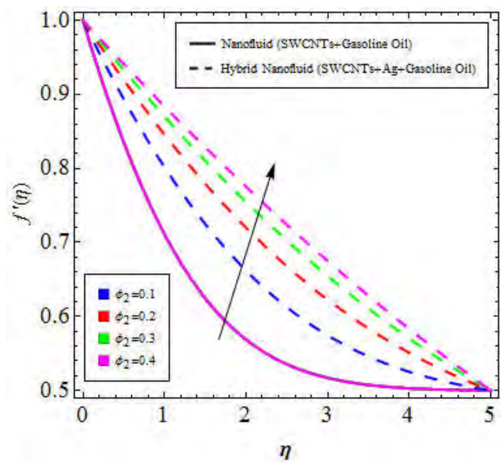

Fig. 9.3: $f'(\eta)$ for higher ϕ_2.

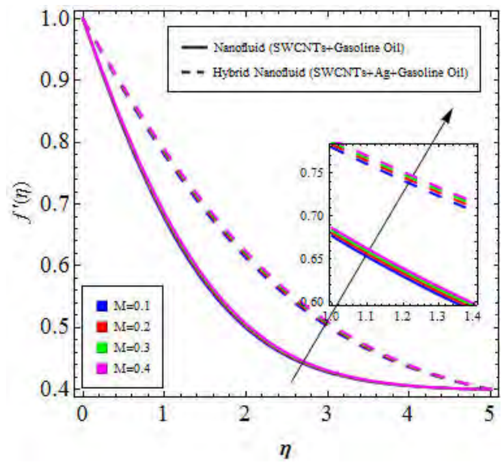

Fig. 9.4: $f'(\eta)$ for higher M.

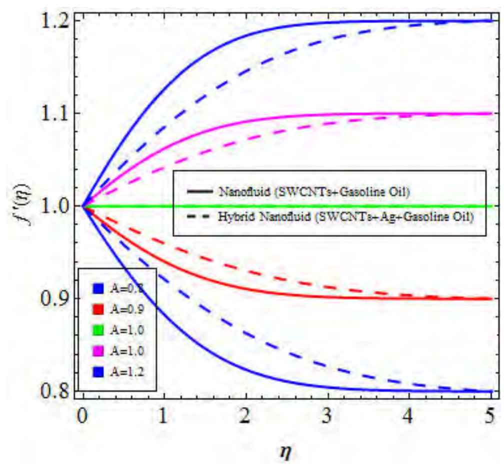

Fig. 9.5: $f'(\eta)$ for higher A.

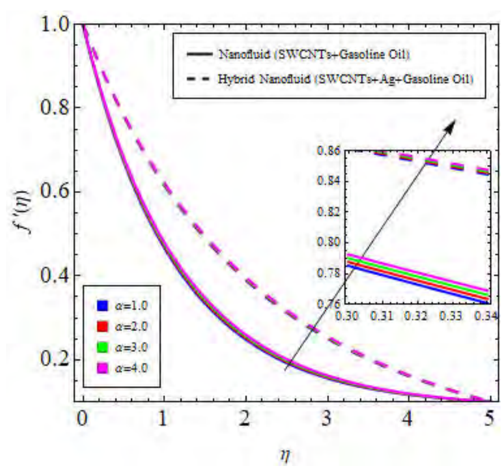

Fig. 9.6: $f'(\eta)$ for higher α.

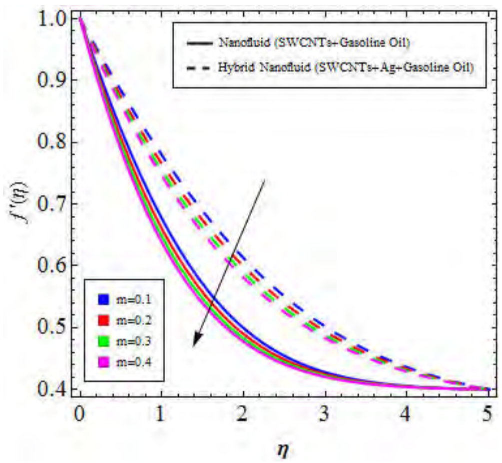

Fig. 9.7: $f'(\eta)$ for higher m.

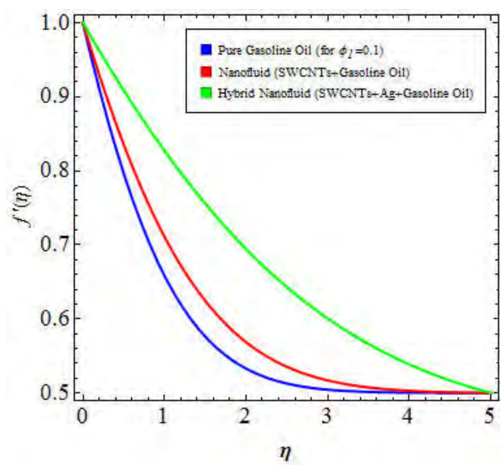

Fig. 9.8: Comparison of $f'(\eta)$ for higher ϕ_1.

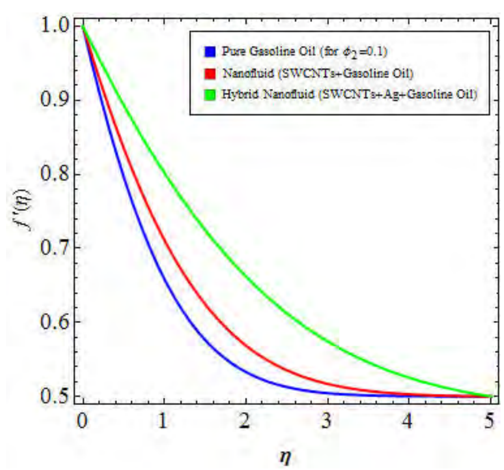

Fig. 9.9: Comparison of $f'(\eta)$ for higher ϕ_2.

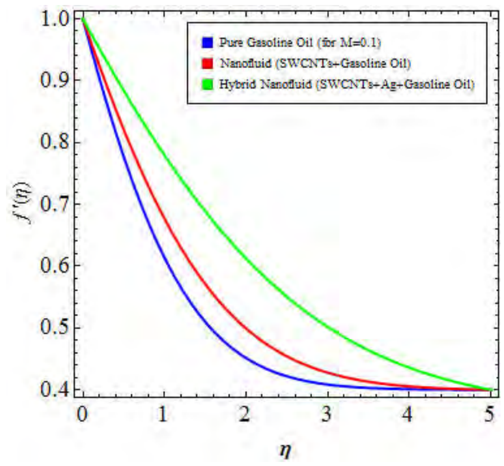

Fig. 9.10: Comparison of $f'(\eta)$ for higher M.

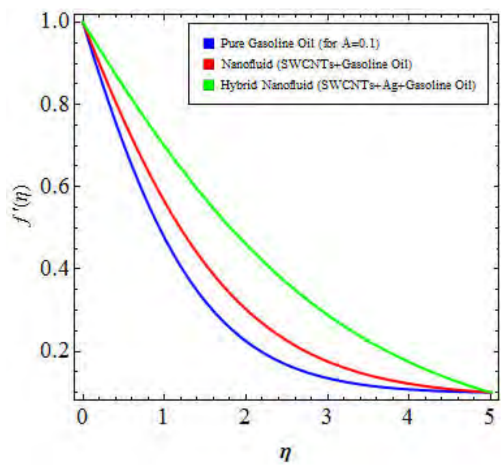

Fig. 9.11: Comparison of $f'(\eta)$ for higher A.

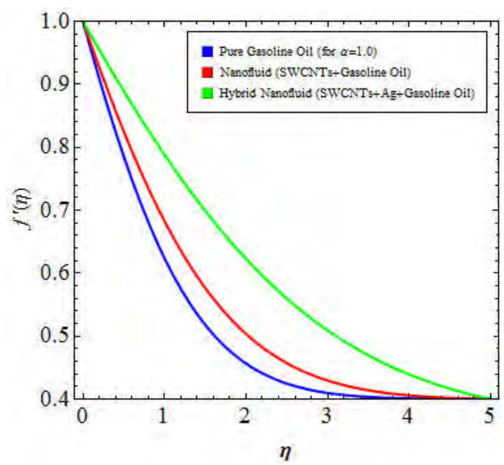

Fig. 9.12: Comparison of $f'(\eta)$ for higher α.

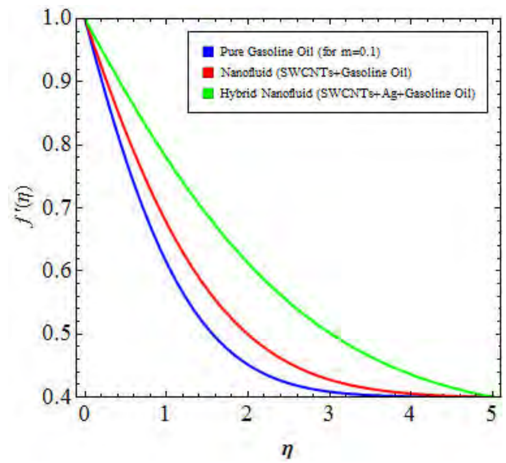

Fig. 9.13: Comparison of $f'(\eta)$ for higher m.

9.6.2 Impacts of influential parameters on $\theta(\eta)$ (temperature)

Fig. 9.14 is plotted for analyzing $\theta(\eta)$ under values of $\phi_1 \epsilon [0.1, 0.4]$. Higher ϕ_1 causes decay in $\theta(\eta)$. Impacts of hybrid nanofluid (SWCNTs+Ag+Gasoline oil) are prominent than nanofluid (SWCNTs+Gasoline oil). Temperature ($\theta(\eta)$) via increment in $\phi_2 \epsilon [0.1, 0.4]$ is plotted in Fig. 9.15. Temperature varies inversely with ϕ_2 and no impact of ϕ_2 is seen on $\theta(\eta)$ during nanofluid (SWCNTs+Gasoline oil) due to no correspondence with nanofluid (SWCNTs+Gasoline oil). Fig. 9.16 is labeled for examining variations in $\theta(\eta)$ due to increase in values of $M \epsilon [0.1, 0.4]$. Reduction in $\theta(\eta)$ is observed via M. Physically an increment in M corresponds to addition of cold fluid particles from melting sheet into the hot fluid. Thus $\theta(\eta)$ reduces and behavior of hybrid nanofluid (SWCNTs+Ag+Gasoline oil) is efficient as compared to nanofluid (SWCNTs+Gasoline oil). Influences of $Ec \epsilon [0.1, 0.4]$ on $\theta(\eta)$ is sketched in Fig. 9.17. $\theta(\eta)$ intensifies with higher Ec as increment in Ec corresponds to more K.E. Figs. 9.18-9.21 are plotted to make a comparison among hybrid nanofluid (SWCNTs+Ag+Gasoline oil), basefluid (Gasoline oil) and nanofluid (SWCNTs+Gasoline oil) for analysis $\theta(\eta)$ subject to ϕ_1, M, ϕ_2 and Ec. It can be seen precisely that impacts of hybrid nanofluid (SWCNTs+Ag+Gasoline oil) are more and are proceeded by nanofluid (SWCNTs+Gasoline oil) and baseliquid (Gasoline oil) respectively.

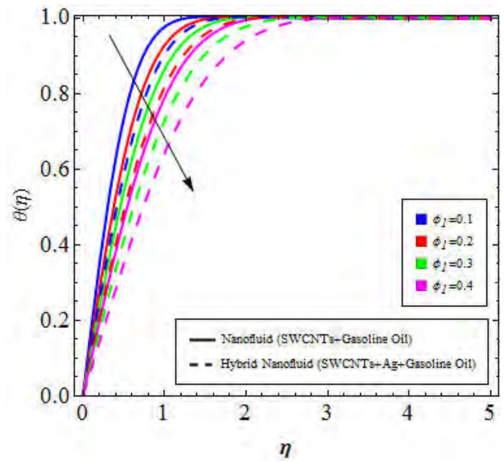

Fig. 9.14: $\theta(\eta)$ for higher ϕ_1.

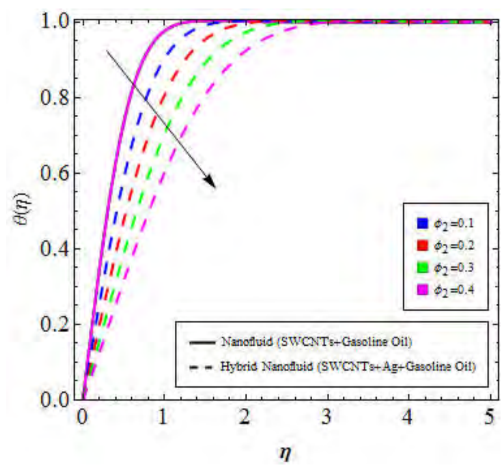

Fig. 9.15: $\theta(\eta)$ for higher ϕ_2.

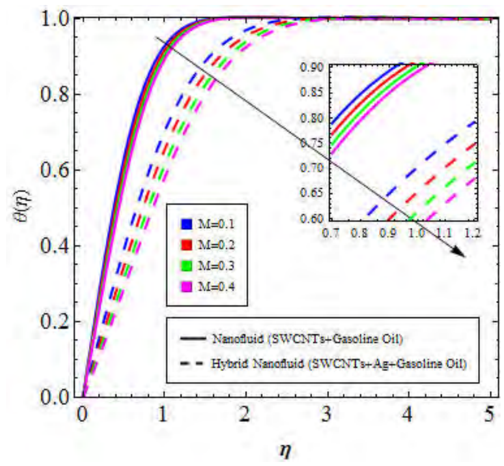

Fig. 9.16: $\theta(\eta)$ for higher M.

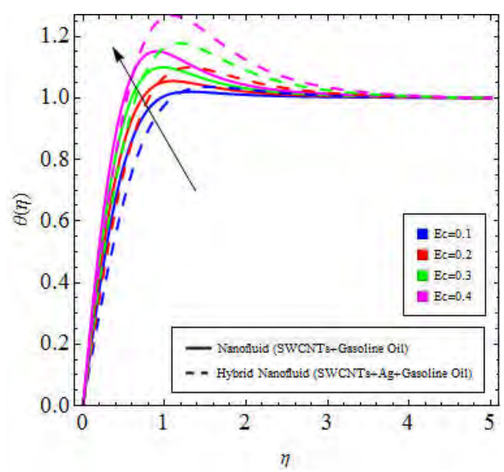

Fig. 9.17: $\theta(\eta)$ for higher Ec.

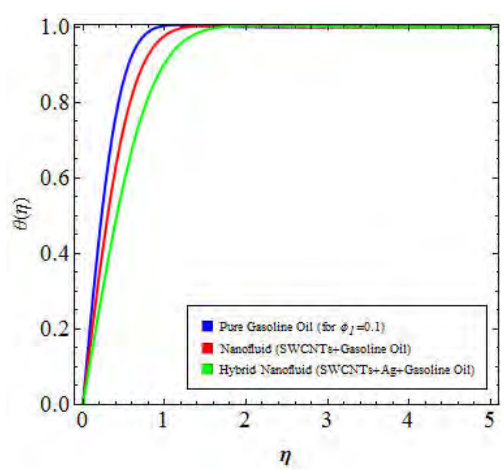

Fig. 9.18: Comparison of $\theta(\eta)$ for higher ϕ_1.

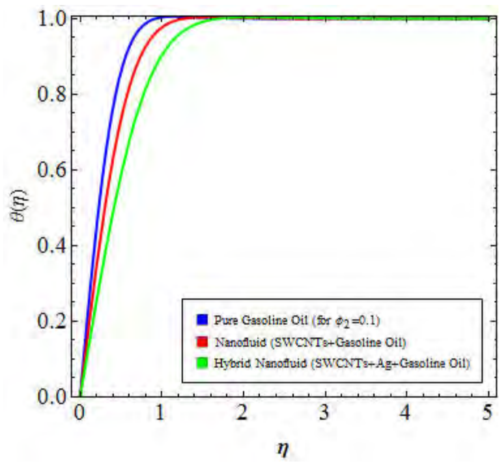

Fig. 9.19: Comparison of $\theta(\eta)$ for higher ϕ_2.

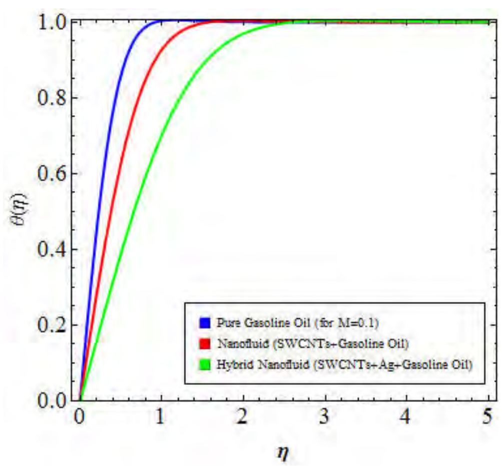

Fig. 9.20: Comparison of $\theta(\eta)$ for higher M.

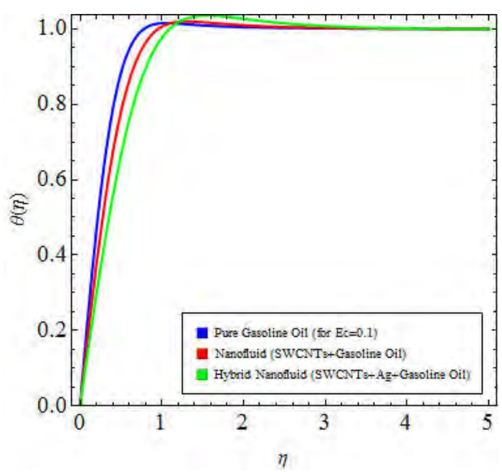

Fig. 9.21: Comparison of $\theta(\eta)$ for higher Ec.

9.6.3 Impacts of influential parameters on C_f (surface friction coefficient) and Nu_x (Nusselt number)

In order to make technological and industrial processes more efficient, surface friction coefficient must be reduced and cooling process (Nusselt number) must be enhanced. Thus C_f under influences of $\phi_{1,}$ ϕ_2 and M, A is plotted in Figs. 9.22 and 9.23 while Nu_x under influences of $\phi_{1,}$ ϕ_2 and M, A is plotted in Figs. 9.26 and 9.27 respectively. Skin friction (C_f) can be minimized via larger values of A. Similarly Nu_x can be regulated through higher values of $\phi_{1,}$ ϕ_2 and A. Comparison among hybrid nanofluid (SWCNTs+Ag+Gasoline oil), baseliquid (Gasoline oil) and nanofluid (SWCNTs+Gasoline oil) during impacts of $\phi_{1,}$ ϕ_2 and M, A on C_f is presented in Figs. 9.24 and 9.25. Similarly comparison during impacts of $\phi_{1,}$ ϕ_2 and M, A on Nu_x is performed in Figs. 9.28 and 9.29 respectively. Efficient performance is noticed for hybrid nanofluid (SWCNTs+Ag+Gasoline oil) followed by nanofluid (SWCNTs+Gasoline oil) and baseliquid (Gasoline oil) respectively.

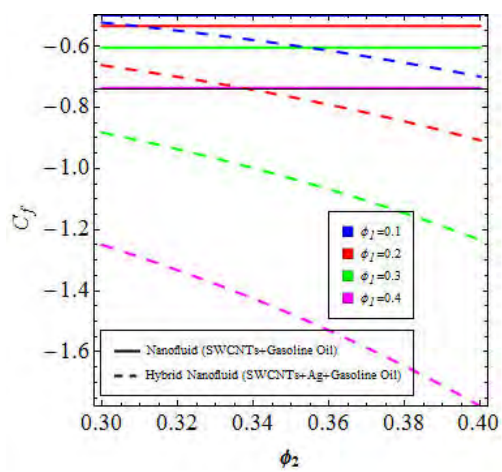

Fig. 9.22: C_f for higher ϕ_1 and ϕ_2.

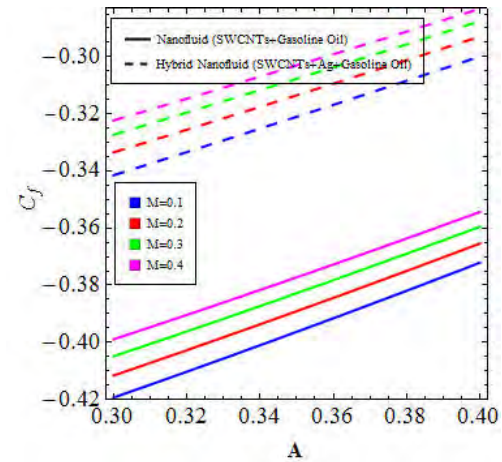

Fig. 9.23: C_f for higher M and A.

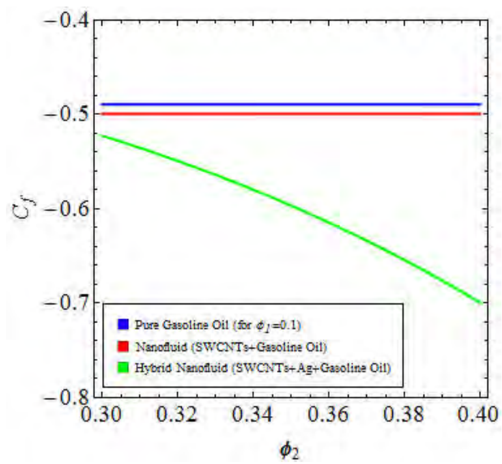

Fig. 9.24: Comparison of C_f for higher ϕ_1 and ϕ_2.

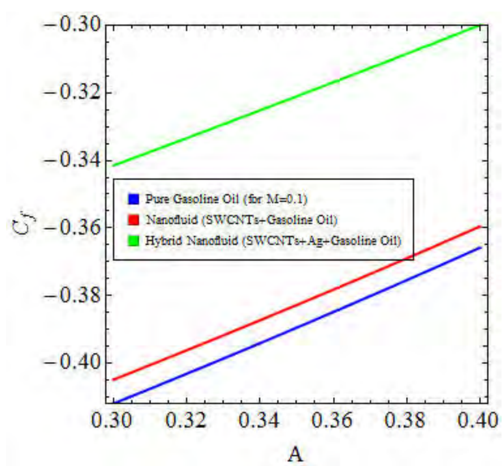

Fig. 9.25: Comparison of C_f for higher M and A.

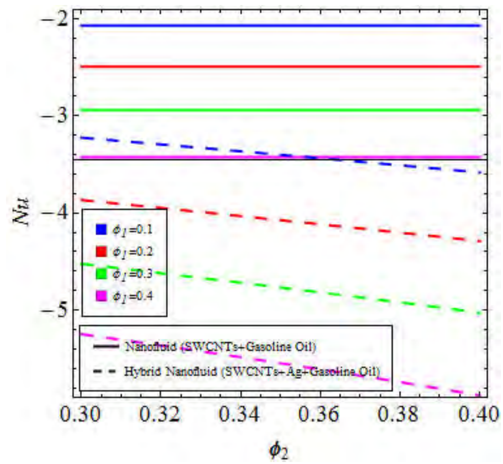

Fig. 9.26: Nu_x for higher ϕ_1 and ϕ_2.

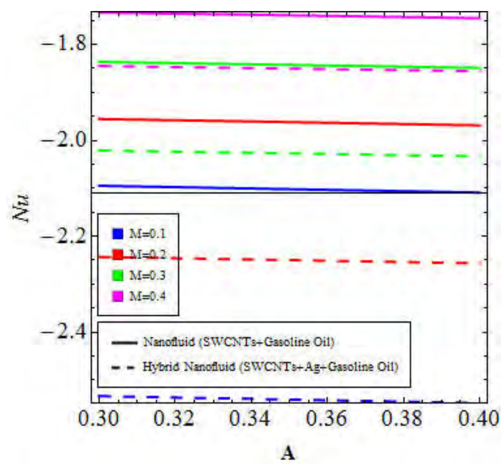

Fig. 9.27: Nu_x for higher M and A.

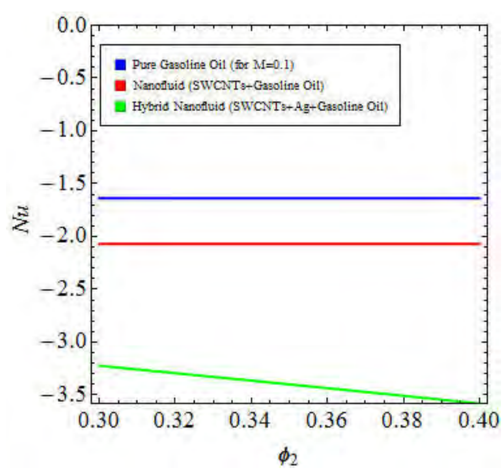

Fig. 9.28: Comparison of Nu_x for higher ϕ_1 and ϕ_2.

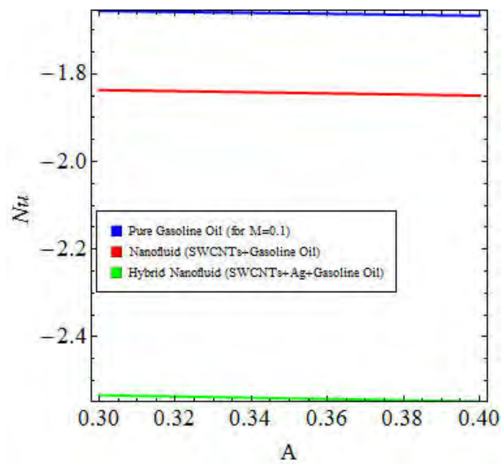

Fig. 9.29: Comparison of Nu_x for higher M and A.

9.7 Key observations

Our findings here are summarized as follows.

- Velocity ($f'(\eta)$) enlarges with higher estimations of ϕ_1, A, ϕ_2, M while it decays through α and m.
- Temperature ($\theta(\eta)$) reduces for higher ϕ_1, ϕ_2 and M while it intensifies with Ec.
- Surface friction coefficient (C_f) minimizes for higher estimation of A.
- Cooling process (Nusselt number) can be regulated with higher ϕ_1, A and ϕ_2.
- During comparison of $f'(\eta)$, $\theta(\eta)$, C_f and Nu_x, an efficient behavior is noted for hybrid nanofluid (SWCNTs+Ag+Gasoline oil) followed by nanofluid (SWCNTs+Gasoline oil) and baseliquid (Gasoline oil).

Chapter 10

Numerical study of Newtonian heating in flow of hybrid nanofluid (SWCNTs+CuO+Ethylene glycol) past a curved surface with viscous dissipation

10.1 Introduction

Present chapter concerns with investigation of hybrid nanomaterial (SWCNTs+CuO+Ethylene glycol) flow by curved non-linear stretched sheet. Heat transfer features are emphasized through Newtonian heating and viscous dissipation. Coupled non-linear ODEs are constructed from the filed equations (Continuity Eq., Momentum Eq. and Energy Eq.) by means of adequate transformations. Such resulting non-linear ODEs are then converted into system of first order ODEs and solved via shooting technique using RK-4 algorithms (bvp4c). Impacts of emerging flow variables toward temperature, skin friction coefficient, velocity and Nusselt number are illustrated graphically. Comparison among hybrid nanofluid (SWCNTs+CuO+Ethylene glycol), nanofluid (SWCNTs+Ethylene glycol) and basefluid (Ethylene glycol) is shown.

10.2 Formulation

Two-dimensional flow of hybrid nanofluid (SWCNTs+CuO+Ethylene glycol) due to curved stretched sheet is studied. Sheet is coiled in form of a circle having radius R. Curvilinear coordinates (s, r) are selected. In $s-$axis direction sheet is non-linearly stretched with velocity $U_w = as^m$ while $r-$axis is normal to it.

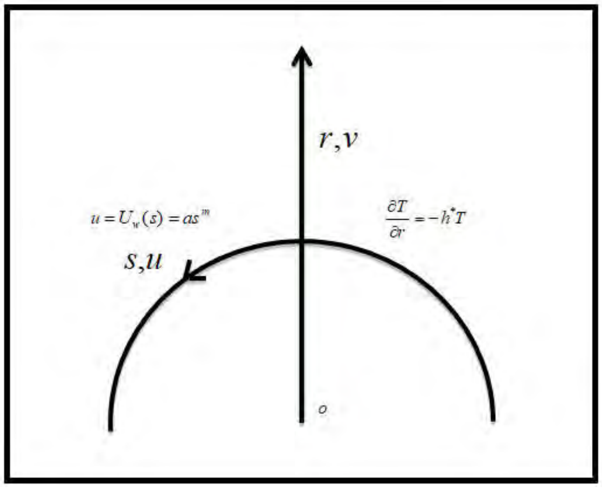

Fig. 10.1: Geometry for the flow field.

Viscous dissipation and Newtonian heating are accounted for exploring features of heat transfer. Single-walled CNTs and CuO are considered as first and second nanoparticles in ethylene glycol baseliquid. Under mentioned assumptions along with boundary layer approximations, the equations are

$$R\frac{\partial u}{\partial s} + \frac{\partial}{\partial r}((r+R)v) = 0, \tag{10.1}$$

$$\frac{\partial p}{\partial r} = \rho_{hnf}\frac{u^2}{r+R}, \tag{10.2}$$

$$\rho_{hnf}(v\frac{\partial u}{\partial r} + \frac{R}{r+R}u\frac{\partial u}{\partial s} + \frac{uv}{r+R}) = -\frac{R}{r+R}\frac{\partial p}{\partial s} + \mu_{hnf}(\frac{\partial^2 u}{\partial r^2} + \frac{1}{r+R}\frac{\partial u}{\partial r} - \frac{u}{(r+R)^2}), \tag{10.3}$$

$$(\rho c_p)_{hnf}(v\frac{\partial T}{\partial r} + \frac{R}{r+R}u\frac{\partial T}{\partial s}) = k_{hnf}(\frac{\partial^2 T}{\partial r^2} + \frac{1}{r+R}\frac{\partial T}{\partial r}) + \mu_{hnf}(\frac{\partial u}{\partial r} - \frac{1}{r+R}u)^2, \tag{10.4}$$

$$u = U_w(s) = U_0 s^m, \quad v = 0, \quad \frac{\partial T}{\partial r} = -h^* T \quad \text{at} \quad r = 0,$$

$$u \to 0, \quad \frac{\partial u}{\partial r} \to 0, \quad T \to T_\infty \quad \text{as} \quad r \to \infty. \tag{10.5}$$

Assume the transformations

$$u = U_0 s^m f'(\eta), \qquad v = -\frac{R}{r+R}\sqrt{U_0 s^{m-1} v_f}[\frac{m+1}{2}f(\eta) + \frac{m-1}{2}f'(\eta)], \qquad \eta = \sqrt{\frac{U_0 s^{m-1}}{v_f}} r,$$

$$p = \rho_f U_0^2 s^{2m} P(\eta), \qquad \theta(\eta) = \frac{T - T_\infty}{T_w - T_\infty}. \tag{10.6}$$

Implementation of these transformations leads to verification of Eq. 10.1 while Eqs. 10.2-10.4 with boundary conditions (in Eq. 10.5) become

$$\frac{P'}{A_{11}} = \frac{f'^2}{\eta+\gamma}, \tag{10.7}$$

$$\frac{m-1}{2}\frac{\gamma\eta}{\eta+\gamma}P' + \frac{2\gamma}{\eta+\gamma}P = \frac{(1-\phi_1)^{2.5}(1-\phi_2)^{2.5}}{A_{11}}\frac{m+1}{2}(\frac{\gamma}{\eta+\gamma}ff'' - \frac{\eta\gamma}{(\eta+\gamma)^2}f'^2 + \frac{\gamma}{(\eta+\gamma)^2}ff' - \frac{2}{m+1}\frac{\eta\gamma^2}{(\eta+\gamma)^2}.$$

$$-\frac{1}{(\eta+\gamma)^2}f' + \frac{1}{\eta+\gamma}f'' + f'''. \tag{10.8}$$

After elimination of P from Eqs. 10.6 and 10.7, we get

$$\frac{A_{11}}{(1-\phi_1)^{2.5}(1-\phi_2)^{2.5}}(f^{(iv)} - \frac{1}{(\eta+\gamma)^2}f'' + \frac{2}{\eta+\gamma}f''' + \frac{1}{(\eta+\gamma)^3}f') - \frac{3m-1}{2}(\frac{\gamma}{(\eta+\gamma)^2}f'^2 - \frac{\gamma}{\eta+\gamma}f'f'')$$

$$+\frac{m+1}{2}(\frac{\gamma}{\eta+\gamma}ff''' + \frac{\gamma}{(\eta+\gamma)^2}ff'' - \frac{\gamma}{(\eta+\gamma)^3}ff') = 0, \tag{10.9}$$

$$\frac{\kappa_{hnf}}{\kappa_f}(\theta'' + \frac{\theta'}{\eta+\gamma}) + B_{11}\frac{\gamma(m+1)}{2(\eta+\gamma)}\Pr f\theta' + \frac{\Pr Ec}{(1-\phi_1)^{2.5}(1-\phi_2)^{2.5}}\frac{1}{(\eta+\gamma)^2}((\eta+\gamma)f'' + f')^2 = 0, \tag{10.10}$$

$$f(0) = 0, \qquad f'(0) = 1, \qquad \theta'(0) = -\alpha^*(1+\theta(0)),$$

$$f' \to 0, \qquad f'' \to 0, \qquad \theta \to 0. \tag{10.11}$$

In above equations

$$A_{11} = \frac{1}{(1-\phi_2)\left((1-\phi_1) + \phi_1\frac{\rho_{m1}}{\rho_f}\right) + \phi_2\frac{\rho_{m2}}{\rho_f}}, \tag{10.12}$$

$$B_{11} = (1-\phi_2)\left((1-\phi_1) + \phi_1\frac{(\rho c_p)_{m1}}{(\rho c_p)_f}\right) + \phi_2\frac{(\rho c_p)_{m2}}{(\rho c_p)_f}. \tag{10.13}$$

Physical parameters in above equations are

$$\gamma = \sqrt{\frac{U_0 s^{1-m}}{v_f}}R, \quad \alpha^* = h^*\sqrt{\frac{s^{1-m}v_f}{U_0}}, \quad \Pr = \frac{\nu_f}{\alpha_f},$$

$$Ec = \frac{(U_w)^2\rho_f}{(\rho c_p)_f(T_w - T_\infty)}. \tag{10.14}$$

10.2.1 Dimensional and non-dimensional expressions for Nusselt number (Nu_s) and Skin friction coefficient (C_{fx})

Nusselt number and skin friction coefficient are

$$Nu_s = \frac{sq_s}{k_f(T_f - T_\infty)}, \quad C_{fx} = \frac{(\tau_{wx})_{r=0}}{\rho_f U_w^2}, \tag{10.15}$$

$$\text{with} \quad q_w = -k_{hnf}(\frac{\partial T}{\partial r})_{r=0}, \quad \tau_{wx} = \mu_{hnf}(\frac{\partial u}{\partial r} - \frac{1}{r+R}u). \tag{10.16}$$

After implementing transformations 10.6 the above expressions become

$$Nu_s(\mathrm{Re})^{-\frac{1}{2}} = \alpha^*\frac{\kappa_{hnf}}{\kappa_f}(1 + \frac{1}{\theta(0)}), \quad C_{fx}(\mathrm{Re})^{\frac{1}{2}} = \frac{1}{(1-\phi_1)^{2.5}(1-\phi_2)^{2.5}}(f''(0) + \frac{1}{\gamma}f'(0)). \tag{10.17}$$

Here local Reynolds number is $\mathrm{Re} = \frac{U_w s}{v_f}$.

10.3 Hamilton-Crosser model for nanomaterial (SWCNTs+Ethylene glycol) and hybrid nanomaterial (SWCNTs+CuO+Ethylene glycol)

Expressions for nanomaterial (SWCNTs+Ethylene glycol) and hybrid nanomaterial (SWCNTs+CuO+Ethylene glycol) defined by Hamilton-Crosser are

For nanofluid

$$\mu_{nf} = \frac{\mu_f}{(1-\phi_1)^{2.5}}, \quad \upsilon_{nf} = \frac{\mu_{nf}}{\rho_{nf}},$$

$$(\rho c_p)_{nf} = (1-\phi_1)(\rho c_p)_f + \phi_1(\rho c_p)_{m1},$$

$$
\begin{aligned}
\rho_{nf} &= (1-\phi_1)\,\rho_f + \phi_1 \rho_{m1}, \\
\frac{\kappa_{nf}}{\kappa_f} &= \frac{\kappa_{m1} + (n^*-1)\kappa_f - (n^*-1)\phi_1(\kappa_f - \kappa_{m1})}{\kappa_{m1} + (n^*-1)\kappa_f + \phi_1(\kappa_f - \kappa_{m1})},
\end{aligned} \tag{10.18}
$$

$$
\begin{aligned}
\mu_{hnf} &= \frac{\mu_f}{(1-\phi_1)^{2.5}(1-\phi_2)^{2.5}}, \qquad v_{hnf} = \frac{\mu_{hnf}}{\rho_{hnf}}, \\
(\rho c_p)_{hnf} &= (1-\phi_2)\left((1-\phi_1)(\rho c_p)_f + \phi_1(\rho c_p)_{m1}\right) + \phi_2(\rho c_p)_{m2}, \\
\rho_{hnf} &= (1-\phi_2)\big((1-\phi_1)\,\rho_f + \phi_1\rho_{m1}\big) + \phi_2\rho_{m2}, \\
\frac{\kappa_{hnf}}{\kappa_{bf}} &= \frac{\kappa_{m2} + (n^*-1)\kappa_{bf} - (n^*-1)\phi_2(\kappa_{bf} - \kappa_{m2})}{\kappa_{m2} + (n^*-1)\kappa_{bf} + \phi_2(\kappa_{bf} - \kappa_{m2})}, \\
\frac{\kappa_{nf}}{\kappa_f} &= \frac{\kappa_{m1} + (n^*-1)\kappa_f - (n^*-1)\phi_1(\kappa_f - \kappa_{m1})}{\kappa_{m1} + (n^*-1)\kappa_f + \phi_1(\kappa_f - \kappa_{m1})}.
\end{aligned} \tag{10.19}
$$

In above expressions we have taken $n^* = 6$ (shape parameter) as we have considered cylindrical shaped nanoparticles.

Table. 10.1: Thermal features of SWCNTs, CuO and ethylene glycol [58].

Nanoparticles\ Properties	Pr	$\kappa(\frac{W}{mK})$	$c_p(\frac{J}{kgK})$	$\rho(\frac{kg}{m^3})$
SWCNTs	-	6600	425	2600
CuO	-	76.50	531.80	0.6320
Ethylene glycol	2.0363	0.253	2430	1115

10.4 Methodology

Field equations (PDEs) after converting into ODEs are solved by shooting method (bvp4c). Such method is applied on first order ODEs. Thus we adopt the following procedure

$$
m_{01} = f, \quad m_{02} = m_{01}' = f', \quad m_{03} = m_{02}' = f'', \quad m_{04} = m_{03}' = f''', \tag{10.20}
$$

$$
m_{01} = \theta, \quad m_{11} = m_{01}' = \theta' \tag{10.21}
$$

$$
\begin{aligned}
m_m = m_{04}' = f'''' = -(\frac{2}{\eta+\gamma}m_{04} + \frac{1}{(\eta+\gamma)^3}m_{02} - \frac{1}{(\eta+\gamma)^2}m_{03}) - \frac{(1-\phi_1)^{2.5}(1-\phi_2)^{2.5}}{A_{11}}(\frac{3m-1}{2}(\frac{\gamma}{(\eta+\gamma)^2}m_{02}^2 - \\
+\frac{m+1}{2}(\frac{\gamma}{\eta+\gamma}m_{01}m_{04} + \frac{\gamma}{(\eta+\gamma)^2}m_{01}m_{03} - \frac{\gamma}{(\eta+\gamma)^3}m_{01}m_{02})),
\end{aligned} \tag{10.22}
$$

$$m_n = m'_{11} = \theta'' = \frac{1}{\frac{\kappa_{hnf}}{\kappa_f}}(B_{11} \Pr m_{01} m_{11} + \frac{\Pr Ec}{(1-\phi_1)^{2.5}(1-\phi_2)^{2.5}} \frac{1}{(\eta+\gamma)^2}(m_{02} + (\eta+\gamma) m_{03})^2) - \frac{m_{11}}{\eta+\gamma}, \tag{10.23}$$

$$m_{01}(0) = 0, \quad m_{02}(0) = 1, \quad m_{11}(0) = -\alpha(1+m_{01}(0)), \quad m_{02} \to 0, \quad m_{03} \to 0, \quad m_{10} \to 0 \quad \text{as} \quad \eta \to \infty. \tag{10.24}$$

10.5 Analysis

Role of present section is to elaborate graphically the impacts of involved physical variables on Nusselt number, temperature, flow and skin friction coefficient. Also for basefluid (Ethylene glycol) $\phi_1 = \phi_2 = 0$, for nanofluid (SWCNTs+Ethylene glycol) both $\phi_1 = 0$ and $\phi_2 = 0.2$ and for hybrid nanofluid (SWCNTs+CuO+Ethylene glycol) ϕ_1 and ϕ_2 are adjusted for better performance.

10.5.1 Behavior of velocity ($f'(\eta)$) via involved parameters

Fig 10.2.portrays the effects of ϕ_1 on $f'(\eta)$. It can be seen that increase in ϕ_1 intensifies $f'(\eta)$. Illustrious behavior is shown by hybrid nanomaterial (SWCNTs+CuO+Ethylene glycol) when compared with nanomaterial (SWCNTs+Ethylene glycol). Effects of ϕ_2 on $f'(\eta)$ is plotted in Fig. 10.3. Velocity ($f'(\eta)$) intensifies with ϕ_2. Accurately no effect of ϕ_2 is seen on nanomaterial (SWCNTs+Ethylene glycol) due to association with hybrid nanomaterial (SWCNTs+CuO+Ethylene glycol) only. Fig. 10.4 describes $f'(\eta)$ under higher γ. Growth in boundary layer is examined via higher γ. Increment in γ leads to increase in radius of curved surface which is associated with the increment in area of contact between fluid and solid surface. Hence $f'(\eta)$ enlarges. Effects of m on $f'(\eta)$ is portrayed in Fig. 10.5. Velocity ($f'(\eta)$) reduces with increment in m. Eminent behavior behavior is analyzed for hybrid nanomaterial (SWCNTs+CuO+Ethylene glycol) as compared to nanomaterial (SWCNTs+Ethylene glycol). Comparison among hybrid nanomaterial (SWCNTs+CuO+Ethylene glycol), nanomaterial (SWCNTs+Ethylene glycol) and basefluid (Ethylene glycol) during analyzing effects of ϕ_1, ϕ_2, γ and m on $f'(\eta)$ is labeled in Figs. 10.6-10.9. Efficient performance is observed for hybrid nanomaterial (SWCNTs+CuO+Ethylene glycol) when compared with nanomaterial

(SWCNTs+Ethylene glycol) and basefluid (Ethylene glycol).

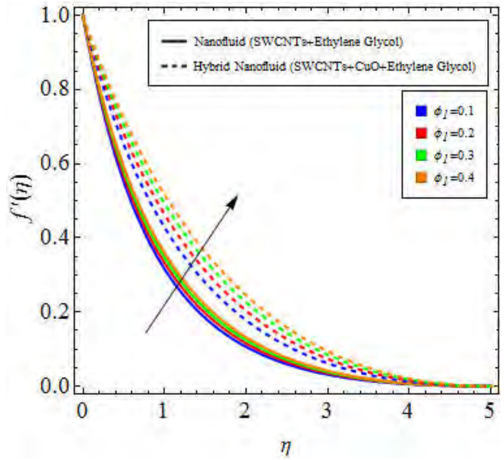

Fig. 10.2: $f'(\eta)$ for higher ϕ_1.

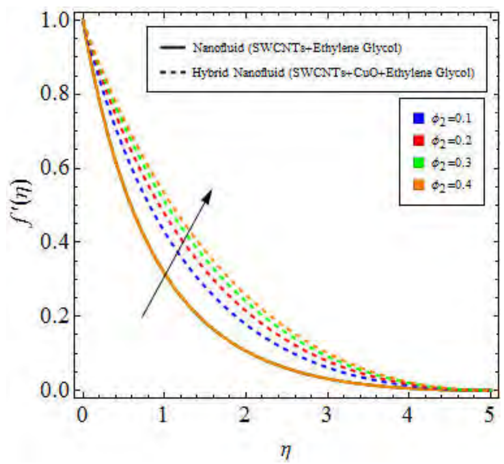

Fig. 10.3: $f'(\eta)$ for higher ϕ_2.

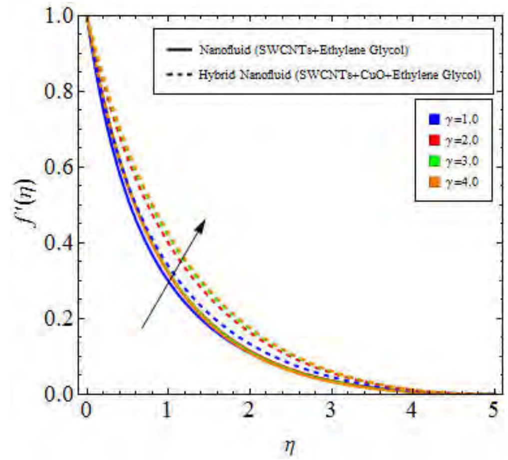

Fig. 10.4: $f'(\eta)$ for higher γ.

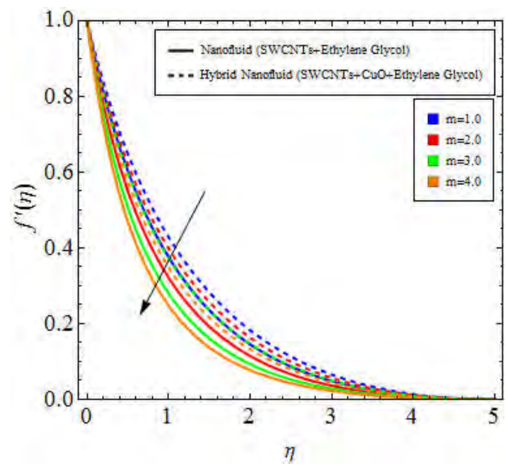

Fig. 10.5: $f'(\eta)$ for higher m.

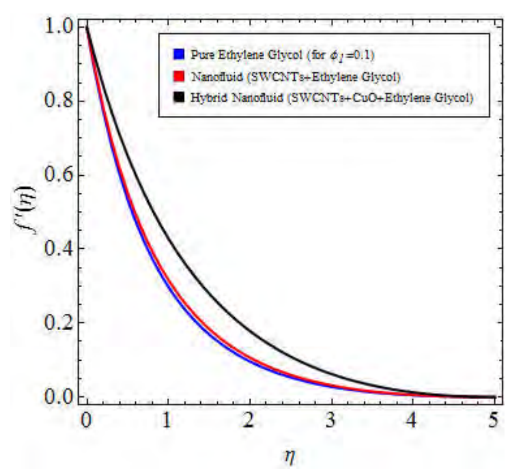

Fig. 10.6: Comparison of $f'(\eta)$ for higher ϕ_1.

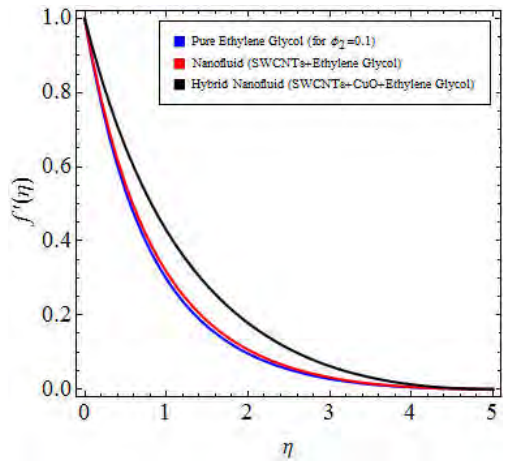

Fig. 10.7: Comparison of $f'(\eta)$ for higher ϕ_2.

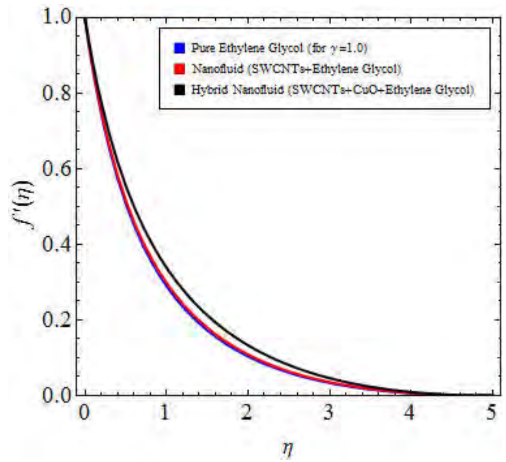

Fig. 10.8: Comparison of $f'(\eta)$ for higher γ.

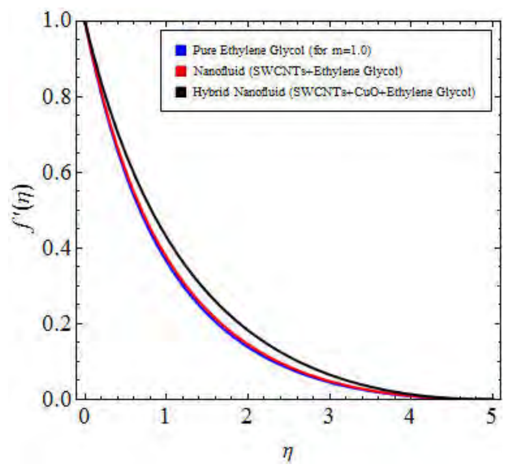

Fig. 10.9: Comparison of $f'(\eta)$ for higher m.

10.5.2 Behavior of temperature ($\theta(\eta)$) via involved parameters

Fig. 10.10 analyzed the impacts of ϕ_1 on $\theta(\eta)$. It is noticed that rise in ϕ_1 enlarges $\theta(\eta)$. Prominent trend is shown by hybrid nanomaterial (SWCNTs+CuO+Ethylene glycol) in comparison to nanomaterial (SWCNTs+Ethylene glycol). Temperature ($\theta(\eta)$) under higher values of ϕ_2 is depicted in Fig. 10.11. Increment in ϕ_2 directly affect $\theta(\eta)$. Also no impact of ϕ_2 is seen on $\theta(\eta)$ during considering nanomaterial (SWCNTs+Ethylene glycol). Fig. 10.12 portrays effects of γ on $\theta(\eta)$. Intensification in $\theta(\eta)$ is analyzed via γ while eminent performance is shown by hybrid nanomaterial (SWCNTs+CuO+Ethylene glycol). In Fig. 10.13, $\theta(\eta)$ under higher m is analyzed. Higher m cause reduction in $\theta(\eta)$. Impacts of hybrid nanomaterial (SWCNTs+CuO+Ethylene glycol) are more than nanomaterial (SWCNTs+Ethylene glycol). $\theta(\eta)$ against higher values of Ec is sketch in Fig. 10.14. Higher Ec causes rise in $\theta(\eta)$. As Ec defines ratio of K.E to enthalpy. Hence rise in Ec leads to increase in K.E. Thus $\theta(\eta)$ enlarges. Fig. 10.15 depicts variations in $\theta(\eta)$ against higher α. Rise in α is associated with increment in coefficient of heat transfer. Hence $\theta(\eta)$ rises. Figs. 10.16-10.21 display comparative study among hybrid nanomaterial (SWCNTs+CuO+Ethylene glycol), nanomaterial (SWCNTs+Ethylene glycol) and basefluid (Ethylene glycol) during influences of ϕ_1, ϕ_2, γ, m, Ec and α on $\theta(\eta)$. During comparative analysis better performance is found for hybrid nanomaterial (SWCNTs+CuO+Ethylene glycol) followed by nanomaterial (SWCNTs+Ethylene glycol) and basefluid (Ethylene glycol) respectively.

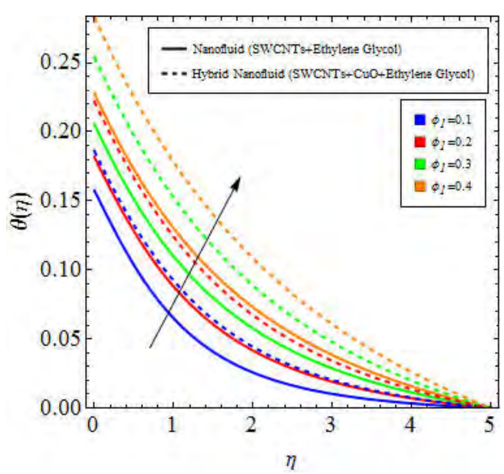

Fig. 10.10: $\theta(\eta)$ for higher ϕ_1.

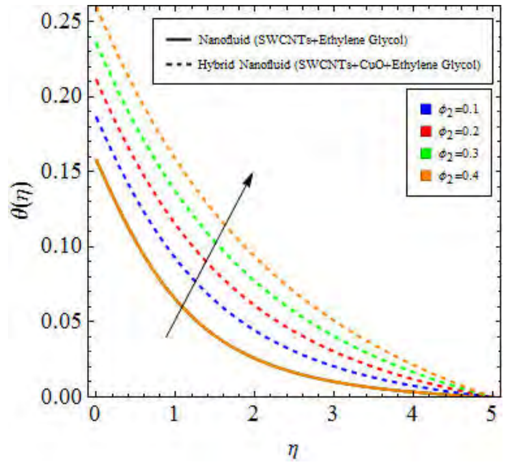

Fig. 10.11: $\theta(\eta)$ for higher ϕ_2.

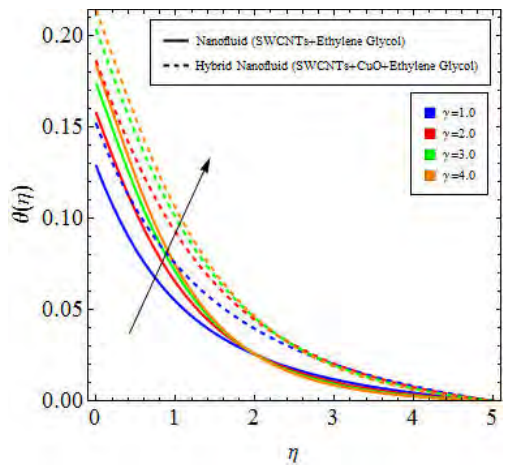

Fig. 10.12: $\theta(\eta)$ for higher γ.

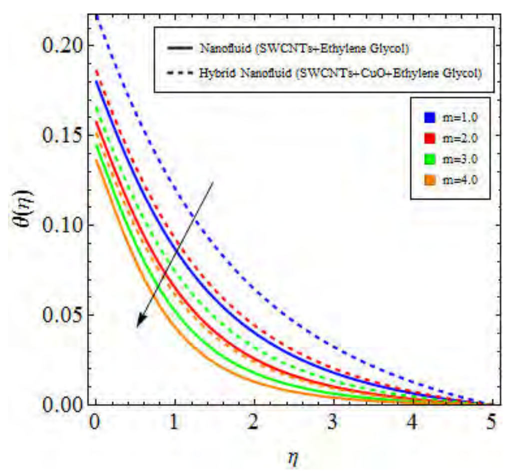

Fig. 10.13: $\theta(\eta)$ for higher m.

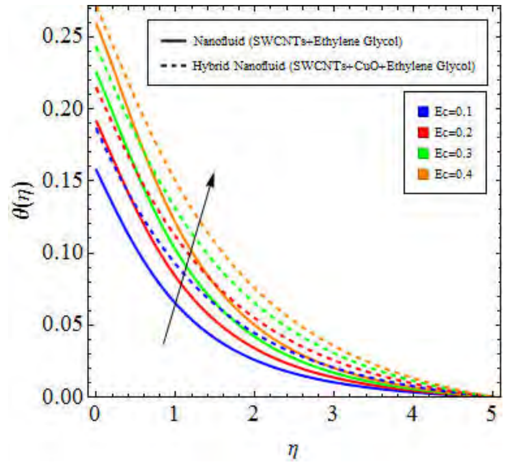

Fig. 10.14: $\theta(\eta)$ for higher Ec.

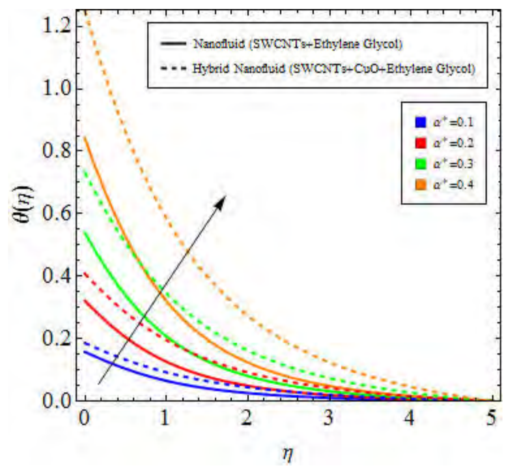

Fig. 10.15: $\theta(\eta)$ for higher α^*.

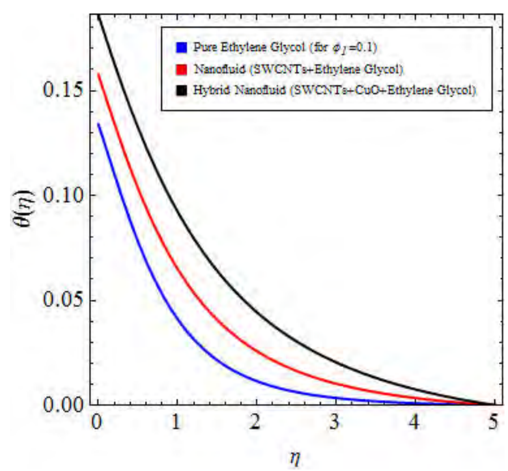

Fig. 10.16: Comparison of $\theta(\eta)$ for higher ϕ_1.

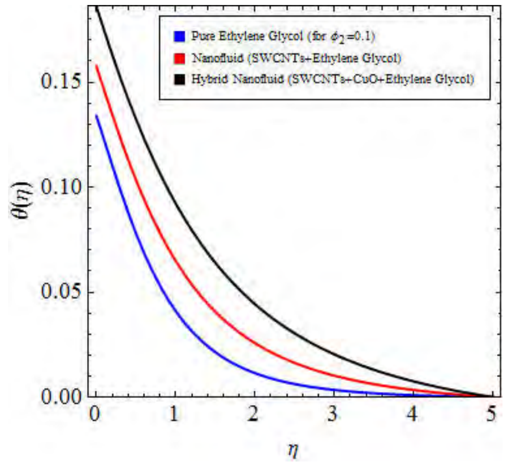

Fig. 10.17: Comparison of $\theta(\eta)$ for higher ϕ_2.

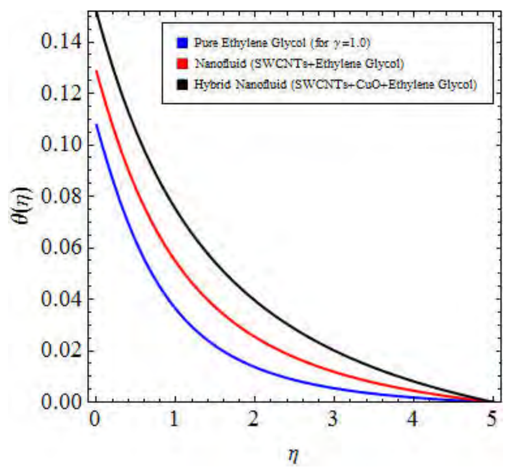

Fig. 10.18: Comparison of $\theta(\eta)$ for higher γ.

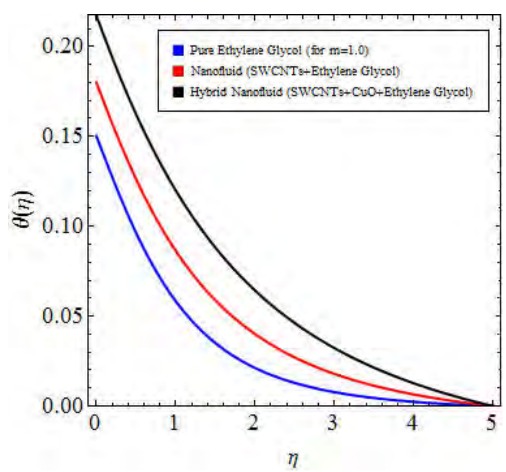

Fig. 10.10: Comparison of $\theta(\eta)$ for higher m.

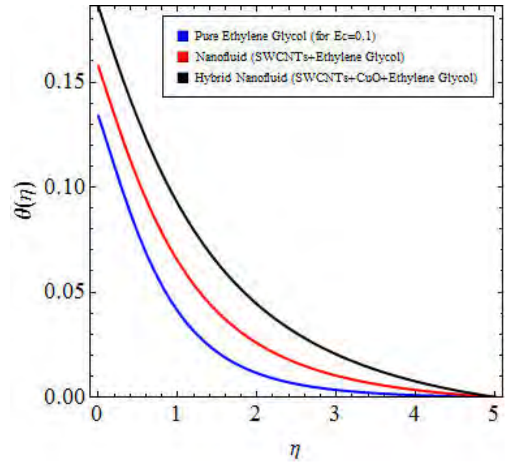

Fig. 10.20: Comparison of $\theta(\eta)$ for higher Ec.

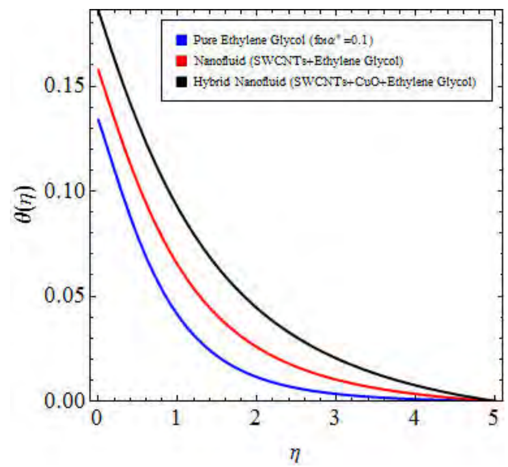

Fig. 10.21: Comparison of $\theta(\eta)$ for higher α^*.

10.5.3 Variations in C_f (skin friction coefficient) and Nu_s (Nusselt number) via involved parameters

Skin friction coefficient (C_f) under higher estimations of ϕ_1 and ϕ_2 is displayed in Fig. 10.22. Both ϕ_1 and ϕ_2 cause increment in C_f. Moreover efficient behavior is shown by hybrid nanomaterial (SWCNTs+CuO+Ethylene glycol). Fig. 10.23 is sketched for studying effects of γ and m on C_f. Rise in C_f occurs with higher m while it decays against γ. Impact of hybrid nanomaterial (SWCNTs+CuO+Ethylene glycol) on C_f is more than nanomaterial (SWCNTs+Ethylene glycol). Comparative observation among hybrid nanomaterial (SWCNTs+CuO+Ethylene glycol), nanomaterial (SWCNTs+Ethylene glycol) and basefluid (Ethylene glycol) is made in Figs.

10.24 and 10.25 during studying impacts of ϕ_1, ϕ_2 and m, γ on C_f. As expected performance of hybrid nanomaterial (SWCNTs+CuO+Ethylene glycol) is efficient and is followed by nanomaterial (SWCNTs+Ethylene glycol) and basefluid (Ethylene glycol) respectively. Nu_s under higher values ϕ_1 and ϕ_2 is labeled in Figs. 10.26. Nu_s varies directly with rise in both ϕ_1 and ϕ_2. Fig. 10.27 is displayed for effects of γ and α on Nu_s. Nu_s decays with higher γ while it enhances with α. Figs. 10.28 and 10.29 are plotted for comparison among hybrid nanomaterial (SWCNTs+CuO+Ethylene glycol), nanomaterial (SWCNTs+Ethylene glycol) and basefluid (Ethylene glycol) during analyzing impacts of ϕ_1, ϕ_2 and α, γ on Nu_s. Hybrid nanomaterial (SWCNTs+CuO+Ethylene glycol) shows efficient behavior followed by nanomaterial (SWCNTs+Ethylene glycol) and basefluid (Ethylene glycol) respectively.

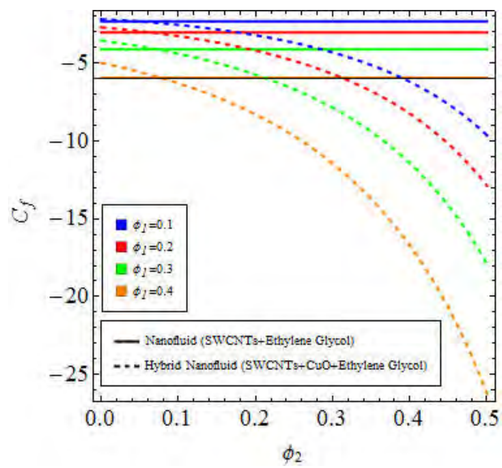

Fig. 10.22: C_f for higher ϕ_1 and ϕ_2.

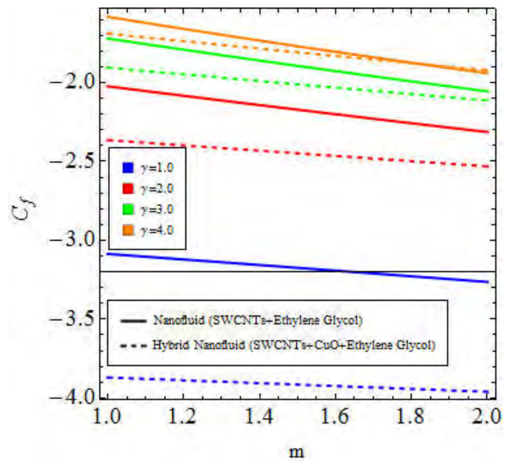

Fig. 10.23: C_f for higher γ and m.

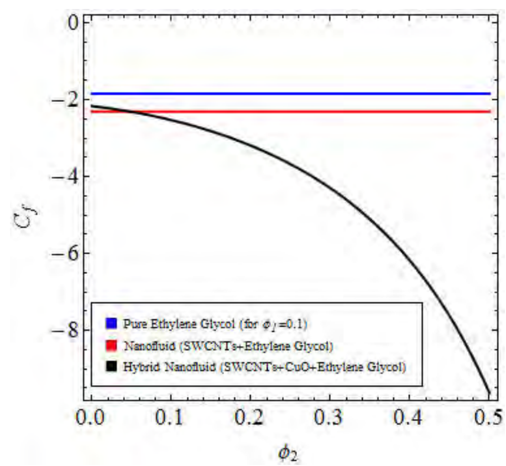

Fig. 10.24: Comparison of C_f for higher ϕ_1 and ϕ_2.

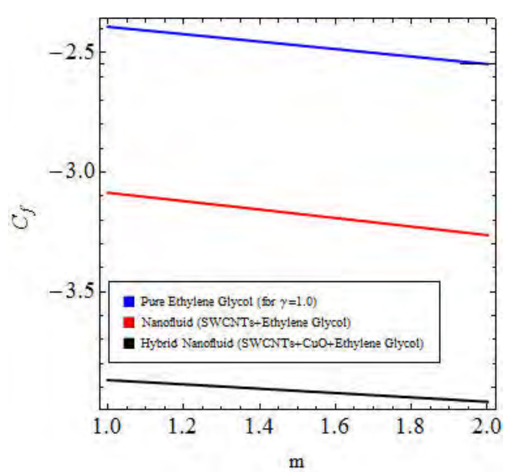

Fig. 10.25: Comparison of C_f for higher γ and m.

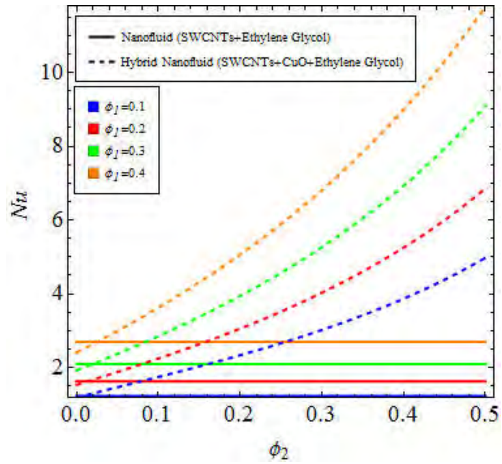

Fig. 10.26: Nu_s for higher ϕ_1 and ϕ_2.

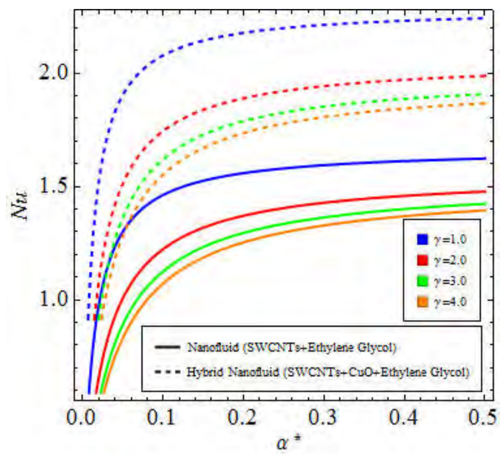

Fig. 10.27: Nu_s for higher γ and α.

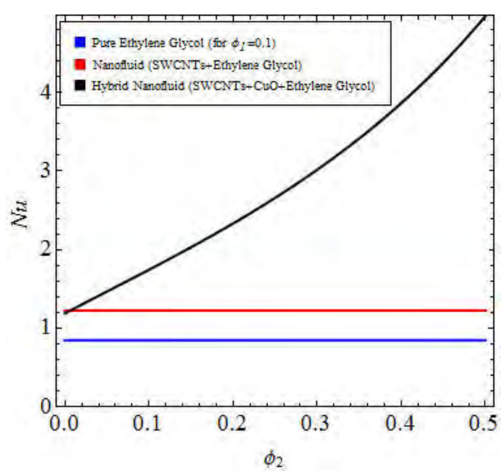

Fig. 10.28: Comparison of Nu_s for higher ϕ_1 and ϕ_2.

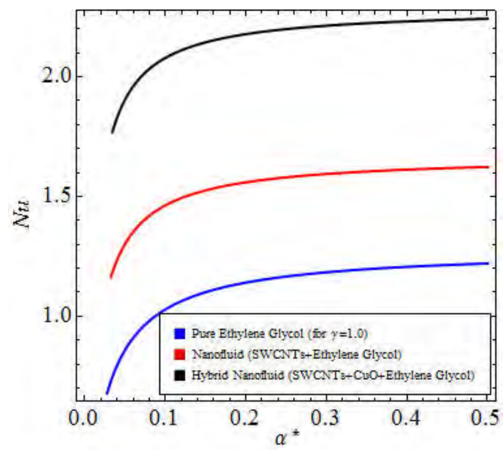

Fig. 10.29: Comparison of Nu_s for higher γ and α^*.

10.6 Key points

Main points are listed below.

- Higher ϕ_1, ϕ_2 and γ lead to decay in velocity ($f'(\eta)$) while reverse behavior of $f'(\eta)$ is noticed for m.
- Enlargement of temperature ($\theta(\eta)$) occurs with increment in Ec, ϕ_1, α, ϕ_2 and γ while it reduces for higher m.
- Higher drag force (skin friction coefficient) occur with ϕ_1, m and ϕ_2 while it can be controlled via larger estimations of γ.
- Cooling process (heat transfer rate) can be intensified via larger estimations of ϕ_1 and ϕ_2 while it reduces with an increase in γ and α.
- During comparative study it is shown that performance of hybrid nanomaterial (SWCNTs+CuO+Ethylene glycol) is better than nanomaterial (SWCNTs+Ethylene glycol) and basefluid (Ethylene glycol).

Bibliography

[1] S. U. S. Choi and J. A. Eastman, Enhancing thermal conductivity of fluids with nanoparticles: The Proceedings of the 1995 ASME International Mechanical Engineering Congress and Exposition, San Francisco, USA, ASME, FED 231/MD, 66 (1995) 99-105.

[2] M. M. Elias, M. Miqdad, I. M. Mahbubul, R. Saidur, M. Kamalisarvestani, M. R. Sohel, A. Hepbasli, N. A. Rahim and M. A. Amalina, Effect of nanoparticle shape on the heat transfer and thermodynamic performance of a shell and tube heat exchanger. Int. Commu. Heat Mass Transfer 44 (2013) 93-99.

[3] M. F. L. D. Volder, S. H. Tawfick, R. H. Baughman and A. J. Hart, Carbon nanotubes: present and future commercial applications. science 339 (2013) 535-539.

[4] J. Sarkar, P. Ghosh, and A. Adil. A review on hybrid nanofluids: recent research, development and applications, Renewable and Sustainable Energy Reviews 43 (2015) 164-177.

[5] Tanzila Hayat and S. Nadeem, Heat transfer enhancement with Ag-CuO/water hybrid nanofluid, Results in Physics 7 (2017) 2317-2324.

[6] G. Huminic and A. Huminic, The influence of hybrid nanofluids on the performances of elliptical tube: Recent research and numerical study, International Journal of Heat and Mass Transfer 129 (2019) 132-143.

[7] Q. Xue, Model for thermal conductivity of carbon nanotube based composites. Phys. B Condens Matter 368 (2005) 302-307.

[8] T. Hayat, K. Muhammad, M. Farooq and A. Alsaedi, Melting heat transfer in stagnation point flow of carbon nanotubes towards variable thickness surface, AIP advances 6 (2016) 015214.

[9] M. I. Khan, A. Kumar, T. Hayat, M. Waqas and R. Singh, Entropy generation in flow of Carreau nanofluid, Journal of Molecular Liquids 278 (2019) 677-687.

[10] J. Buongiorno, Convective transport in nanofluids, ASME Journal of Heat Transfer 128 (2006) 240-250.

[11] M. Turkyilmazoglu, Single phase nanofluids in fluid mechanics and their hydrodynamic linear stability analysis. Computer Methods and Programs in Biomedicine 187 (2020):105171.

[12] T. Hayat, S. Qayyum, S. A. Shehzad and A. Alsaedi, Simultaneous effects of heat generation/absorption and thermal radiation in magnetohydrodynamics (MHD) flow of Maxwell nanofluid towards a stretched surface, Results Phys. 7 (2017) 562-573.

[13] S. Dinarvand and I. Pop, Free-convective flow of copper/water nanofluid about a rotating down-pointing cone using Tiwari-Das nanofluid scheme, Advanced Powder Technology 28 (2017) 900-909.

[14] B. Souayeh, K. G. Kumar, M. G. Reddy, S. Rani, N. Hdhiri, H. Alfannakh and M. R. Gorji, Slip flow and radiative heat transfer behavior of Titanium alloy and ferromagnetic nanoparticles along with suspension of dusty fluid, Journal of Molecular Liquids 290 (2019),111-223.

[15] S. Soltani, A, Kasaeian, H. Sarrafha and D. Wen, An experimental investigation of a hybrid photovoltaic/thermoelectric system with nanofluid application, Solar Energy 155 (2017) 1033-1043.

[16] M. Sheikholeslami and H. B. Rokni, Nanofluid two phase model analysis in existence of induced magnetic field, International Journal of Heat and Mass Transfer 107 (2017) 288-299.

[17] M. I. Khan, T. Hayat, A. Alsaedi, S. Qayyum and M. Tamoor, Entropy optimization and quartic autocatalysis in MHD chemically reactive stagnation point flow of Sisko nanomaterial, International Journal of Heat and Mass Transfer 127 (2018) 829-837.

[18] Y. Ma, R. Mohebbi, M. M. Rashidi, Z. Yang and M. A. Sheremet, Numerical study of MHD nanofluid natural convection in a baffled U-shaped enclosure, International Journal of Heat and Mass Transfer 130 (2019) 123-134.

[19] A. Hussanan, I. Khan, M. Rahimi-Gorji and W. A. Khan, CNTS water-based nanofluid over a stretching sheet, BioNanoScience DOI: doi.org/10.1007/s12668-018-0592-6.

[20] K. Muhammad, T. Hayat, A.Alsaedi, B. Ahmad, Numerical study of entropy production minimization in Bödewadt flow with carbon nanotubes, Physica A: Statistical Mechanics and its Applications 550 (2020) 123966.

[21] L. J. Crane, Flow past a stretching plate. Zeitschrift fur Angewandte Mathematik und Physik 21 (1970) 645-641.

[22] M. I. Khan, T. Hayat, A. Alsaedi, S. Qayyum and M. Tamoor, Entropy optimization and quartic autocatalysis in MHD chemically reactive stagnation point flow of Sisko nanomaterial, International Journal of Heat and Mass Transfer 127 (2018) 829-837.

[23] N. S. Khashi'ie, N. M. Arifin, R. Nazar and E. H. Hafidzuddin, N. Wahi and I. Pop, Magnetohydrodynamics (MHD) axisymmetric flow and heat transfer of a hybrid nanofluid past a radially permeable stretching/shrinking sheet with joule heating, Chinese Journal of Physics 64 (2020) 251-263.

[24] T. Hayat, R. S. Saif, R. Ellahi, T. Muhammad and A. Alsaedi, Simultaneous effects of melting heat and internal heat generation in stagnation point flow of Jeffrey fluid towards a nonlinear stretching surface with variable thickness, International Journal of Thermal Sciences 132 (2018) 344-354.

[25] S. Z. Alamri, A. A. Khan, M. Azeez and R. Ellahi, Effects of mass transfer on MHD second grade fluid towards stretching cylinder: A novel perspective of Cattaneo–Christov heat flux model, Physics Letters A 383 (2019) 276-281.

[26] S. A. Khan, T. Saeed, M. Ijaz Khan, T. Hayat, M. Imran Khan and A. Alsaedi, Entropy optimized CNTs based Darcy-Forchheimer nanomaterial flow between two stretchable rotating disks, International Journal of Hydrogen Energy 44 (2019) 31579-31592.

[27] M. Naveed, Z. Abbas and M. Sajid, Hydromagnetic flow over an unsteady curved stretching surface, Engineering Science and Technology, an International Journal 19 (2019) 841-845.

[28] M. Gholinia, M. Armin, A. A. Ranjbar and D. D. Ganji, Numerical thermal study on CNTs/ C2H6O2– H2O hybrid base nanofluid upon a porous stretching cylinder under impact of magnetic source, Case Studies in Thermal Engineering14 (2019) 100490.

[29] M. Bilal, M. Sagheer and S. Hussain, Numerical study of magnetohydrodynamics and thermal radiation on Williamson nanofluid flow over a stretching cylinder with variable thermal conductivity, Alexandria Engineering Journal 57 (2018) 3281-3289.

[30] T. Hayat, K. Muhammad, A. Alsaedi and B. Ahmad, Melting effect in squeezing flow of third-garde fluid with non-Fourier heat flux model, Physica Scripta (2019) doi: 10.1088/1402-4896/ab1c2c.

[31] J. Engmann., S. Servai and A. S. Burbidge, Squeeze flow theory and applications to rheometry: A review 132 (2005), pp. 1-27.

[32] M. J. Stefan, Versuch ber die scheinbare adhesion, Akad Wissensch Wien Math Natur. 69 (1874)713.

[33] T. Hayat, S. Qayyum and A. Alsaedi, A., Three-dimensional mixed convection squeezing flow, Appl. Math. Mech. 36 (2015).47-60.

[34] A. Qayyum, M. Awais, A. Alsaedi and T. Hayat, Unsteady squeezing flow of Jeffrey fluid between two parallel disks, Chinese. Phys. Lett. 29 (2012) 034701.

[35] T. Hayat, M. Khan, T. Muhammad and A. Alsaedi, A useful model for squeezing flow of nanofluid, Journal of Molecular Liquids 237 (2017) 447-454.

[36] T. Muhammad, T. Hayat, A. Alsaedi and A. Qayyum, Hydromagnetic unsteady squeezing flow of Jeffrey fluid between two parallel plates, Chinese Journal of Physics, 55 (2017) 1511-1522.

[37] T. Hayat, K. Muhammad, M. Farooq and A.Alsaedi, Squeezed flow subject to Cattaneo-Christov heat flux and rotating frame, Journal of Molecular Liquids, 220 (2016) 216-222.

[38] K. Gupta and S. S. Ray, Numerical treatment for investigation of squeezing unsteady nanofluid flow between two parallel plates, Powder Technology 279 (2015) 282-289.

[39] T. Hayat, M. Khan, M. Imtiaz and A. Alsaedi, Squeezing flow past a Riga plate with chemical reaction and convective conditions, Journal of Molecular Liquids 225 (2017) 569-576.

[40] M. Sheikholeslami, D. D. Ganji and H. R. Ashorynejad, Investigation of squeezing unsteady nanofluid flow using ADM. Powder Technology 239 (2013) 259-265.

[41] L. Roberts, On the melting of a semi-infinite body of ice placed in a hot stream of air. J. Fluid Mech. 4 (1958) 505-528.

[42] T. Hayat, M. Farooq and A. Alsaedi, Melting heat transfer in the stagnation point flow of Maxwell fluid with double-diffusive convection. Int. J. Numer. Methods Heat Fluid Flow 24 (2014) 760-774.

[43] K. Das, Radiation and melting effects on MHD boundary layer flow over a moving surface. Ain Shams Eng. J. 5 (2014) 1207-1214.

[44] N. A. Yacob, A. Ishak and I. Pop, Melting heat transfer in boundary layer stagnation-point flow towards a stretching/shrinking sheet in a micropolar fluid. Computers & Fluids 47 (2011) 16-21.

[45] N. Bachok, A. Ishak and I. Pop, Melting heat transfer in boundary layer stagnation-point flow towards a stretching / shrinking sheet. Physics Letters A 374 (2010) 4075-4079.

[46] C. J. Ho and J.Y. Gao, An experimental study on melting heat transfer of paraffin dispersed with Al_2O_3 nanoparticles in a vertical enclosure. International Journal of Heat and Mass Transfer 62 (2013) 2-8.

[47] T. Hayat, K. Muhammad, A. Alsaedi and S. Asghar, Thermodynamics by melting in flow of an Oldroyd-B material, J. Braz. Soc. Mech. Sci. Eng. (2018) 40: 530. doi.org/10.1007/s40430-018-1447-3.

[48] B. J. Gireesha, B. Mahanthesh, I. S. Shivakumara and K. M. Eshwarappa, Melting heat transfer in boundary layer stagnation-point flow of nanofluid toward a stretching sheet with induced magnetic field, Engineering Science and Technology, an International Journal 19 (1), 313-321.

[49] T. Hayat, R. S. Saif, R. Ellahi, T. Muhammad and A. Alsaedi, Simultaneous effects of melting heat and internal heat generation in stagnation point flow of Jeffrey fluid towards a nonlinear stretching surface with variable thickness, International Journal of Thermal Sciences 132 (2018) 344-354.

[50] M. Awais, T. Hayat and A. Alsaedi, Investigation of heat transfer in flow of Burgers fluid during a melting process. J. Egypt. Math. Soci. 23 (2015) 410-415.

[51] P. D. Weidman and V. Putkaradze, Axisymmetric stagnation flow obliquely impinging on a circular cylinder. Eur. J. Mech. B/Fluids 22 (2003) 123-131.

[52] T. R. Mahapatra and A. S. Gupta, Heat transfer in stagnation-point flow towards a stretching sheet. Heat Mass Transfer 38 (2002) 517-521.

[53] S. Pop, T. Grosan and I. Pop, Radiation effects on the flow near the stagnation point of a stretching sheet. Technische Mech. 25 (2004) 100-106.

[54] P. Sharma and G. Singh, Effects of variable thermal conductivity and heat source/sink on MHD flow near a stagnation point on a linearly stretching sheet. Journal of Applied Fluid Mechanics 2 (2009) 13-21.

[55] T. Hayat and M. Nawaz, Unsteady stagnation point flow of viscous fluid caused by an impulsively rotating disk. J. Taiwan Inst. Chem. Eng. 42 (2011) 41-49.

[56] M. Turkyilmazoglu and I. Pop, Exact analytical solutions for the flow and heat transfer near the stagnation point on a stretching/shrinking sheet in a Jeffrey fluid. International Journal of Heat and Mass Transfer 57 (2013) 82-88.

[57] D. Pal and B. Talukdar, Buoyancy and chemical reaction effects on MHD mixed convection heat and mass transfer in a porous medium with thermal radiation and Ohmic heating. Commun. Nonlinear Sci. Numer. Simul. 15 (2010) 2878-2893.

[58] K. Muhammad, T. Hayat, A. Alsaedi and S. Asghar, Stagnation point flow of basefluid (gasoline oil), nanomaterial (CNTs) and hybrid nanomaterial (CNTs+CuO): A comparative study, Material Research Express 6 (2019) 105003.

[59] S. Sarkar and B. Sahoo, Analysis of oblique stagnation point flow over a rough surface, Journal of Mathematical Analysis and Applications 490 (2020) 1: 124208.

[60] A. U. Awan, S. Abid, N. Ullah and S. Nadeem, Magnetohydrodynamic oblique stagnation point flow of second grade fluid over an oscillatory stretching surface, Results in Physics 8 (2020) 103233.

[61] U. Farooq, Y. L. Zhao, T. Hayat and S. J. Liao, Application of the HAM-based mathematica package BVPh 2.0 on MHD Falkner-Skan flow of nanofluid. Computers & Fluids 111 (2015) 64-75.

[62] L. Zheng and X. Zhang, Modeling and Analysis of Modern Fluid Problems, A volume in Mathematics in Science and Engineering (2017) 115-178.

[63] S. J. Liao, Homotopy analysis method in non-linear differential equations, Springer and Higher Education Press, Heidelberg. (2012).

[64] L. Zheng and X. Zhang, Homotopy analytical method, Modeling and Analysis of Modern Fluid Problems (2017)115-178.

[65] T. Hayat, K. Muhammad, M. Farooq and A. Alsaedi, Squeezed flow subject to Cattaneo-Christov heat flux and rotating frame, Journal of Molecular Liquids 220 (2016) 216-222.

[66] T. Hayat, K. Muhammad, A. Alsaedi and M. Farooq, Features of Darcy-Forchheimer flow of carbon nanofluid in frame of chemical species with numerical significance, J. Cent. South Univ. (2019) 26: 1260-1270.

Turnitin Originality Report

Models for flows with melting heat and convection by Khursheed Muhammad . turnitin

From DRSM (DRSM L)

- Processed on 17-Aug-2021 11:24 PKT
- ID: 1632373680
- Word Count: 22767

Similarity Index
11%
Similarity by Source
Internet Sources:
3%
Publications:
9%
Student Papers:
2%

Focal Person (Turnitin)
Quaid-i-Azam University
Islamabad

sources:

1 < 1% match (student papers from 14-May-2018)
Submitted to Higher Education Commission Pakistan on 2018-05-14

2 < 1% match (student papers from 01-Mar-2018)
Submitted to Higher Education Commission Pakistan on 2018-03-01

3 < 1% match (student papers from 06-Jun-2018)
Submitted to Higher Education Commission Pakistan on 2018-06-06

4 < 1% match (student papers from 21-Dec-2013)
Submitted to Higher Education Commission Pakistan on 2013-12-21

5 < 1% match (student papers from 27-Mar-2014)
Submitted to Higher Education Commission Pakistan on 2014-03-27

6 < 1% match (student papers from 10-Jun-2013)
Submitted to Higher Education Commission Pakistan on 2013-06-10

7 < 1% match (student papers from 06-Jan-2011)
Submitted to Higher Education Commission Pakistan on 2011-01-06

8 < 1% match (student papers from 08-Sep-2010)
Submitted to Higher Education Commission Pakistan on 2010-09-08

9 < 1% match (student papers from 25-Mar-2021)
Submitted to Higher Education Commission Pakistan on 2021-03-25

10 < 1% match (student papers from 05-Jun-2014)
Submitted to Higher Education Commission Pakistan on 2014-06-05

11 < 1% match (Internet from 23-May-2020)
https://aip.scitation.org/doi/10.1063/1.4908602

12 < 1% match (Internet from 24-Mar-2020)
https://aip.scitation.org/doi/10.1063/1.4935571

13 < 1% match (Internet from 01-Jan-2020)
https://aip.scitation.org/doi/10.1063/1.4943398

14 < 1% match (Internet from 13-Dec-2019)
https://aip.scitation.org/doi/10.1063/1.5118929?af=R&feed=most-recent

15 < 1% match (publications)
Khursheed Muhammad, T. Hayat, A. Alsaedi, B. Ahmed. "A comparative study for convective flow of basefluid (gasoline oil), nanomaterial (SWCNTs) and hybrid nanomaterial (SWCNTs + MWCNTs)". Applied Nanoscience, 2020

16 < 1% match (publications)